A study of the dynamics of the Plasma Filled Rod Pinch

James Macdonald

Submitted in partial fulfilment of the requirements for the degree of Doctor of Philosophy of Imperial College London

Plasma Physics group

The Blackett Laboratory

Imperial College London

March 2020

Imperial College London

Declaration

I hereby certify that the material in this thesis, which I submit for the degree of Doctor of Philosophy, is entirely original unless otherwise cited or acknowledged in the text.

James Macdonald

March 2020

Abstract

The Plasma Filled Rod Pinch (PFRP) is a radiographic source used in high power flash x-ray machines. The purpose of this study is to provide detailed measurements of the plasma pre-fill required in the PFRP; then use these as a basis for 3D MHD simulations of the dynamics of the plasma in the PFRP.

Several interferometry systems were developed to analyse the density of the plasma pre-fill - a fibre optic based interferometer gave information at a single point over time and a CW laser-based system giving 12 temporally and spatially resolved interferograms. Thomson scattering and spectroscopic analysis were also undertaken, enabling estimates of the electron density of the plasma in the order of 10^{18} /cm^2 at the source with a divergence of 25 - 30°. The velocity of the plasma expansion was found to vary with the charging voltage for the system, with velocities of 8,500 – 14,500 m/s. The 12 frame interferometry system was then used to study the plasma from 6 guns placed around a central rod, a similar orientation to that used in PFRP experiments. The plasma guns were subsequently modelled as simple plasma sources, and the parameters of the plasma were set so that its behaviour matches the experimental data. The model has been used to simulate possible scenarios that could affect the performance of the PFRP.

This study has provided suggestions that the snowplough phase is very resilient to variations away from the standard configuration. Future work will hopefully include simulations featuring the Hall term.

Acknowledgements

Thanks are due to the many people who supported me during this study. Firstly, Dr. Simon Bland should receive a medal for his unending patience! His ingenuity and creativity saved many a day when things just didn't seem to want to work correctly. Prof. Jerry Chittenden was likewise patient with the many questions that arose during my attempts at running Gorgon and provided much needed advice at key junctures during the study.

I'd like to thank the many others at Imperial that helped me out, such as the MAGPIE team for all of their help in performing the spectroscopy and Thomson experiments, and the subsequent analysis, and the Gorgon team for their help in troubleshooting my simulations. Thanks are also due for the support, advice and assistance, provided by various people at AWE and NRL.

Finally, a huge thanks to my parents - two inspirational individuals that gave their all to provide their children with the best chances they could.

Contents

Index of figures

Chapter 1

Chapter 2

Chapter 3

Chapter 4

Chapter 5

Glossary of abbreviations, terms and symbols used

CW laser – a non-pulsed (continuous wave) laser light source
PFRP – Plasma Filled Rod Pinch, a type of flash x-ray source
eV – electron volt, a unit of energy, 1.602×10^{-19} Joules
refractive index – generally η, describes how the material affects the velocity of light travelling though it. η_e, η_0, and η_{tot} are used to denote the contributions to the refractive index from free electrons, neutrals, and the combined effect.
cyclotron frequency – also known as the Larmor frequency, the frequency of oscillation of a charged particle in a uniform field, given by $\omega_c = eB/m$. The Larmor radius is the radius of curvature associated with this oscillation, given by $r_L = v/\omega_c$.
c – the speed of light in a vacuum, approximately 3×10^{8} m/s
m_e – the mass of an electron, 0.91×10^{-30} kg
m_p – the mass of a proton, 1.67×10^{-27} kg
e – the charge of a single electron, 1.602×10^{-19} Coulombs, though q is often used in equations to cater for multiply ionised particles
r_e – the classical radius of the electron, $= e^2/4\pi\varepsilon_0 m_e c^2 \sim 2.82\times10^{-15}$ m
k_B – Boltzmann's constant, 1.38×10^{-23} J/°K
n_e,n_0,n_i – the densities of electrons, neutrals and ions, respectively.
λ_D – the Debye length, the distance over which charges are screened in a quasineutral plasma, given by $\lambda_D = \sqrt{\frac{\varepsilon_0 k_B T}{n_e e^2}}$
σ – plasma conductivity
μ_0 – permability of free space, $4\pi\times10^{-7}$ H/m
ε_0 – permittivity of free space, 8.854×10^{-12} F/m
T_e,T_i – electron and ion temperatures. Note: generally quoted in eV. (1eV = k_BT(=11600 °K))
v_e,v_i, - electron and ion velocities. Thermal velocities are given by $v_{th} = \sqrt{\frac{3k_B T_e}{m_e}}$
fringe constant - the change in density required to give rise to a complete fringe shift in interferometry, calculated using $\lambda n_c/\pi$, where n_c, the critical plasma density, is the density at which the beam cannot propagate through the plasma, given by $\varepsilon_0 m_e \omega^2/e^2$
plasma frequency, $\omega_p = \sqrt{\frac{n_e e^2}{\epsilon_0 m_e}}$,
V_A - Alfvén velocity, $v_A = B/(\mu_0 n_i m_i)^{1/2}$
magnetic field arising from current flowing in a wire, $B = \mu_0 I/2\pi r$

Many references exist for this information, F. Chen [G.1] is a good example.

Chapter 1: Introduction

This PhD study is focussed on gaining a better understanding of the operation of the Plasma Filled Rod Pinch (PFRP) flash x-ray source [1.1]. The PFRP offers a mm scale high brightness source for high power flash x-ray radiography. This study aims to build on existing works and leverage current simulation techniques to understand factors that may affect the performance of the source. Compared to other flash x-ray sources, the PFRP offers a relatively small source size coupled with a dose that is much higher than similarly sized sources, which together enable high resolution and contrast radiographic imaging.

1.1: Flash X-ray Radiography

Flash radiography is the practice of studying the properties of materials through variations in their density, such as the density change following a shock wave propagating through a sample, or how the wires in a wire array z-pinch ablate when the current flows. A short lived source (of x-rays, protons and others) is used to illuminate a sample. Different density regions will absorb or totally block differing amounts of radiation, allowing for the nature of the material to be discerned by variations of the signal captured by a detector, such as a sheet of x-ray film. A schematic of a typical x-ray radiography scheme is shown in figure 1.1.

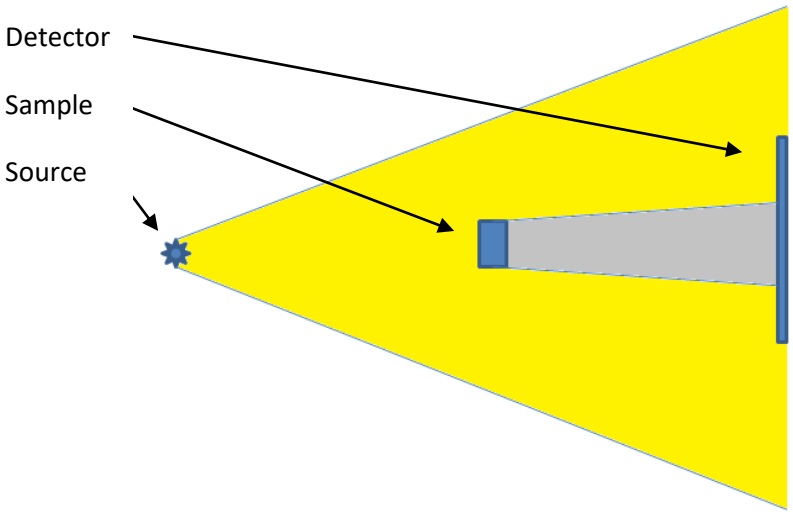

Figure 1.1: The basic configuration of a flash x-ray diagnostic. The yellow region represents x-rays emitted by the source, and the grey region is the "shadow" cast by the sample. Distances involved are largely set by the experiment, for example, if explosives are used the source and detector need to be at a safe distance.

In order to take an image of a fast-changing object that is suitable for qualitative analysis, the diagnostics must be well resolved in both space and time. If the object under study is travelling at velocity, v, in the duration of the x-ray burst, dt, the distance the object travels is vdt. If the total system magnification is M, the object will move Mvdt across the sensor. By decreasing the length of the x-ray burst, the amount the object's image moves across the sensor can be decreased, reducing the amount of motion blur recorded. To obtain the same exposure on the detector from a shorter pulse, it is necessary to increase the intensity of the burst accordingly.

Whilst other radiographic systems may use continuous sources and a time resolved detector, flash radiography systems tend to be able to generate very short bursts of more intense, harder (higher energy) x-rays and so have become the method of choice for many applications, particularly those examining high Z materials. Time resolved detectors also tend to have lower detection efficiencies than simple films so the latter are still regularly used in experiments [1.2].

The resolution of the diagnostic is governed by the size of the x-ray source as well as the resolution of the detector. A large source will lead to uncertainties in the path taken by the photon when it is captured by the detector, leading to lower resolution.

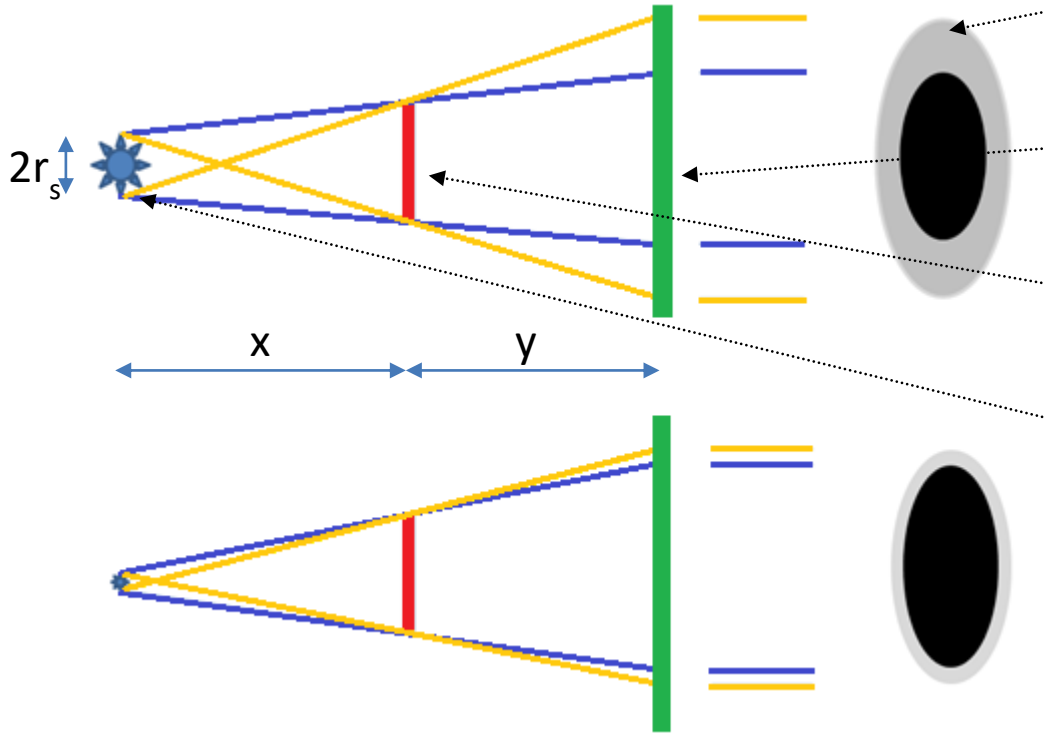

Figure 1.2: System resolution is affected by the source size. The grey region is the area where the recorded signal would be ambiguous, leading to decreased resolution. These sketches are not to any scale, ordinarily the distances separating the source, object and detector are much greater than shown.

A small source will decrease the uncertainties associated with the photon's path, and lead to higher resolution imaging. Figure 1.2 is a simple illustration of how the variation in the source size can impact the resolution of the final image. If the distance from the source to the sample is denoted as x, the distance from the sample to the detector is denoted as y, and the radius of the source is r_s, using small angle approximations, a simple estimate of the size of the ambiguous zone is given by $r_s y/x$. As the distance from the source and sample is generally governed by the experiment, improvements in resolution require decreases in source size. Detector blur, when the recorded signal leaks through to adjacent pixels (or grains in film), can further affect the achieved resolution.

1.2: Bremsstrahlung Radiation

Flash x-ray sources are usually created through the impact / interaction of a pulsed beam of electrons with a solid converter, which results in Bremsstrahlung radiation being emitted [1.3]. When an energetic electron, with velocity v_e, approaches a nucleus it can be deflected. A deflection can be considered as a lateral acceleration which results in radiation emission. As the nucleii are far

heavier than the electrons, they can be considered stationary. The power radiated by an accelerated charge is given by Larmor's formula:

$$P = \frac{q^2 a^2}{6\pi\varepsilon_0 c^3}$$ (Eq. 1.1)

where a, the acceleration, is given by $\frac{Ze^2}{4\pi\varepsilon_0 r^2}\frac{1}{m_e}$, *Z* is the charge state [1.4].

Assuming the electron is accelerated over a distance which is roughly 2*b,* where *b* is the deBroglie wavelength, λ=h/p, where h is Planck's constant, and p is the particle momentum [1.5]. This distance is chosen as it is the distance at which the particles must be considered to interact with other matter in a wave-like manner, in this case it is deflected, similar to diffraction.

The energy emitted in one collision is then given by the product of the power emitted, and the duration of the interaction, $2b/v_e$, v_e is the velocity of the electron:

$$\delta E \sim P\frac{2b}{v_e} \sim \frac{c^2}{6\pi\varepsilon_0 c^3}\frac{Z^2 e^4}{16\pi^2 {\varepsilon_0}^2 b^4 {m_e}^2}\frac{2b}{v_e}$$ (Eq. 1.2)

By integrating over a volume bounded by a cylinder of radius b, length $v_e dt$, filled with an ion density n_i we get the power from a single electron traversing the volume:

$$\frac{\Delta E_{tot}}{\Delta t} = \frac{Z^2 e^6 n_i}{24\pi^2 {\varepsilon_0}^3 c^3 {m_e}^2}\int_{b_{min}}^{b_{max}}\frac{db}{b^2}$$ (Eq. 1.3)

Multiplying Eq. 1.3 by n_e, and using $v_e = (k_b T_e/m_e)^{1/2}$, along with the identity:

$\int_{b_{min}}^{b_{max}}\frac{db}{b^2} = \frac{1}{b_{min}} - \frac{1}{b_{max}} \cong \frac{1}{b_{min}} = \frac{m_e v_e}{\hbar}$ (the reciprocal of the deBroglie wavelength), yields the total power:

$$P_{Brems} = \frac{Z^2 e^6 n_i n_e}{24\pi^2 {\varepsilon_0}^3 c^3 {m_e}^{3/2}\hbar}(k_B T_e)^{1/2}$$ (Eq. 1.4)

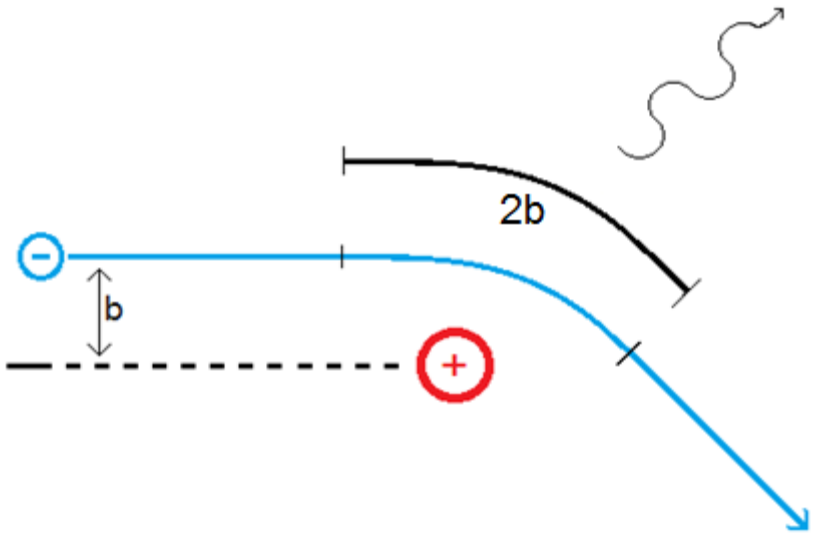

Figure 1.3: The Bremsstrahlung process

This is the classically derived version of the radiated power equation and is very similar to the quantum mechanically derived version, which features an extra term called the Gaunt factor [1.6], an approximation used to correct for quantum effects important to emission, absorption and opacity. In cases where these are not relevant, it is generally approximated to 1.

The energy, or hardness, of the emitted x-ray varies as a result of how closely the electron approaches the nucleus. A glancing incidence would result in a slight deflection of the electron's trajectory, leading to a low energy, or soft, x-ray. A major deflection will give rise to a higher energy x-ray. The highest energies will occur when the electron is almost completely stopped. Bremsstrahlung radiation is produced with a range of energies. Low energy sources produce spectra with distinctive peaks that correspond to electronic transitions. However higher energy sources do not exhibit specific lines in their emission, as the range of allowable transitions leads to a continuous spectrum. The highest energies will be governed by the acceleration voltage, but the peak is generally between 1/4 and 1/3 of the maximum [1.7].

The energy and intensity of an x-ray source is governed by many factors, including the density of the target and electron beam density. Electron density is governed by the electrical power driving the

source. In order to attain sufficient numbers of electrons in the desired timeframe, the source current needs to be high.

Flash x-ray sources tend to use electron beams accelerated across a gap from the cathode to the anode. A high accelerating voltage easily (keV to many MeV range) overcomes the work function (the energy required to liberate an electron from the surface of a material, generally in the single eV range) of the electrons on the surface of the cathode and they are drawn out to create a beam of electrons that are subsequently drawn towards the anode, the positive electrode, figure 1.4. Ions are also subjected to similar forces but are not generally drawn out of the anode surface. Some current may arise resulting from ions being liberated from the anode by the electron current heating it. Ions do not contribute to the generation of x-rays, although sometimes the ion current can aid focussing of the electron beam. The configuration shown in figure 1.4 is one of the simpler source designs, and shows the basic features common to most flash x-ray sources, though it tends to have a relatively large source size (roughly 50 to 200 mm).

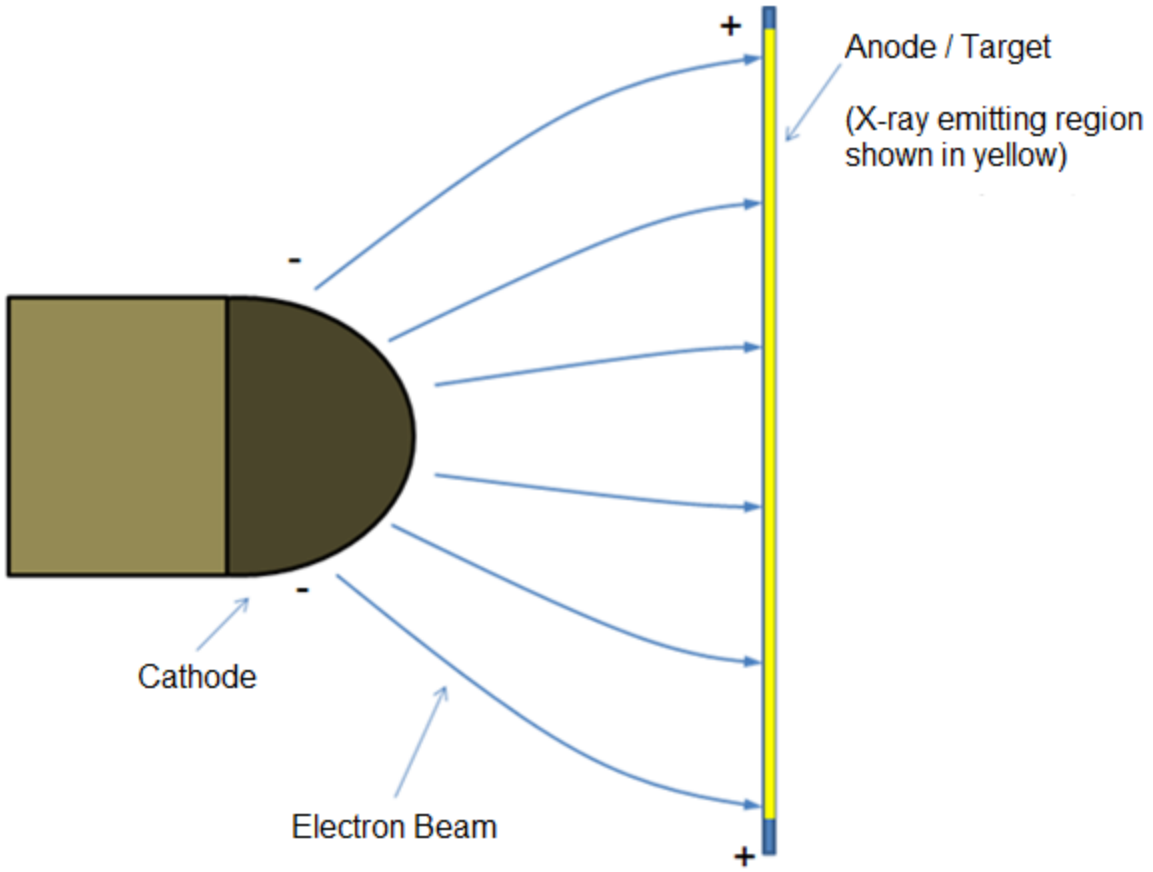

Figure 1.4: The basic configuration of a large area radiographic source. The large electric field between the anode and cathode draws electrons off the cathode surface and into the gap, where they undergo acceleration before impacting the anode target. The yellow region shown here illustrates the source size.

The anode features a converter, a target made of a dense, high atomic material, such as tungsten, that provides a large number of opportunities for the incoming, highly energetic electrons to interact with nuclei. The target must be radiographically thin so that any x-rays that are created are able to penetrate it, rather than being re-absorbed. Such arrangements of cathodes and targets are often referred to as x-ray "diodes", as the current will preferentially flow in a certain direction between a pair of electrodes, just like the semiconductor components of the same name. The oblique target configurations used in devices such as dental x-rays are not easily accommodated in these diodes due to the high field stresses present. Dental systems are optimised for longevity and lower energy x-rays, flash x-ray sources are optimised for high fluxes of higher energy x-rays, where single-shot lifetimes are acceptable. Considering this, oblique targets can be much thicker which enables long lifetimes.

X-ray diodes come in many different configurations, from desktop x-pinch devices which produce ~10 mJ yields of a few keV radiation from a sub-ns <50 µm sized source [1.8] to large area diodes connected to building sized pulsed power driver that produce many 10s of J of radiation at energies ranging 1 to beyond 20 MeV in roughly 20 to 100 ns [1.9]. The intensity in these larger sources is often expressed as "Dose rate" and is generally measured in Rads, indicating how much dose would be absorbed in a given time, for a given material (eg. Air, Si) [1.10]. 1 Rad is 0.01 Gy, or 0.01 J/kg of absorbed x-ray dose. In commercial systems, the dose measurement is generally quoted at 1 metre from the source. The relationship between accelerating voltage, V, the current, I, and dose rate is often stated in a "radiographer's equation" [1.11]:

Dose rate (Rads/sec) = $1.7 \times 10^{6}.I.V^{2.65}$, for Z=73 (Tantalum target) in the direct-ahead direction, at 1 m.

This phenomenological equation depends on the type of x-ray source as higher voltages skew the emission of the x-rays (lower voltage sources tend to emit isotropically, higher voltage sources lead to more emission in the forward direction [1.12]), the above equation assumes paraxial electrons, that is, electrons travelling in the forward direction. The dose varies with current for the simple reason that there are more electrons in the beam to interact with the target.

In the target region there is a trade-off at play between the amount of energy deposited into the small volume and the time of the deposition. Greater energies lead to more rapid expansion of the source volume, due to heating effects. The heating of the converter can vaporise it and give rise to plasma formation. If the plasma remains sufficiently dense, there will still be a large Bremsstrahlung component, just from a larger, less dense source than when it was solid, leading to a less well-defined spot. If the energy can be deposited quickly enough though, the converter doesn't have any time to grow appreciably, and so, the spot remains small. If lower energy levels are used, there's less expansion, due to reduced heating effects, or shorter time.

The impedance of the x-ray source is what relates its geometry and dynamics to the generator applying the voltage and supplying the current. The impedance of a system can be broken down into three parts, a real part which is the resistance, and two imaginary parts which are the capacitance and the inductance of the system, and is given by $Z= [R^2 + (\omega L -1/\omega C)^2]^{½}$, where Z is the impedance, R is the resistance, L is the inductance and C is the capacitance [1.5]. L and C can be estimated in design software or measured. Impedance is used, rather than purely resistance, because of the transient nature of the applied power. X-ray source impedances can range from 10s of Ohms, to near-shorts, below 3 Ohms, and may also vary during the current pulse. For the same stored energy, lower impedance diodes lead to high currents. Some sources rely on high currents to give rise to a pinching of the beam, which increases the energy density of the beam by restricting its size.

1.3: Pulsed Power

The very brief high voltage pulses required for flash radiography are created using pulsed power systems. Here electrical energy at low power is stored over several seconds / minutes, then released as a high-power pulse a few tens of ns in duration. Such compression is achieved in one or more stages. The most often used system is based around a Marx bank [1.13]. These use an array of capacitors and fast high voltage switches. The capacitors are charged in parallel, to 50-100 kV each, typically, for flash x-ray machines. Once charged, the switches are triggered, and this causes a re-configuration of the capacitor circuit into series, stacking the charged capacitors. For example, charging 50 capacitors in parallel to 50 kV and then switching them to discharge in series would yield an output voltage of 2.5 MV. The output of a Marx bank, however, is generally too slow for flash radiography, with the output current pulse generally being in the µs range due to the self-inductance of the capacitors and switches. To further shorten the pulse, a "pulse forming line" (PFL) is employed, which is generally a co-axial arrangement filled with oil or water for MV-scale machines, which acts as a very low inductance capacitor. The PFL is charged from the Marx bank in µs (Water has a high dielectric strength for very short timescales, so a water-filled PFL can be charged for up to

a few µs, where an oil-filled PFL can be charged for longer), then a switch at the end of the line is activated, and the line discharges into the load in a few tens of ns. As it has been in development for over 50 years, the Marx-PFL-based approach has worked well for many years but tends to be very large and can be prone to single point failure as the entire voltage pulse is affected if the rapid reconfiguration phase fails for some reason. If a component breaks down, the entire pulse energy can be dumped into the damaged component. For further reading, [1.14] and [1.15] provide good introductions to pulsed power.

Recent developments have led to alternatives to Marx-PFL configurations - Inductive Voltage Adders (IVAs) [1.16], Linear Induction Accelerators (LIAs) [also 1.16] and Linear Transformer Drivers (LTDs) [1.17]. In all of these cases, fast voltage pulses are added together over a series of smaller acceleration gaps applied in regions known as cavities, with no single region experiencing the full voltage, except the output region. For IVAs and LIAs, the power for each cavity comes from a separate PFL which is fed from a shared Marx bank or other storage device. LTD cavities contain their own separate power storage stages. The multiple cavities are required as a single gap would not be able to support the full accelerating voltage.

In IVAs a separate Marx bank energises a number of PFLs that in turn feed a series of induction cavities. In LTDs the Marx and PFLs are replaced with many low inductance capacitors and switches connected directly around the cavity. The cost of IVAs and LTDs can be higher than traditional systems, but they enable higher output voltages, pulse-shaping and their modularity reduces the effects of a single point failure.

The basic operations of the large pulsed power machines, and the components that go into them are essentially the same as their lower power electronics counterparts, such as capacitors, resistors, transmission lines and so on. Unlike “standard” electronics, however, many of these components require the interactions of mechanical engineers, electronics engineer and physicists to construct.

1.4: X-ray diodes

The simplest type of source is the large area diode, as shown in figure 1.4. A high potential, in the megavolt range, is applied across the anode-cathode gap (a-k gap), and electrons are drawn from the surface of the cathode, as the applied voltage far exceeds their work function. The cathode is generally made of high-density carbon as it provides an even emission surface. The radiographic spot size for such a source is generally in the cm range, these are used for their very high doses of hundreds of Rads and beyond. The current is generally in the tens to hundreds of kiloamps range, depending on the application. To reduce the size of the source and improve the resolution several modifications to the design of the diode are commonly used.

Self-Magnetic Pinch

The Self-Magnetic Pinch (SMP) diode [1.18] is a narrow cylindrical cathode tip, as opposed to the much larger hemispherical cathode used in the large area diode, a small distance from an anode plate, see figure 1.5. The anode plate is often behind a thin metallic foil, not shown in figure 1.5 to aid clarity.

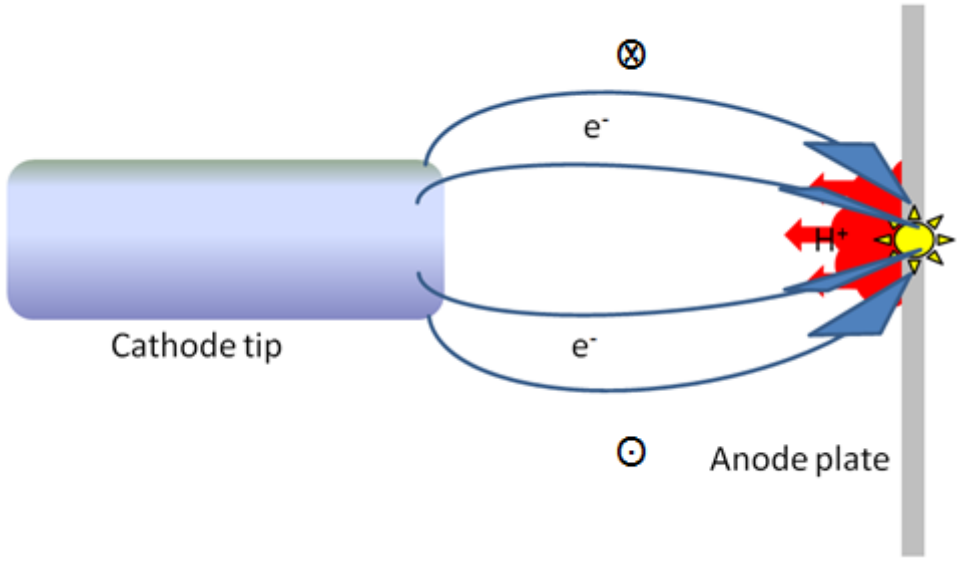

Figure 1.5: Sketch showing the operation of the self magnetic pinch diode. The cathode tip is generally cm scale, as is the cathode-anode gap.

Electrons are drawn off the cathode to form a beam of electrons. The electron beam heats the anode plate, giving rise to a surface plasma. Ions are drawn out of the plasma, and stream back to the cathode. The ions cancel out part of the space charge of the electrons and also add to the current flowing in the region, causing the electron beam to decrease radius, hence the "pinch" part of the name. This behaviour gives rise to a tightly confined electron beam on the anode/converter, producing a radiographic spot of < 4 mm, whilst maintaining a dose range of 1-100s R. [1.18] points out that the impedance varies during the pulse, starting high as the diode begins to conduct, settling around 35 Ohms for the main part of the pulse, and then dropping as the anode plasma reaches the cathode, causing the impedance to collapse. The role of the foil is also discussed, as a momentary impediment to the expansion of the anode plasma, delaying the impedance collapse.

Vacuum Rod Pinch

The SMP offers a bright source with a smaller source size than the LAD, and operates over a wide range of voltages, but better resolution is offered by other sources such as the vacuum rod pinch. The vacuum rod pinch consists of a thin rod protruding through a ring [1.19], sketched in figure 1.6.

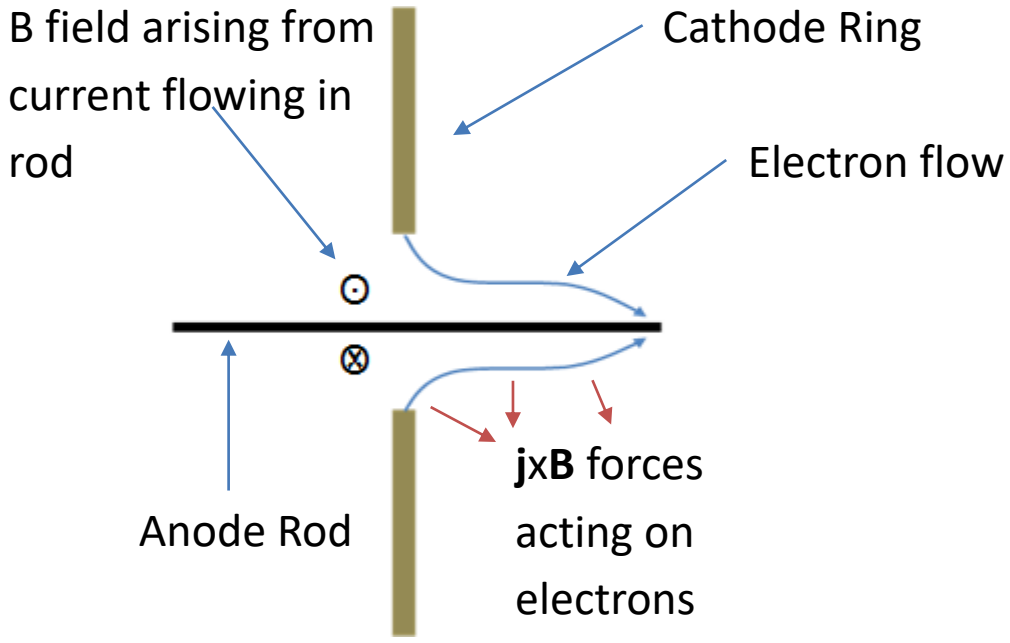

Figure 1.6: Basic design of the vacuum rod pinch diode. The rod is generally ~1 mm in diameter, and protrudes through the hole by a few tens of mm.

When the voltage pulse is applied, electrons are drawn from the cathode ring, and are accelerated toward the rod. As the current flows, the **jxB** forces arising from the magnetic field due to the current in the rod direct the electron flow to the tip of the rod. The rod pinch provides a small spot (~1 mm), but with low dose (a few R), as the impedance is in the tens of Ohms, due to space-charge limited and magnetically-limited current flow [1.20], where the current that can flow is restricted by the ability of the cathode to emit electrons due to those already emitted screening the electric field, and where the electrons flow in a sheath along a surface due to the magnetic fields, as shown in figure 1.6. As the diode is generally operated at ~2 MV voltages, the dose rate is limited by the emission being almost isotropic, rather than more forward directed as occurs with higher voltage sources.

1.5: The Plasma Filled Rod Pinch

To reduce the impedance of the vacuum rod pinch in order to increase the dose, the plasma filled rod pinch (PFRP) was developed [1.1]. Like the vacuum rod pinch, the PFRP consists of an anode rod protruding through a cathode ring. However, the PFRP has an additional plasma pre-fill from plasma guns that surround the rod, see figure 1.7. This pre-fill lowers the impedance of the source considerably to a few Ohms, which leads to a higher current, in the region of 500 kA, and ultimately, a much higher dose than the vacuum rod pinch, of 15 R upwards, whilst retaining the small source size.

During operation, as the main current pulse flows, the plasma is swept along the rod in a "snowplough". This occurs in response to magnetic forces acting on the components of the plasma. The plasma continues to travel off the end of the rod, and this is when an accelerating gap opens up between the anode rod and the surface of the plasma. Electrons are drawn from the plasma and accelerated across the gap to the tip of the anode rod, where they interact with the rod material through Bremsstrahlung, as illustrated in figure 1.8. As the electrons are highly energetic, and the rod is thin, they may pass through a number of times, generating x-rays on each pass.

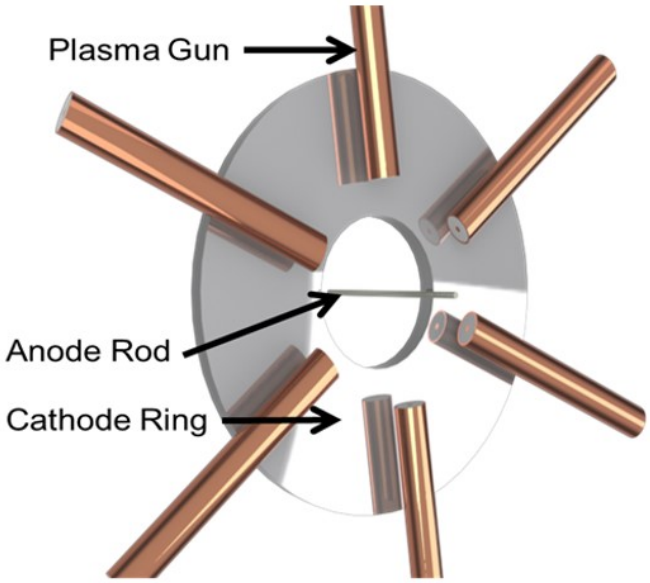

Figure 1.7: The construction of the plasma filled rod pinch diode. The rod protrudes through the hole by approximately 25 mm, and the plasma gun nozzles are approximately 25 mm from the rod.

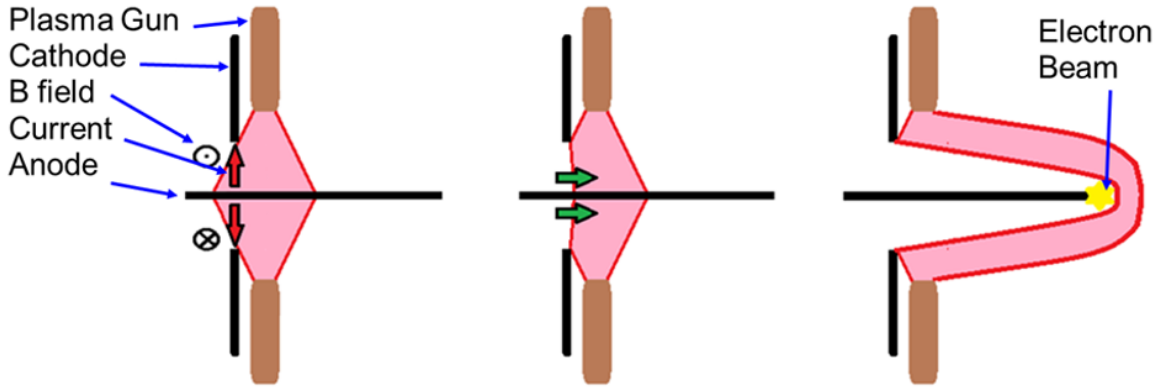

Figure 1.8: Operation of the Plasma Filled Rod Pinch

This can also happen in the vacuum rod pinch. The electrons are concentrated on the very tip of the rod but may impact it up to a few mm further down. This means that on axis, the spot is well defined, and round, but from the side, however, the spot is elongated, which means the radiographic resolution of the PFRP is dependent upon alignment. Initial experiments on Gamble at NRL [1.1] saw the low impedance phase of operation that marks the snowplough last for 50 ns, at which point the voltage rises to 1 MV, with the current peaking at 500 kA. The x-ray pulse lasted for 60 ns with a recorded dose of 20 Rads, roughly $3x10^8$ Rads/s.

Increasing the plasma pre-fill density enabled control over the x-ray pulse width which was minimised to 8 ns and an increased dose rate, 10^9 Rads/s, though a lower total dose due to the shorter x-ray burst. The denser pre-fill leads to a longer low-impedance phase.

1.6: Plasma opening switch operating regimes

The operation of the PFRP is very similar in many ways to that of another high-power device known as a Plasma Opening Switch, or POS. POSes are used to interrupt large current flows, allowing high voltage pulses to be generated into the load. Conventional switches cannot open high currents, as arcs form between the electrodes. The physics underlying POS operation has been explored in a number of publications and is often used as a basis for understanding PFRP dynamics. Published literature states that there are several processes that can lead to a POS opening. Grua, Cassany [1.21] and Weber [1.22] in particular cover the different opening modes, the dominant process being governed by factors such as plasma density, current evolution and the geometry of opening switch. The modes of interest here are the "Hall regime" and the "snowplough".

In the Hall regime, often referred to as the Extended MHD, or eMHD, regime, the magnetic field is able to penetrate and magnetise the plasma and causes the electrons to aggregate into conduction channels, as shown in figure 1.10 but the ions are immobile (or can at least be considered such as they cannot respond to the magnetic pulse as quickly as the electrons can due to their higher mass) and remain stationary during the pulse as the ion plasma frequency, ω_{pi}, is lower than the characteristic timescale of the pulse.

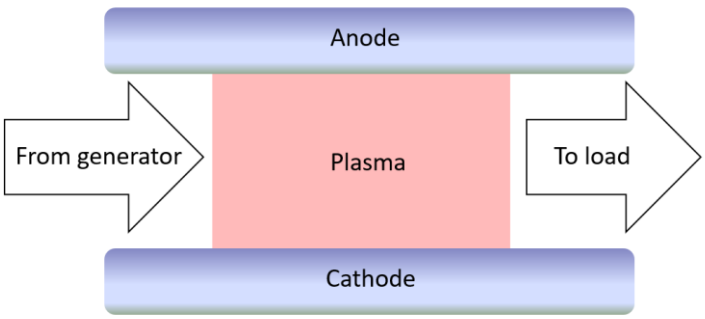

Figure 1.9: A basic plasma opening switch configuration

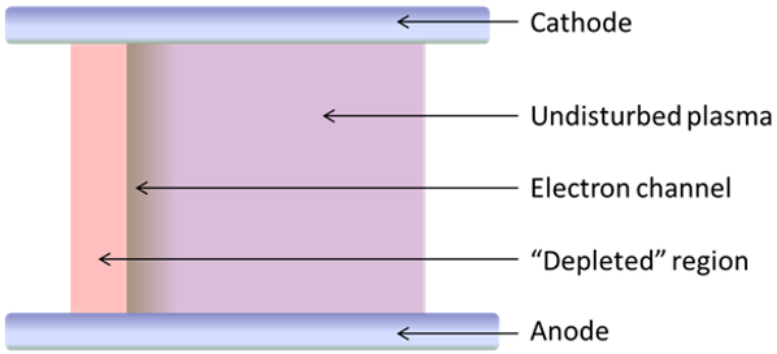

Figure 1.10: Hall regime operation can lead to an electron channel arising as the electrons are swept by the magnetic field whilst the ions remain immobile.

The snowplough regime is different in that the ions are also swept by the magnetic field, clearing the volume behind the shocked-up plasma, figure 1.11. The plasma is separated from the vacuum by a non-neutral sheath, that is c/ω_{pi} wide, as the electrons are able to respond to the magnetic field but the ions are not. [1.23] states that the time electrons or ions spend in the sheath sees them acquire a perpendicular displacement equal to c/ω_{pi}. This sets the requirement for the snowplough mode to dominate that the characteristic width of the sheath is larger than c/ω_{pi}.

For the Hall regime to dominate, the timescales involved need to be less than the ion cyclotron period. For carbon atoms, the ion cyclotron period can be estimated to be a few tens of nanoseconds at the high currents present in the main pulse. When the current is low, it is feasible that the Hall regime will dominate until the current has ramped up sufficiently for the snowplough to take over, due to the lower B fields present.

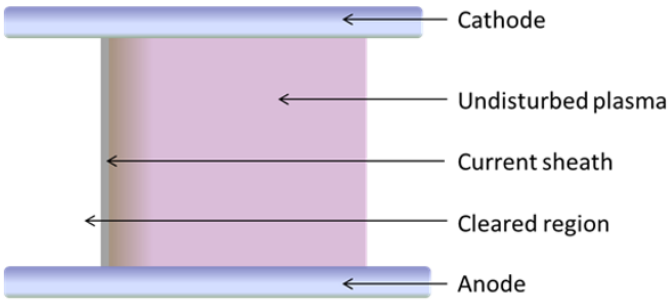

Figure 1.11: In the snowplough regime, ions, as well as electrons, are cleared from behind the current sheath, leaving a cleared region.

If the period of the ion gyrofrequency is shorter than the timescales of the current pulse, they will be able to respond to the pulse's magnetic field, and the field will permeate the plasma more readily, rather than acting as a piston pushing the plasma in a snowplough. If the current pulse rises too slowly, the plasma will be able to respond to the field. A typical rise profile for the pulse is 0-500 kA in 50 ns, with the magnetic field at the tip of the rod estimated to be 400 T in [1.1]. The snowplough propagates at up to the Alfvén velocity [1.24], whereas the field penetration travels through the plasma faster for the Hall regime. The speed limit applies for the snowplough as it requires the ions move as well as the electrons, and they take longer to move than the electrons do because of their greater mass. Estimates of the Alfvén velocity, 6×10^5 m/s (1 mm from the centre of the rod with 500 kA flowing in the rod gives a magnetic field of 100 T, n_i = 1018, T_i = 1 eV) are of a similar magnitude to the snowplough propagation speed estimates gained from [1.1], in the order of 5×10^5 m/s, which supports the notion that the PFRP operates under the snowplough regime. The main method of estimating the velocity of the snowplough propagation is to measure the time of the low impedance phase of the operation. Once the plasma travels past the rod's tip, the impedance of the system increases dramatically. The paper on magnetic field penetration into plasmas [1.23], provides a precise criterion for the transition from snowplough to field penetration. The factor R is used as a guide to the expected behaviour of the magnetic field interacting with the plasma:

$$R \equiv 2\frac{v_{sp}}{v_c} \qquad \text{(Eq. 1.5)}$$

v_{sp} and v_c are the snowplough and convective skin shock velocities respectively.

Eq. 1.5 shows that the dominant effect is governed by the variation of density length scale. If R>>1, the snowplough mode dominates, if R<<1, the Hall mode does. If the density varies on a scale less than the ion skin depth, the Hall effect is dominant. Fruchtman continues to analyse the division of energy flow, and concludes that, in the snowplough mode, the energy flux is equipartitioned between the magnetic field energy and plasma energy. The energy that goes into the plasma is divided between kinetic energy and heating. In the Hall mode, the ions do not gain significant energy, but one quarter of the energy goes into heating the plasma. The gradient in the flux of electron thermal energy drives an increase in the electron thermal energy until it equals the magnetic field energy.

In a different paper, [1.25] discusses how the polarity of the current pulse can affect the penetration of the field into the plasma. Assuming the plasma is quasi-steady-state, the electron trajectories must flow with the lines of current flow. If the density is uniform, and electrons move from small to large radius, the field must grow also. If the electrons flow from large radius to smaller, the magnetic field penetration decreases. However, in the case of non-uniform plasmas. field penetration can occur in a positive polarity.

1.7: Aim of the study

As highlighted in the previous section, there are many factors that could affect the behaviour of the PFRP, in part the behaviour of the plasma pre-fill and its subsequent dynamics. How resilient is it? Is there any scope to optimise it? A detailed study of the operation of the source using 3D MHD simulations didn't exist. The overarching aim of this thesis was to develop the capability to model this device in 3D.

To accomplish this, required detailed diagnostics on the behaviour of the plasma in a PFRP. This can be achieved by first studying the plasma from a single plasma gun; then the exploration of operation of multiple guns firing together, observing the effects of interactions between the plasma plumes projected from the guns and a rod inserted at the centre.

Measurements of plasma density, position and velocity from a single plasma gun were then used as the basis for calculations and subsequently validated against measurements with multiple guns. Using the 3D MHD simulation code Gorgon [1.26, 1.27], the effects of variations in the timing and rise time of the main current pulse, plasma pre-fill density, and pre-fill asymmetries were explored, providing simulations that can subsequently be used as a basis for experiments on a large pulsed power facility. Once the computer model was developed, it was used to investigate the nature of the plasma behaviour, such as the shape of the snowplough, the thickness of the current sheath and the distribution of the magnetic fields.

1.8: Structure of thesis

This thesis consists of six chapters, this introduction chapter being the first. This chapter aims to give the reader a good background to the focus of this study, and why it is required.

The rest of this thesis is structured as follows:

Chapter 2 outlines the diagnostics and techniques used in investigating the plasma guns that are used as the source for the plasma pre-fill.

Chapter 3 presents the results of these experiments, first outlining measurements from a single gun, before examining the interaction between plasmas from multiple guns in a configuration used in PFRPs. The effects of misalignment and guns misfiring is also examined.

Chapter 4 introduces the simulation techniques used to model the PFRP, in particular outlining how the 3D MHD code Gorgon was employed.

Chapter 5 presents the results of the simulation work.

The final chapter summarises the results and gives ideas for future avenues of research.

Chapter 2: Experimental set up & diagnostics

The primary goal of this study was to obtain a more detailed understanding of the operation of the PFRP. The plasma pre-fill that bridges the gap between the anode and cathode is key to the performance of the PFRP, ultimately determining the formation of the electron beam between the plasma and the rod (including when it forms, the amount of current flowing through the beam and the dynamics of the plasma close to the rod).

The pre-fill plasma is created by firing six plasma guns made from co-axial cable with copper inner and outer conductors, and a solid PTFE insulation layer in between (they are also known as cable guns due to their construction). The plasma is generated when a voltage pulse, provided by a high voltage pulse generator, is applied to the cable, and flashover on the surface of the insulating layer occurs at the unconnected end, which has a nozzle cut into the end face. As the current flows through the flashover region, the insulator is ablated and subsequently ionised, giving rise to a plasma. The **j**x**B** forces from the current, and the density gradient of the plasma drive the plasma outwards, away from the nozzle. They are generally used in a vacuum of 10^{-4} mbar. Six guns are used in order to obtain a reasonably uniform plasma fill and provide a level of redundancy.

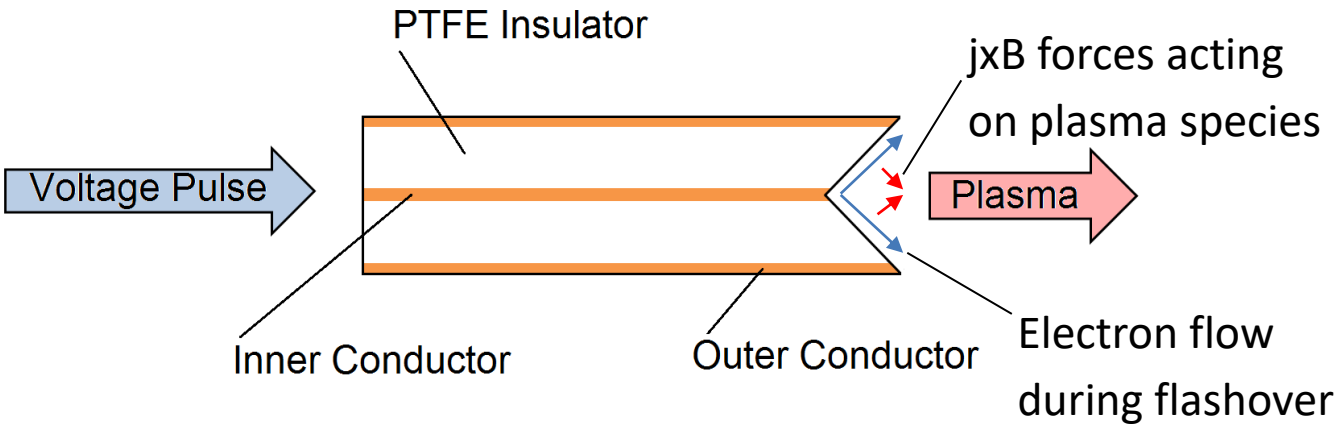

Figure 2.1: Basic construction of plasma gun [2.1]

Studies were carried out, [2.2], looking at different constructions for the plasma gun and differences in the behaviour of different designs were observed, such as plasma propagation velocity and density changes when altering the materials used in the plasma guns. For example, when the central conductor was modified to tungsten rather than copper, the electron density dropped slightly from 4.5 to 4.0 $x10^{20}$ m^{-2}, and the velocity increased from $23x10^3$ to $30x10^3$ m/s. They also investigated the effects of the angle the face is cut at, noting a similar divergence angle, but density dropped to a third and the velocity increased to $44x10^3$ m/s, when the gun face was machined flat.

Although these variations could prove interesting, it was decided to focus solely on the "standard" design, a copper outer and inner conductor, and Teflon insulator, sold as RG-401 [2.3] with a 60° cone machined into it as described in [2.1]. It is this version that is used in the PFRP on Gamble II at NRL [2.4].

This PhD study explored key parameters of the plasma, including the density (both electron and neutral densities), the temperature, and the ion species present in the plasma. Interferometry was used to explore densities whilst spectroscopy was used to understand the components of the plasma, and Thomson scattering was utilised to provide information on its temperature.

Initially, the plasma from a gun was studied then experiments with multiple guns were performed, as the PFRP is usually configured with six guns.

Previous studies, for example [2.5,2.6,2.1] the plasma density from a plasma gun was understood to be in the region of 10^{15} - 10^{18} /cm^3, temperatures in the range of 1-10 eV, with velocities of the front of the plasma in the region of 10x10^3 m/s. This provided the information to guide the design of the diagnostics.

2.1: Experiment setup: Characterisation of plasma from a single plasma gun

In order to replicate the operating conditions for the plasma guns in the PFRP, a vacuum chamber was used that featured viewing ports of opposing sides. This configuration allowed for a line of sight passing through the chamber, side-on to the plasma gun nozzle, to facilitate interferometry, as well as an end-on view using a turning mirror. A turbo-molecular pump backed by a roughing pump was used to evacuate the chamber. The set-up is shown in figure 2.2.

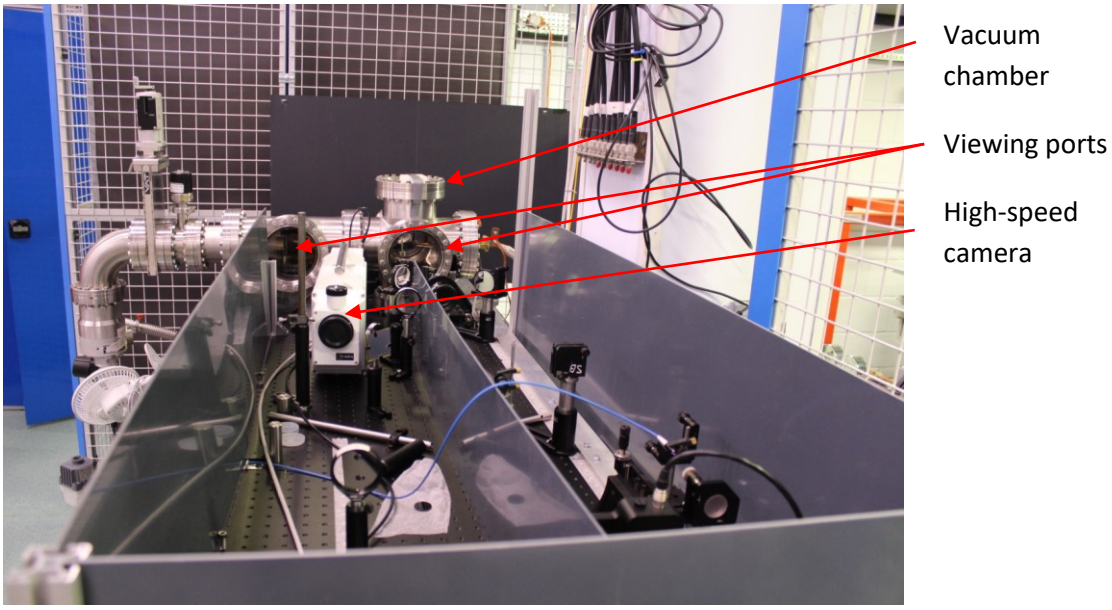

Figure 2.2: The initial vacuum chamber in situ in the lab. The two viewing ports can be seen, with the one on the right matched by another on the other side of the chamber, not visible. The optical apparatus in the foreground is the initial version of the interferometer

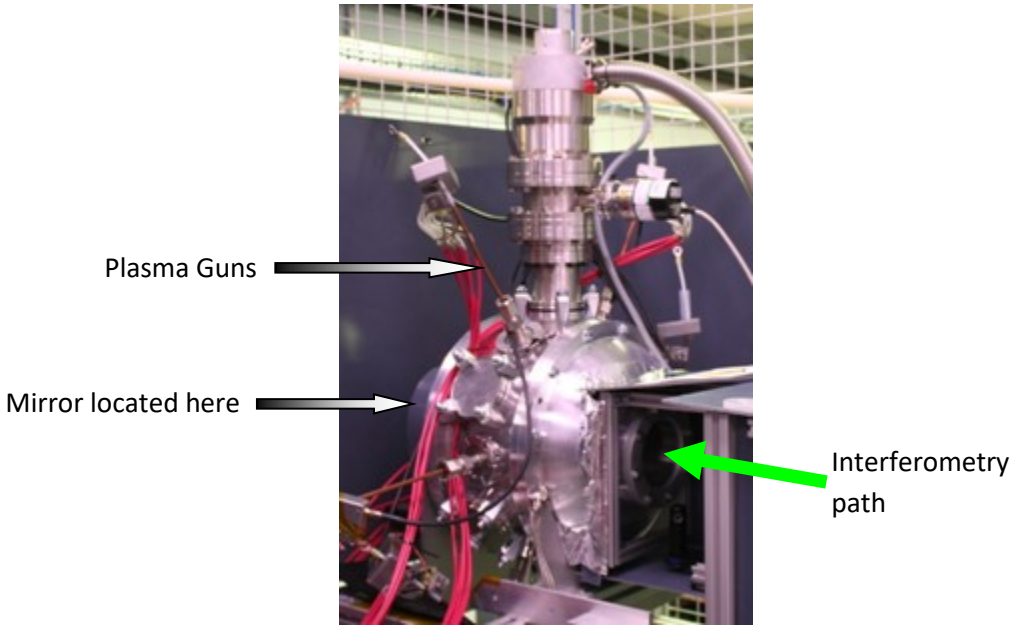

Figure 2.3: The six-gun chamber in position, small panel in laser enclosure removed to show diagnostics port location.

The chamber was mounted on a small optical table, which sat on a specially-built frame made from heavy duty extruded aluminium struts, with vibration absorbing rubber between the table and the floor. In order to keep vibrations to a minimum, the roughing pump was placed on the floor, and connected to the exhaust of the turbo pump by a long flexible bellows-type pipe.

To study the convergence of multiple guns, a second chamber was constructed that could accommodate six guns. This chamber supports axial views, aligned to the axis of the rod in the PFRP, side on to the converging regions of plasma from the guns, see figure 2.3

Timing of the various systems was achieved through the use of a Quantum Composers 9528 trigger generator. This provided 8 individually adjustable outputs to trigger different subsystems, such as the high-speed camera, the oscilloscopes, and the trigger unit for the plasma gun driver. The outputs can be set to any voltage up to 45 V and can be made to be directly compatible with most systems.

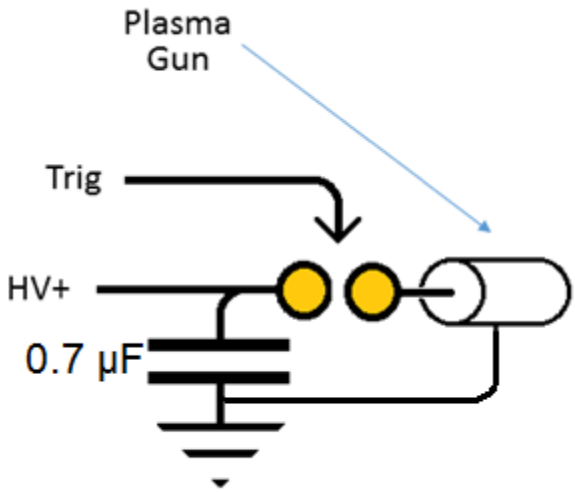

Figure 2.4: A basic schematic of the IC pulser.

Initially, a small pulser was used to power a single plasma gun. This pulser was built at Imperial College, based on the discharge of a single 0.7 µF capacitor charged to ~ 25 kV and it was able to provide currents of ~3 kA to the plasma gun, which although much less than the ~25 kA usually used in PFRP systems, enabled the diagnostics to be timed and optimised. A simplified schematic is shown in figure 2.4.

As the experiment progressed, two more powerful pulsers were employed, each being capable of driving up to three plasma guns at ~25 kA each. This type of pulser, termed a "doghouse" was on loan from the Naval Research Labs in Washington, DC. Each doghouse, see figure 2.5, contains three 0.7 µF capacitors and a sealed spark gap switch. One electrode on each capacitor is connected to one side of the switch, the other side of the switch is connected to ground. The other electrode on each capacitor is connected to the central conductor of the plasma gun but is also grounded through an inductor. During operation, the capacitor is charged to a high positive voltage (in the 20-25 kV range). When the switch is triggered, the electrode of the capacitor is instantly connected to ground. As the other electrode (and the inner conductor of the plasma gun) is grounded only through an inductor, the voltage momentarily reverses which causes the open end of the plasma gun to flash over as the only fast route to discharge.

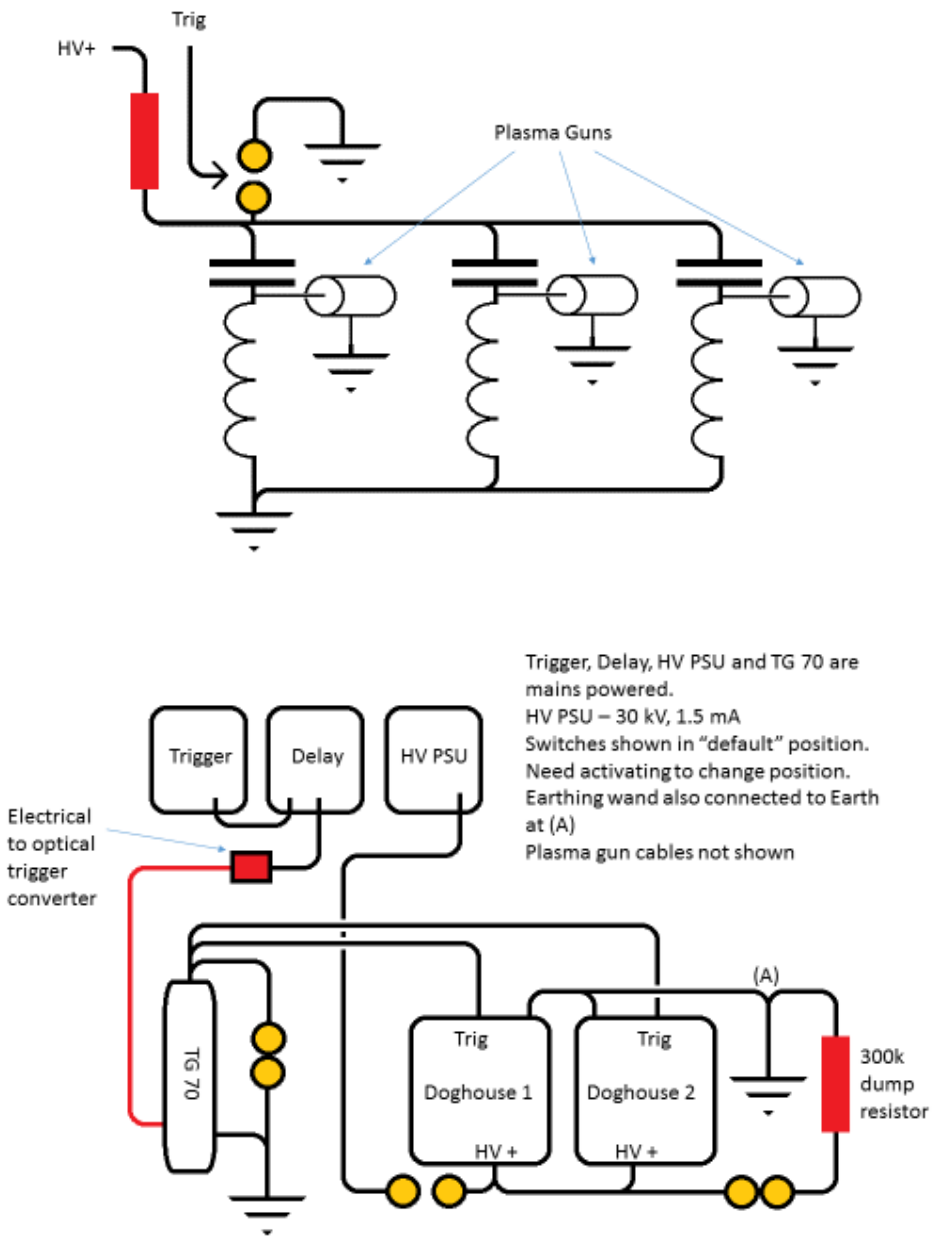

Figure 2.5: Top: Basic circuit diagram of the central pulser unit (doghouse) Bottom: Schematic showing how the pulser units integrate into the larger system

Introduced in [2.6], the design provides a low inductance, and has the added benefit that the whole of the run of cables feeding the plasma guns remains at ground potential except for when the pulse is applied, reducing the electrical stresses on the cable, and lowering electrical hazards. The system was triggered by either a Maxwell TG-70 trigger generator [2.7] or a Thyratron [2.8]. At one point, the TG-70 failed following a shot, and so triggering duties were taken over by a Thyratron system,

built at Imperial College. This consisted of a thermionic valve, that can rapidly switch high voltages into the trigger cable of the doghouses. Both of these systems provided a very fast rising edge (ns) up to voltages over 30 kV.

The charging and dumping system was made using pneumatically operated switches, set so that the system fails safe in the event of loss of pressure. These connect a high power 300 kΩ dump resistor to the guns, rather than just using a "hard" dump system. The reason for this choice was that the plasma guns fire when a voltage builds up across the grounded inductor. If a hard dump was used, the voltage would spike in a similar timescale to when the switch fires. By dumping through a resistor, dI/dt is minimised, and the voltage that builds up on the inductor is limited, preventing the plasma guns from firing.

2.2: Diagnostics

2.2.1: Current measurement

Rogowski coils were used to monitor the current flowing to the guns, both as a fiducial, and also as a diagnostic in itself. They are robust and easily made. They consist of a length of wire that has the return path twisted back around it, rather than the end of the wire simply closing the loop. This length is then placed around the cable under study. When a time-varying current is passed through the enclosed wire, the magnetic flux passing through the coil changes, setting up a voltage in the coil through induction.

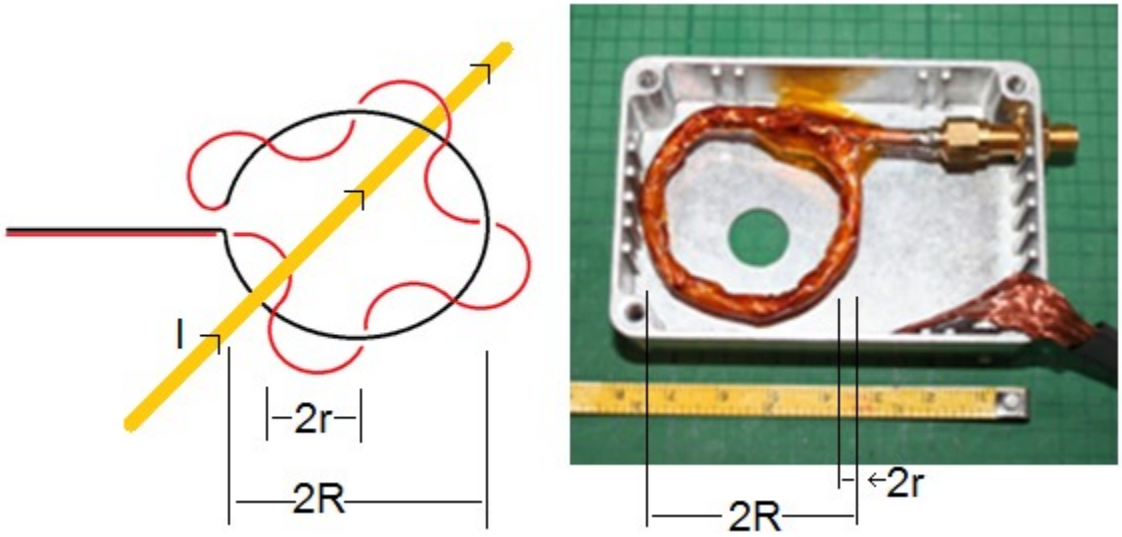

Figure 2.6: Left: Sketch showing the basic structure of a Rogowski coil, the current-carrying wire goes through the centre of the probe. Right: Photograph showing the construction of one of the coils used, the orange coating is Kapton tape, to insulate the coil from the metal box shielding it "R" is the major radius of the coil, "r" is the minor radius.

The Rogowski coil should not be placed over multiple current carrying wires, such as co-axial cables, where the currents flow in opposing directions, as the signal from one wire will cancel the other, leading to erroneous readings. The construction of the coil can be tailored to the expected signal, as the output is proportional to the size of the coil, the number of turns of the wire back over the loop, and the rate of change of the current.

Faraday's law tells us: $\oint E.dl = -{}^{d\phi_B}/_{dt}$ (Eq 2.1)

Using ϕ_B=∫B.dS, S=πr^2, ϕ_B=Bπr^2, where r is the minor radius of the loop the magnetic flux is passing through, B=μ_0I/2πR, where R is the major radius, Faraday's law can be rewritten as:

$$\oint E.dl = -\frac{\mu_0 \pi r^2}{2\pi R}\frac{dI}{dt} \quad \text{(Eq 2.2)}$$

The EMF induced in a loop is given by $\oint E.dl$, so setting A as the area of the minor loop, and N as the number of minor loops, we reach:

$$v(t) = \frac{AN\mu_0}{2\pi R}\frac{dI}{dt} \quad \text{(Eq 2.3)}$$

The resulting voltage, v(t), is proportional to the first derivative of the current. If a direct measurement of current is needed, an integrator must be added to the circuit. The frequency of the integrator should be higher than the frequency of the signal being measured. Integration by hardware at the point of measurement can mask signals that occur in timescales less than the integration time, such as breakdowns, and so it should be performed numerically in software rather than hardware if this is a likely occurrence, after the trace has been inspected. This approach enables post-facto analysis on data that could be otherwise missed. The above equations only apply when the minor radius is small compared to the major one, leading to a locally uniform field in the coil.

The coils used were 40 mm in major radius, 2 mm in minor radius, and had 7 turns, shown in figure 2.6. several factors can affect the calibration of a Rogowski coil, causing it to stray from the values calculated using the equations above, for instance, the fact that they are handmade may cause the radius of the turns to vary, and the inductance of the coil can cause errors to creep in if high speed signals are being measured. Another major source of error can be capacitive coupling of the coil to electric fields - hence an earthed housing is used to shield the probe, though such shielding requires an aperture for the cable to pass through in order to allow the field to penetrate the probe. Given the number of possible sources of error, the coils were calibrated using a Pearson Model 110 (0.1 V/A) current transformer to obtain a calibration factor.

In the experimental data, small offsets on oscilloscopes used to collect the data from the Rogowski coils occurred. These were carefully removed by inspecting the integrated data and removing any offset gradient, as shown in figure 2.7. The signal acquired during the short time before the trigger fires should be zero. As is evident in the left image of figure 2.7, it exhibits a pronounced slope. If the slope of this region is extrapolated for the duration of the full trace, it can then be removed from the measured signal, as seen in the right image in figure 2.7.

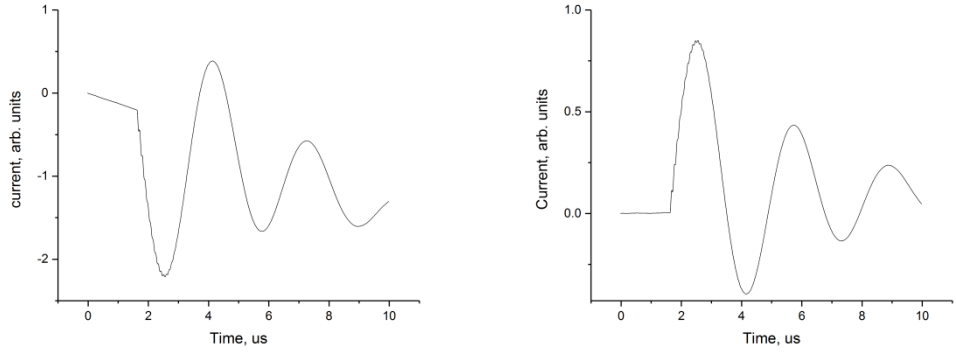

Figure 2.7: An example of an integrated Rogowski signal, showing the effects of scope offset on the signal leading to a decreasing baseline (left). By compensating for the offset by the addition of a counter-offset, the signal can be corrected (right). (Note: Right trace has also been inverted)

Using a pair of Rogowski coils, set in opposing directions can also help alleviate this problem, as the measured signal will give opposing traces, but any noise or coupling effects will give similar signals on both measurements, and so can be removed.

2.2.2: Interferometry

Interferometry is a technique that analyses the change in optical path length between two paths in a system, a reference path that undergoes no change, and a probe path. Light passes through both paths and when it recombines, it will do so either in or out of phase, leading to constructive or destructive interference. As the path length changes, the output varies between in and out of phase, leading to variations in the signal intensity.

The optical path length is a product of the physical path length and the refractive index of the medium the light is propagating through, so although the physical distance the beam is travelling remains unchanged, the optical path length changes as a result of the refractive index changing.

[2.9] covers the derivation of the refractive index of a plasma and the following section is a summarised extract of it. As the electric field from the beam of laser light interacts with electrons (ions move too slowly to respond to the variations in the field), the equation of motion for an electron moving with velocity v_e in the field of the beam is:

$$-e\vec{E} - \nu_{col} m_e \vec{V_e} = m_e \frac{d\vec{V_e}}{dt} \quad \text{(Eq 2.4)}$$

where $\vec{E} = \vec{E}_0 e^{i(\omega t - kx)}$ and ν_{col} is the electron collision frequency. The electron velocity as a result of being driven by the beam will be of a similar form, namely:

$$\vec{V}_e = \vec{V}_0 e^{i(\omega t - kx)} \quad \text{(Eq 2.5)}$$

The current density driven in the plasma can be derived as:

$$\nabla \times \vec{B} = -\epsilon_0 \mu_0 \omega \left(1 - \frac{n_e e^2}{(\omega - i\nu_{col})\omega \epsilon_0 m_e}\right) \vec{E} \quad \text{(Eq 2.6)}$$

which, using the plasma frequency equation, $\omega_p = \sqrt{\frac{n_e e^2}{\epsilon_0 m_e}}$, and assuming $\nu_{col} << \omega$, can be re-written as:

$$\mu_0 \vec{\boldsymbol{j}} = \nabla \times \vec{B} = -\epsilon_0 \mu_0 \omega \left(1 - \frac{{\omega_p}^2}{\omega^2}\right) \vec{E} \quad \text{(Eq 2.7)}$$

differentiation and substitution into the Faraday-Maxwell equation yields:

$$\nabla^2 \vec{E} = \epsilon_0 \mu_0 \left(1 - \frac{{\omega_p}^2}{\omega^2}\right) \frac{d^2 \vec{E}}{dt^2} \Rightarrow \nabla^2 \vec{E} = \frac{1}{c^2}\left(1 - \frac{{\omega_p}^2}{\omega^2}\right) \frac{d^2 \vec{E}}{dt^2} \quad \text{(Eq 2.8)}$$

from this, the wave velocity can be obtained from the wave equation to give the refractive index, η:

$$\frac{1}{v^2} = \frac{1}{c^2}\left(1 - \frac{{\omega_p}^2}{\omega^2}\right), v = \frac{c}{\eta}, thus\ \eta = \left(1 - \frac{{\omega_p}^2}{\omega^2}\right)^{\frac{1}{2}} \quad \text{(Eq 2.9)}$$

From the above, it can be seen that the refractive index of a plasma is related to the free electron density, n_e, within ω_p. If the probing frequency is too low, the beam cannot propagate through the plasma as the plasma is able to respond and screen out the EM fields of the beam. In this case, the beam will be repelled, and reflected. This is used, for instance, in a plasma mirror [2.10]. These can be used to remove pre-pulse from high power lasers, where the pre-pulse ablates a target, giving rise to a plasma, that then reflects the main pulse onto the main target. If the frequency is higher, the plasma cannot respond quickly enough, and the beam will propagate through the plasma. Near

the plasma frequency, the beam propagates only a few Debye lengths into the plasma, where its energy can be absorbed by the plasma, causing heating effects.

The refractive index of a plasma is also affected by the density of the neutral species, n_0. Neutrals are atoms (or molecules) that are not ionized and are generally present in plasma in varying degrees. The ratio of neutrals to ions is the ionisation ratio. In a plasma, the neutrals become ionised through collisions with other particles (ions, neutrals or electrons). A neutral can be in an "excited" state, where the atom sits in a higher energy state than its natural, ground state. The energy can come from collisions, or photon absorption. Excitation energies are lower than the energy required to liberate an electron from a neutral to make an ion and the incident beam interacts with the neutrals through the bound electrons forming an atomic dipole. Each energy state has a specific oscillation frequency associated with it.

Starting with an equation describing the displacement of each electron bound to an atom:

$$\vec{x}(t) = -\frac{e}{m_e(\omega_0^2-\omega^2)}\vec{E}(t) \quad \text{(Eq. 2.10)}$$

and summing over all the electron oscillators gives the polarisation of the atom:

$$P = n_0 \sum_j^M \frac{N_j e^2 \vec{E}(x)}{m_e(\omega_{0j}^2-\omega^2)} \quad \text{(Eq. 2.11)}$$

Using $\vec{P} = \vec{E}(\epsilon - \epsilon_0)$ leads to:

$$\epsilon = \epsilon_0 + n_0 \sum_j^M \frac{N_j e^2 \vec{E}(x)}{m_e(\omega_{0j}^2-\omega^2)} \quad \text{(Eq. 2.12)}$$

giving the refractive index:

$$\eta = \left(1 + \frac{n_0 e^2}{\epsilon_o m_e} \sum_j^M \frac{N_j}{(\omega_{0j}^2-\omega^2)}\right)^{1/2} \quad \text{(Eq. 2.13)}$$

Each electron will not have solely one ω_0, but rather multiple values associated with different transitions, $\omega_{0i,j}$, and it is necessary to sum over all possible interactions. α, the polarisabilty of the atom, is given by:

$$\alpha = \frac{e^2}{4\pi\epsilon_0 m_e}\sum_{i,j}\frac{f_{i,j}}{(\omega_{0i,j}^2-\omega^2)} \quad \text{(Eq. 2.14)}$$

Where:

$$f_{i,j} = \frac{32}{3\pi\sqrt{3}}\frac{1}{i^5}\frac{1}{j^3}\frac{1}{(\frac{1}{i^2}-\frac{1}{j^2})^3} \quad \text{(Eq. 2.15)}$$

In practice, $\eta \approx 1 + 2\pi\alpha n_0$ is used, calling on experimentally measured values for α. To completely calculate the refractive index from first principles is computationally intensive however, as the relation between each electron with each state needs to be considered, as well as quantum mechanical effects that couple transitions to electrons that could undergo them. [2.9, 2.11] provide a table of some typical polarisabilities, reproduced in table 1.

Atom	2πα
He	$1.3X10^{-24}cm^3$
H_2	$5.0X10^{-24}cm^3$
Air	$1.1X10^{-23}cm^3$
Ar	$1.1X10^{-23}cm^3$
Al	$4.4X10^{-23}cm^3$

Table 1: Typical polarisabilities

The refractive index of the plasma is a sum of the contributions from the electrons and the neutrals. The contribution to the refractive index of the plasma resulting from the presence of neutrals is positive, whereas the contribution from the free electrons is negative. In a plasma with n_e = $10^{18}/cm^3$, 10% ionisation, η_0 = 1.000110000 (for a laser wavelength of 1064 nm and assuming $2\pi\alpha$ = $1.1x10^{23}$ cm^3), η_e = 0.999999978. It is clear that the refractive index change due to atoms is much more pronounced than that due to electrons.

The detected signal is the sum of the probe and reference beams, $S_{det}=S_{probe}+S_{ref}$. As the beam is an EM wave, the electric field can be written as:

$$E_{tot} = E_i^{\,i(\omega t)}(E_i^{\,i(\phi_{probe})} + E_i^{\,i(\phi_{ref})}) \quad \text{(Eq. 2.16)}$$

Where ϕ_{probe} and ϕ_{ref} are the phase changes for the probing and reference beams respectively, E_i and E_{tot} are the incident and summed energy densities of the beam. The signal on a detector, such as a photodiode, is proportional to E^2 (as detectors tend to record intensity), which leads to:

$$E_{tot}{}^2 = \left(E_{ref}{}^2 + E_{probe}{}^2\right)\left(1 + \frac{2E_{ref}E_{probe}}{\left(E_{ref}{}^2+E_{probe}{}^2\right)}\cos(\phi_{ref} - \phi_{probe})\right) \quad \text{(Eq. 2.17)}$$

As the optical path length changes (which is a product of the physical path length and the refractive index), the phase difference between the reference and probe beams changes, leading to variations in the signal on the detector between zero and a maximum amplitude. The change in intensity of the interferometry signal leads to knowledge about the density of the plasma as the changing refractive index due to the plasma causes a variation in the phase shift in the probe arm. There are many different types of interferometry system, such as the Michelson-Morley, Mach-Zehnder, Fabry-Perot types. In this experiment, only the Michelson-Morley type was used [2.12].

2.2.2.1: The Michelson-Morley Interferometer

The Michelson-Morley (MM) type of interferometer features a double pass of the medium under study, which doubles the sensitivity of the measurement. This system also only requires one beam splitter, which can prove cost effective on large beam diameters. A beam enters a beam splitter at 45° and is split two ways. One way leads to a mirror only, acting as a reference beam. This beam reflects off the mirror and back to the beam splitter. The probe beam heads off to the plasma, passes through it, and is reflected back off a mirror on the far side, see figure 2.8. The two return beams then pass from the beam splitter to the detector, for example a high-speed camera. The beams are all co-linear. Fringes are created when the path lengths of the reference and probe beams differ.

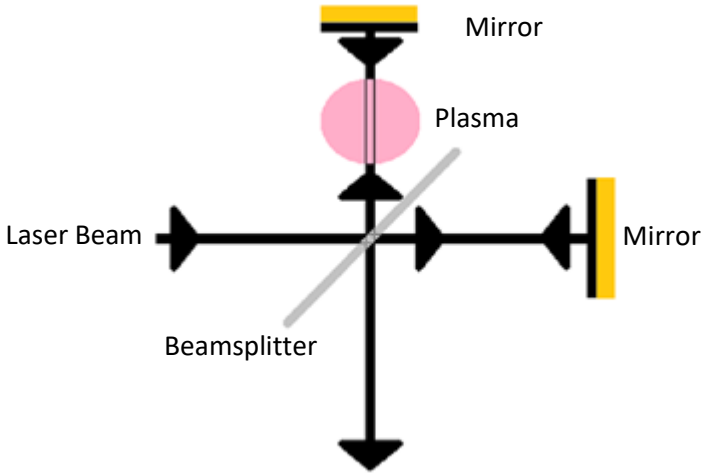

Figure 2.8: Schematic showing the configuration of the Michelson-Morley interferometer.

A misalignment of the arms can be added to the system, to create a series of fringes known as tilt fringes for the static case, where the path difference increases gradually across the field of view. When the refractive index changes in a portion of the area under study, the fringes then appear to distort. The change in density that leads to a refractive index change sufficient for a full fringe shift is called the fringe constant. The fringe constant is calculated using $\lambda n_c/\pi$, where n_c, the critical plasma density, is the density at which the beam cannot propagate through the plasma, given by $\varepsilon_0 m_e \omega^2/e^2$. For the wavelengths used in this study, the fringe constant at 532 nm is 6.65×10^{16} cm^{-2}, at 1064 nm it is 3.33×10^{16} cm^{-2} and at 1550 nm, it is 2.28×10^{16} cm^{-2}. Here we consider only the variation due to electrons.

Another big advantage of the MM configuration is that it is relatively easy to align, as it is obvious when the co-linear beams aren't aligned correctly (if the system is badly aligned, no fringes are visible, and tracing the paths of the beams shows where the error is. In a nearly-perfect configuration, fringes will be seen, but the fringe pattern will not be parallel). The optical path lengths of the two arms must not differ by more than the coherence length of the laser source used. If the coherence length is very short, the arms must be matched through the addition of compensating optics.

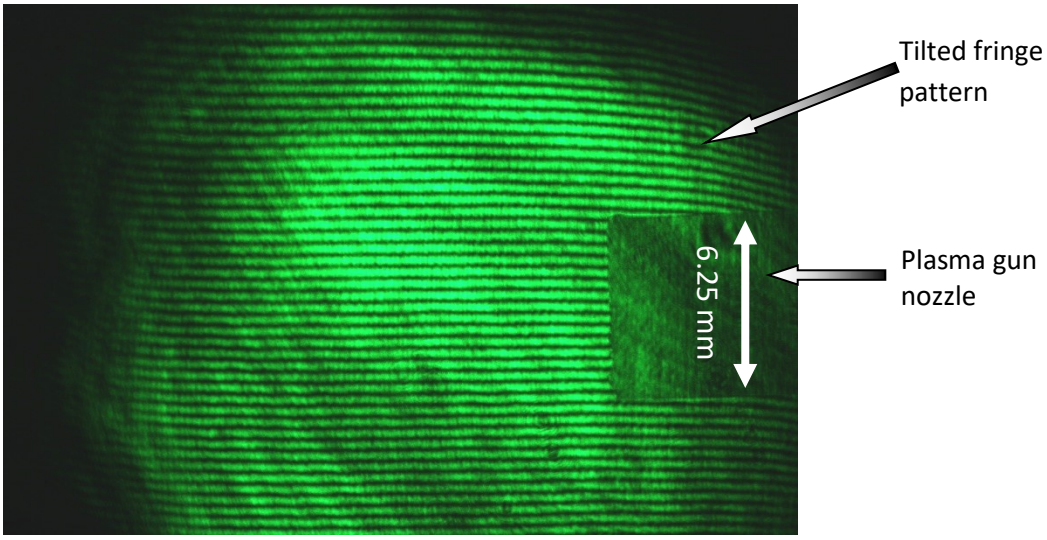

Figure 2.9: An example of a static shot interferometry image from MAGPIE, showing parallel tilt fringes. The image is green because it contains only light from the 532 nm laser used. Single image taken with dSLR camera and pulsed laser.

There are two modes of usage for interferometry, spatial or temporal. Spatial interferometry shows the variation of optical path length over an area. With good quality optics, and a well aligned system with a minute and deliberate misalignment, it is possible to create a tilt fringe pattern where the fringes are all straight and parallel. Most sources will not be perfectly collimated, for example a laser source will generally be a narrow beam that is spread by a divergent lens, and then collimated at the desired width. The divergent section of the path will introduce different path lengths that will give rise to fringes.

The measurement is made at a point in time by capturing the fringe pattern with a camera. Comparison with a unchanged fringe pattern, an example of which is figure 2.9, yields information on how the medium has changed. Figure 2.10 shows a comparison between the initial fringe pattern and one taken later in the plasma's evolution. If a single image is required, a digital SLR-type camera can be used with a pulsed laser, as is the case on MAGPIE, a pulsed power generator at Imperial College London used for plasma phenomenon studies [2.13]. As variations over the duration of the current pulse from the doghouses were to be studied, it was necessary to develop a multi-frame interferometer using a high-speed camera.

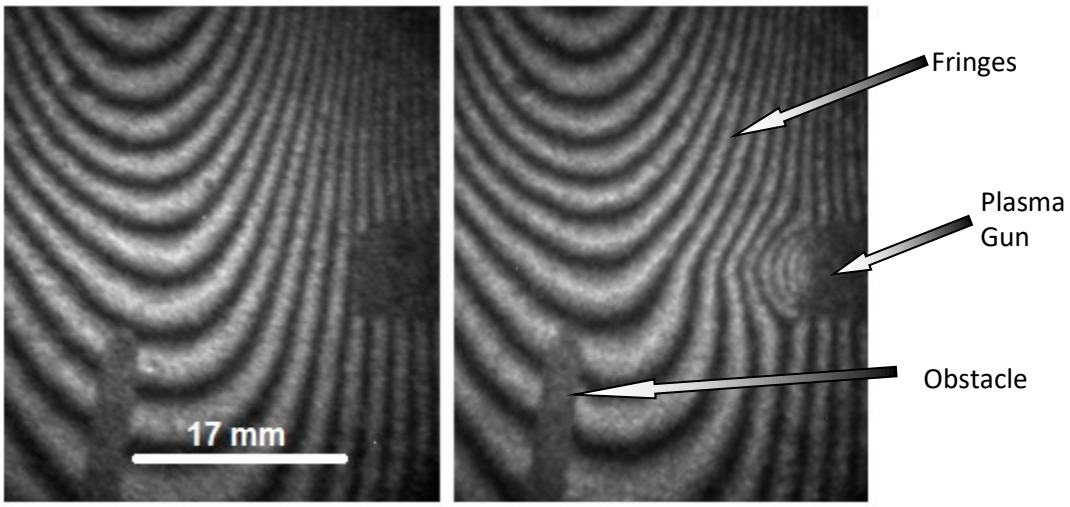

Figure 2.10: Spatial interferometry studies the movement of interference fringes before and after a plasma is generated. The left image is the static frame, taken before the plasma gun fires, and the second frame is taken a short time after the gun fires, and shows how the fringes change as the plasma evolves (only one gun used in this sequence).

The interferograms show how the density varies over space, but they do not inform about absolute densities, as the fringes shift relative to each other. A single chord temporal interferometer can be deployed, providing a continuous measure of plasma density at a specific point in space. A temporal interferometer was developed for this purpose.

2.2.2.1: Spatial Interferometry

The spatial interferometer, figure 2.11, was constructed as a Michelson-Morley configuration, with each arm being approximately 1 metre long. Measurements were taken using a high-speed camera, the Invisible Vision UHSI 12/24, capable of taking 12 frames at arbitrary timing with a minimum exposure time of 5 ns [2.14]. A CW laser is used to provide the light to the interferometer.

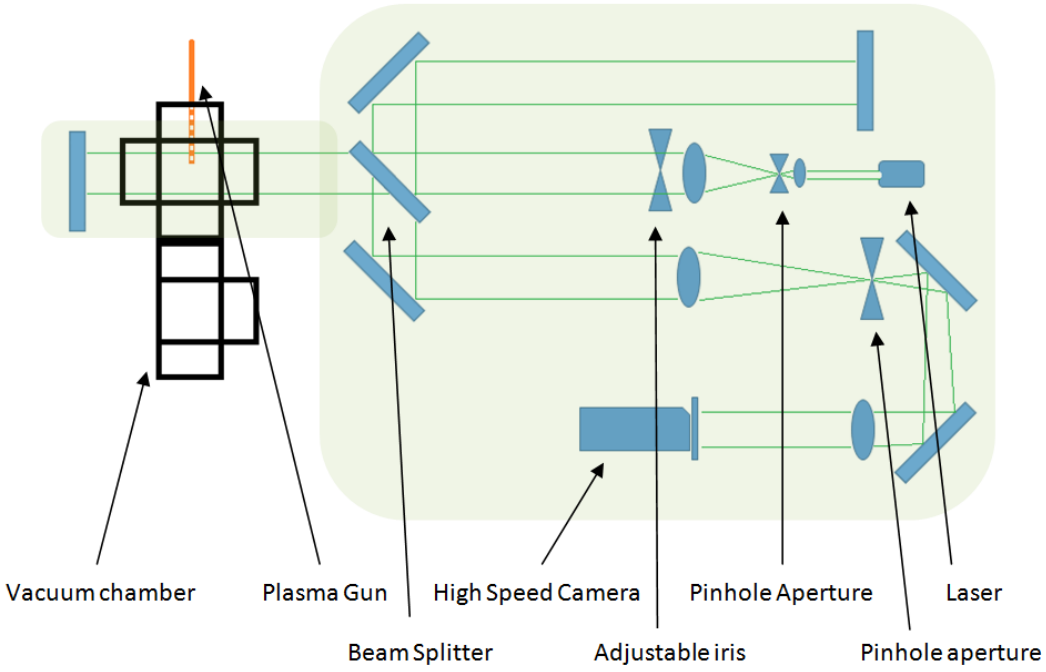

Figure 2.11: Schematic of the layout of the bench, showing how the alignment of the interferometer (denoted by the shaded area) passes through the chamber (shown in black) at the crosspiece. The plasma gun (orange) nozzle is inserted into the beam.

The camera is constructed from a CCD mounted behind a microchannel plate, or MCP. The MCP is made of many fine channels into which photons travel. The channels are angled away from the optical axis however, so it unlikely that a photon will traverse an entire channel. As they propagate down the channel, they collide with the wall of the channel and liberate an electron. There is a high potential applied between the walls of the channel, so they act to accelerate the electron along the channel, liberating more electrons when it, too, collides with the wall. This causes a cascade of electrons to be created from a small number of photons, leading to high sensitivity. In order to ensure that the frames are all of the same scene, a kaleidoscope lens is installed before the MCP, multiplying the instances of the scene across the device. Eventually, the electron cascade exits the channel, where it impacts on a phosphor screen, converting the electrons into light once more. The light is collected and focussed onto the CCD by a lens. By applying a well controlled high voltage pulse to different sections of the MCP, it is possible to cause a section to be powered, whilst the remainder of the MCP stays off. In this way, it is possible to obtain, in the case of the Invisible Vision UHSI 12/24, 12 images taken at different times. At the magnification factor the system is configured

with, the resolution of the image is roughly 15 pixels/mm. At the velocities the plasma is expected to travel at, 5-10 mm/μs, this equates to sub-pixel movement per exposure at even the lowest expected velocity, 0.7 pixels in a 10 ns exposure.

The camera timing is configured in software and uploaded to the camera over an ethernet cable. The camera requires only one external trigger, the rest of the timing is executed internally.

A small laser diode was originally used as the source for the spatial interferometer, an OdicForce three colour unit. Only powering one of the colours gave up to 80 mW of 532 nm laser light. A shutter was placed in front of it to prevent the high-speed camera's delicate internals overheating.

The quality of the beam was not very good from the small diode laser, with many bright spots and intensity variations. One method of improving the beam is to employ spatial filtering, where the beam is focussed down and passed through a small aperture before expanding and re-collimating the beam. This process filters out some of the unwanted higher frequency modes that may be present in the beam, improving its quality. The higher modes focus at larger radii than the main mode, and so are blocked by the aperture, a technique arising from Fourier optics [2.12].

This version of the interferometer had a field of view that was also too small to study the convergence of the plasma, spanning just ~20 mm, whereas ~50 mm was required as a minimum. Unsuccessful attempts to expand the beam were attempted, such as including a Galilean telescope arrangement [2.12] in the probe beam path, before the plasma chamber, to expand the beam on the way to the plasma and then shrink it on its way back. This system caused many reflections. The next option was to expand the beam further, before the interferometer, which leads to the brightness of the beam decreasing dramatically, leading to a need for longer exposures, which then allowed vibrations to begin causing challenges.

A significant improvement to the interferometer was made by exchanging the small 80 mW OdicForce for a 6.5 W Coherent Verdi V.5. The more powerful output could be expanded to a beam

75 mm wide, whilst still being much brighter, leading to an improved field of view that could contain the six plasma gun nozzles. As the exposure time is governed by the number of photons captured, an increase in the beam intensity means that exposure times could be much shorter, as little as 10 ns, rather than the longer times required for the OdicForce, which were in the region of 75-100 ns. Even if vibrations were causing equipment to vibrate, the images would not move enough to cause blurring in such a short time, as they would be occurring over much longer (~ms) timescales.

The Verdi laser source was delivered to the system through a single mode fibre, which was contained within metal armoured flexible conduit running from the enclosure containing the laser head and fibre launch system, figure 2.12. The single mode fibre ensures that higher order components of the beam are filtered out, giving an excellent beam quality. As the beam is focussed down to approximately 5 µm in diameter to maximise the energy transferred into the fibre, consideration is required concerning the energy density threshold of the face of the fibre. Tests elsewhere at Imperial college showed that this method can be applied successfully on systems with up to 20 W lasers for a short duration. With the Verdi on full power (6 W), between 4.5 and 5 W were measured at the exit of the fibre inside the interferometry enclosure, representing a significant increase in illumination over the original laser. The risk of damage to the camera is minimised by shuttering the beam before it enters the fibre, only exposing the fibre to the beam for a very short time, just 2 ms.The type of shutter used, a ThorLabs SH11, was found to only be capable of reliable operation down to 11 ms, below which it suffered bounce and increased variation of closure time. As a backup, in case the shutter should fail to close, a second shutter was included, just behind the first. By operating the shutters slightly out of synchronisation, adjustment of the timings enables them to provide a reliable opening time of just 2 ms. Figure 2.13 shows a comparison between images captures using the original and the improved interferometers.

In practice, images on the camera could be affected by the flash at the tip of each plasma gun, decreasing contrast of the image and potentially obscuring the interferometry fringe pattern.

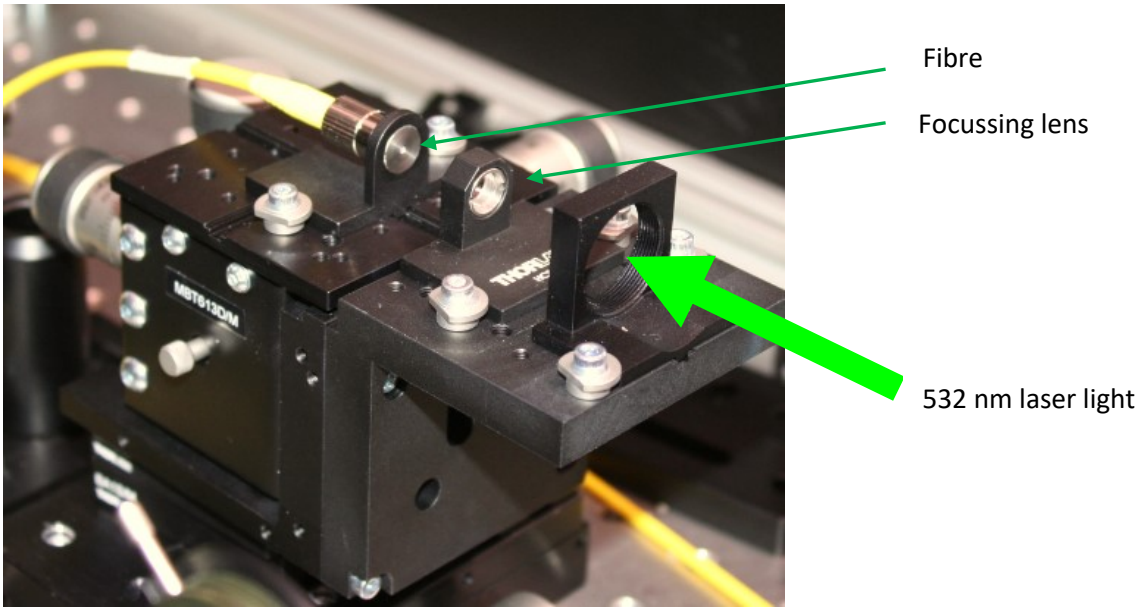

Figure 2.12: Using a Thorlabs MBT613D/M platform for fine 3-axis adjustment, and a Thorlabs A280-A (f=18.4 mm, NA = 0.15) RPO Aspheric lens to focus the laser beam, it is possible to inject the laser beam into the fibre, with very little loss.

Placing a small aperture at the focal point of the demagnification section of the interferometer solved the problem of the flash from the nozzle drowning out the interferometry signal. At this point in the optical path, the laser beam is focussed, and so passes through the aperture unaffected, but the light from the plasma guns is unfocussed, and so is almost entirely blocked, drastically reducing the flash and improving the quality of the image. Adding an aperture at this point in the optical path could give rise to inadvertent Schlieren effects [2.15], where the laser light is deflected due to gradients in the plasma density. The angle of deflection along x is given by:

$$\theta = \frac{\lambda^2 e^2}{8\pi^2 c^2 m_e \varepsilon_0} \int_0^l \frac{dn_e}{dx} dl \quad \text{(Eq 2.18)}$$

The integrated density gradient limit needed to meet the angle of acceptance can be calculated through manipulation of the above, and yields a maximum integrated density limit of 8×10^{18} /cm^2 at the distances in the inteferometer, before deflecting out of an aperture of 2 mm. At the nozzle, during a high voltage shot, the integrated density gradient is 2.3×10^{18} / cm^2. This value is close to, but not quite, the gradient to get full Schlieren effects, which could explain the lower contrast near the nozzles. The flash from the nozzle is further reduced by the addition of an interference filter, allowing only 532 nm light from the laser through it.

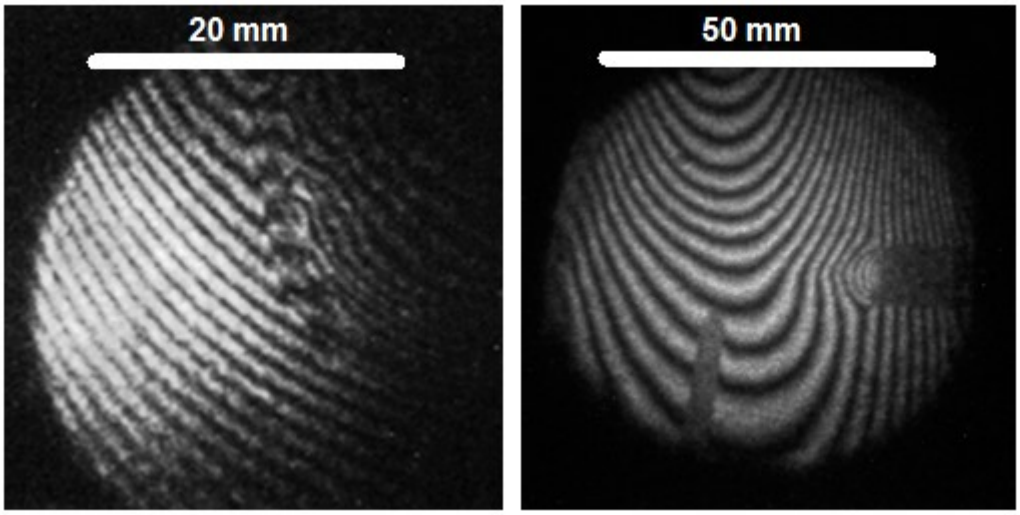

Figure 2.13: Comparison of the quality of the original interferometry frames acquired using the OdicForce diode laser system (left, 4.5 µs after trigger) with that of the new system Coherent Verdi based system (right, 3.27 µs after trigger), highlights the improvements made to the system. The nozzle is clearly visible on the new system, on the right of the image, whereas it had to be located outside the illuminated region on the old system

The optical table the interferometer was built onto was enclosed in a light-tight housing, constructed from a grey PVC designed for the purpose, to mitigate against the hazards of working with Class 4 lasers. The lid of the enclosure was wired into an interlock system.

Once the vacuum chamber was installed, extra sets of fringes were noticed, caused by the chamber windows. Their removal was achieved by tilting the chamber slightly, so that the reflections were not on the main optical path.

The interferograms are analysed by a process involving both manual and automated steps. The first step is to trace the fringes manually in Adobe Photoshop, and from this, generate maps of the fringes for each of the 12 frames. Once the fringes have been mapped, the images are passed into software written at Imperial College in Matlab, called Magic. The mechanics of Magic are introduced in [2.9]. In order for this to yield meaningful results, it is critical that the different frames are all perfectly aligned. In preparation for the automated stage, any regions within the image that do not contain fringes are masked off in grey. Fringes must be drawn in black, and the space between them must be white. Figures 2.14 and 2.15 show examples of fringe maps.

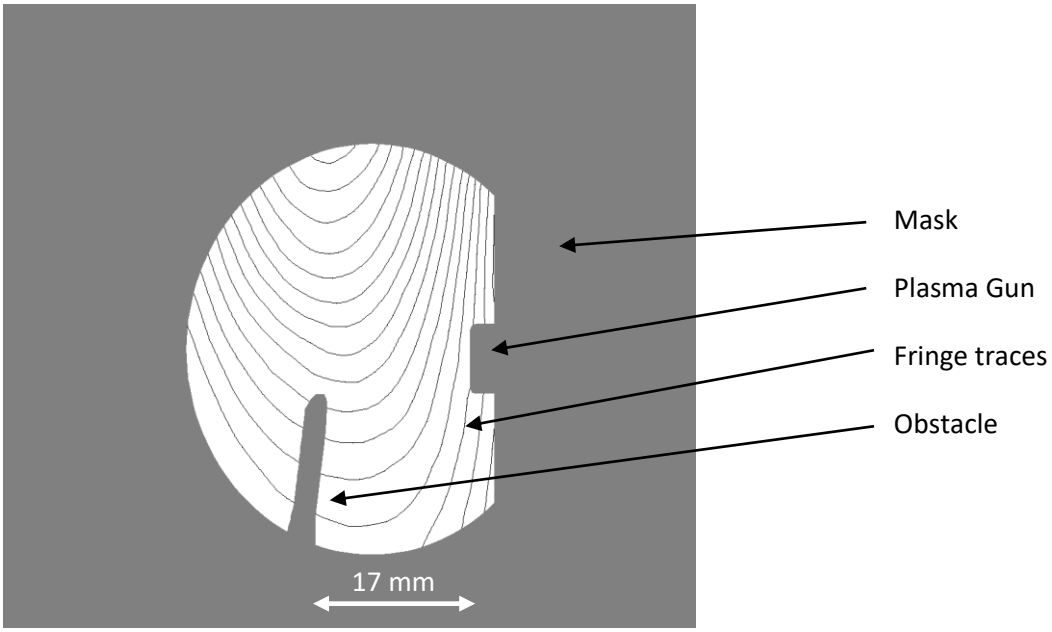

Figure 2.14: An example of a fringe map for a static shot

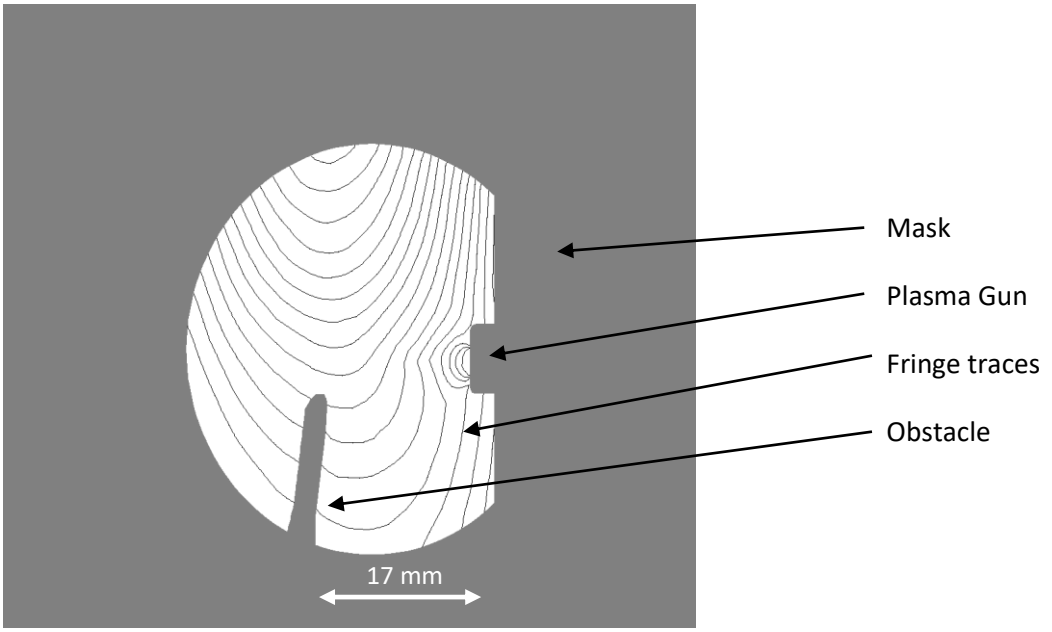

Figure 2.15: An example of fringe map showing moved fringes

Figure 2.14 shows the fringe map from the initial (unchanged) fringe pattern, and figure 2.15 shows a fringe map from a fringe pattern captured later on in the pulse. The comparison and calculation steps require the static fringes, and a fringe map from later on in the shot, showing the fringes having moved.

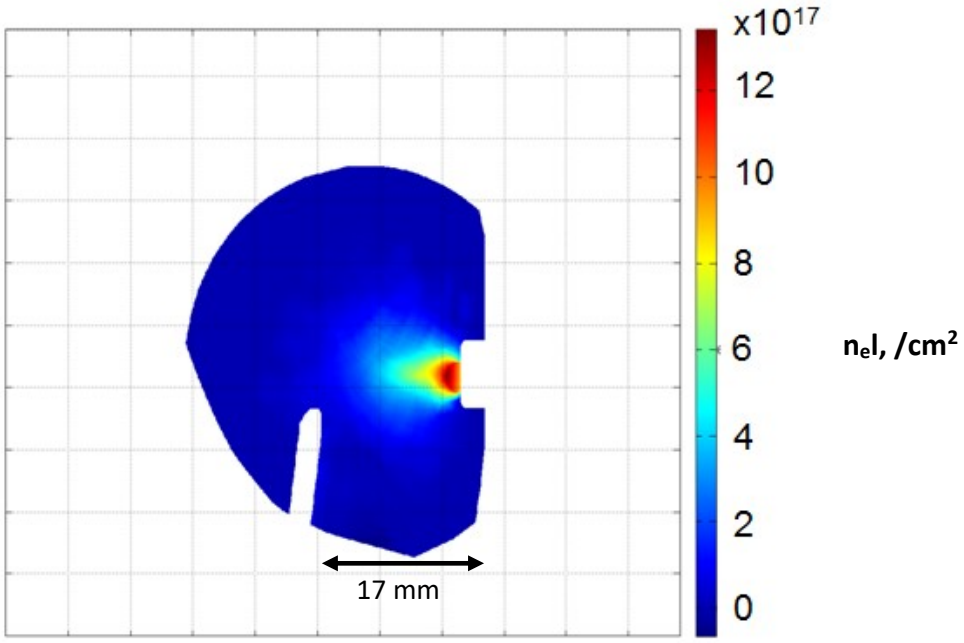

Figure 2.16: The density map acquired by analysing the above example fringes.

After fringes are identified and the phase shift extrapolated, Magic compares the two images to calculate the resulting plasma density, and it is then possible to plot density maps, such as figure 2.16, phase maps, and export the data for use in other applications, such as Origin. Analysis shows that this technique can contain several uncertainties. By far the largest error arises from the manual method of tracing the fringes. As can be seen in figure 2.17, it isn't totally clear where the fringes are at their brightest or darkest. It is marginally easier to trace following the dark fringes, but it is still very difficult to discern the exact point at which the trace should be drawn. On good contrast images, it could be considered that a reasonable error is as much as 1/8 of a fringe. On poorer images, this error increases dramatically. 1/8 of a fringe represents an error in $\int n_e dl$ of 8.3 $x10^{15}$ cm^{-2}. The lineout shown in figure 2.18 is a best-case example; it shows distinct fringe contrasts at the centre of the image. Towards the edges the contrast begins to deteriorate. Noise in the image also makes it more difficult to pick the correct point for the maximum and minimum of each fringe. In the example shown in figure 2.17, 1/8 of a fringe corresponds to approximately 5 pixels in the central zone. The variation in pixel value at the edges starts to become indistinguishable from noise, as this region is not as well illuminated.

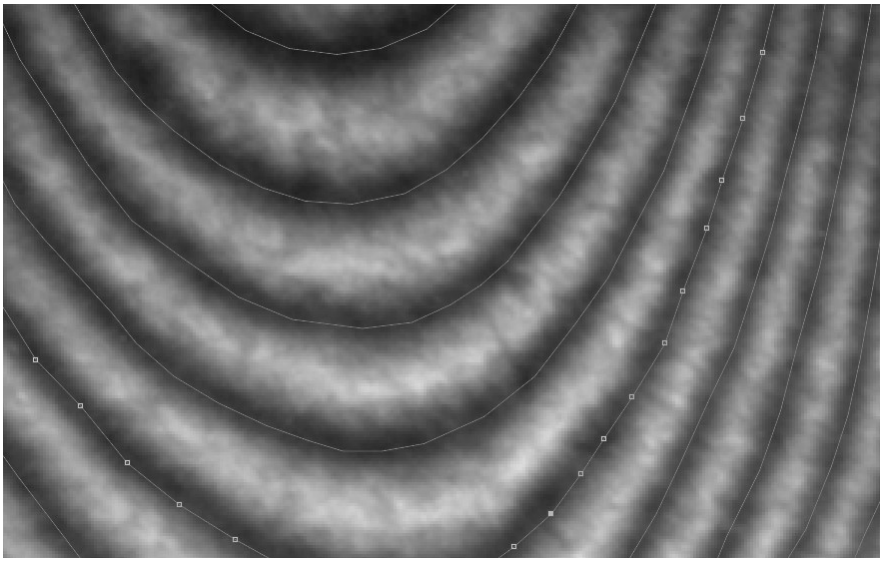

Figure 2.17: A section of an interferogram showing the manually traced fringes.

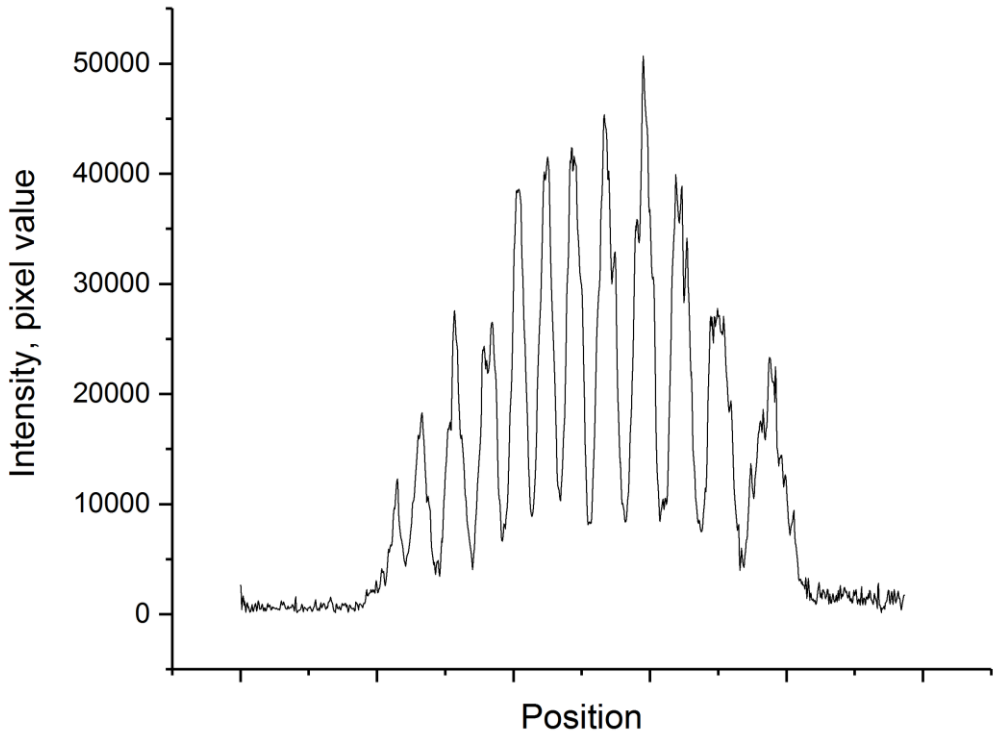

Figure 2.18: An example lineout from an interferogram

In regions where the density changes dramatically, such as the central point where the six guns converge, the fringes can become very muddled, increasing the errors dramatically. In these regions, it is sometimes better to mask off these zones rather than risk errors arising in other areas due to problems tracking the fringes.

The interferogram yields a 2D density map of line integrated densities. Imaging the plasma gun nozzle end-on, rather than from the side, showed that it initiates at a few locations, but very quickly becomes axisymmetric spreading around the entire circumference of the nozzle. If the assumption of azimuthal symmetry is made, it becomes possible to generate a density map through the process of Abel Inversion [2.16].

Despite the uncertainties associated with the analysis of the images, the spatial interferometer can yield very useful information about the plasma distribution. Adding multi-frame capabilities provides additional information on the behaviour of the plasma over time. There is not, however, an absolute zero defined anywhere in the interferogram. For this, temporal interferometry is called upon. Temporal and spatial interferometry techniques are often used together, as the temporal system can provide a known zero point, allowing for absolute values to be determined throughout the spatial interferograms. Without the zero point, the interferometry can only show relative changes.

2.2.2.2: CW Interferometry, aka Temporal Interferometry

Temporal interferometry uses a very narrow beam passing through the medium at a specific point, giving a chord measurement over a length through the medium. The output is captured by a light-sensitive time-resolved detector, such as a photodiode. The measurement is continuous in time, but specific in space.

Developments in fibre optic technology for the telecommunications industry have led to the existence of components that can be used to create a fibre-based interferometer, where the beams are completely enclosed in fibre until they exit into the medium under study. 1550 nm is usually used for this sort of system, as that's the wavelength used most frequently in the telecommunications industry, leading to more affordable components. Another advantage is that the sensitivity of the system increases with wavelength through the fringe constant, the line-integrated density change required to generate one fringe is $\lambda n_c/\pi$, where n_c is the critical density of the plasma = $\omega^2 m_e \varepsilon_o / e^2$ (remember that $\lambda = 2\pi c/\omega$). At 1550 nm, the fringe constant is 2.3×10^{16} / cm^2

(1064 nm leads to a fringe constant of 3.33×10^{16} / cm^2, 532 nm leads to 6.65×10^{16} / cm^2). For this experiment a Michelson-Morley based system was developed, figure 2.19, which utilised triature analysis [2.17, 2.18] to accurately determine small fringe shifts and whether the densities were increasing or decreasing. The laser for the system was an NP Photonics "The Rock" unit, 80 mW CW with a linewidth of 7 kHz, so very stable. Stability is important as any changes in the nature of the beam, such as its phase, will have an impact on the accuracy of the measurements made. A 90:10 splitter is the first component, providing a 10% reference signal and the 90% beam to send through the plasma. The reference path is fairly loss free, but the path through to the plasma and back is very lossy, so the majority of the signal is sent in this direction. Losses arise as the beam passes through the windows of the chamber, imperfect reflection off the mirror and imperfect connections of fibre sections for example. A large loss can arise from imperfect collimation of the beam when it exits the lens. If the lens doesn't collimate perfectly, the beam expands as a cone. This leads to some of it not being reflected back into the lens on its return journey. This signal is then passed into a circulator, a device which has three ports. The signal enters the device on Port 1 and exits from Port 2. It then exits the fibre and is collimated and sent through the plasma.

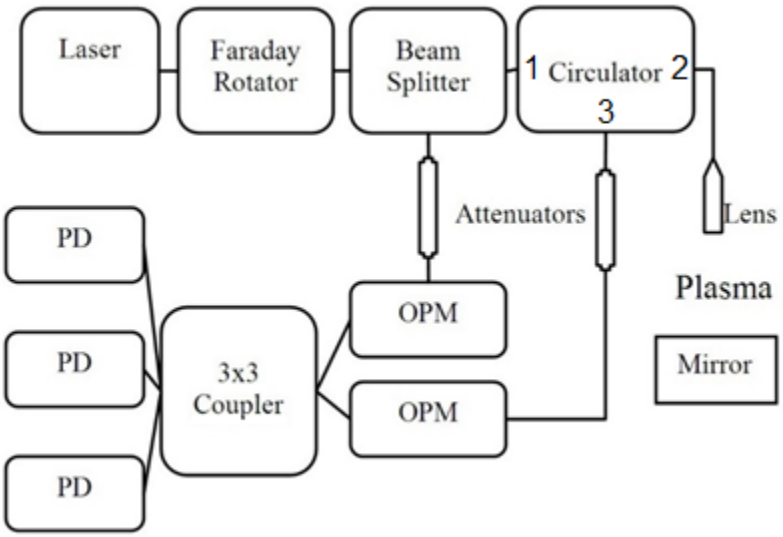

Figure 2.19: The modular construction of the triature interferometer

On the far side of the plasma is a mirror, reflecting the beam back through the plasma, and back into the collimator. The signal then re-enters the circulator on Port 2 and leaves on Port 3. They generally operate in a similar way to Faraday rotation isolation devices, relying on "non-reversible optics". The beam passes through a region that is subjected to a magnetic field. The plane of polarisation of the beam is rotated by the field and exits the device with the plane of polasization rotated. When it passes back through the magnetic field, the plane of polarisation is rotated once more, in the same direction as the first rotation, reinforcing the initial rotation, not negating it. The paths of the outward and return journeys differ as a result of a birefringent zone at either end of the magnetised region. As the beam has a different polarisation on the return leg of the journey, the path it follows differs as a result of the birefringent regions.

Other types of fibre-based interferometer exist, using just one channel. The single channel yields a time-varying signal, varying between a maximum and minimum value as the system detects movement through a fringe. When the signal is between maximum and minimum, it is possible to understand how the plasma density is changing. When it reaches a maximum or minimum value, however, it is not possible to know the direction it is changing, as shown in figure 2.20. In free space optics, this ambiguity is generally resolved by the use of a quadrature system, which uses two beams, 90° out of phase. When one of the signals is at a maxima or minima, its derivative is zero, but the other signal is in the most sensitive area with its derivative at a maximum. Quadrature systems are not all "in fibre" but a measurement technique known as "Triature" can be employed using a 3x3 coupler.

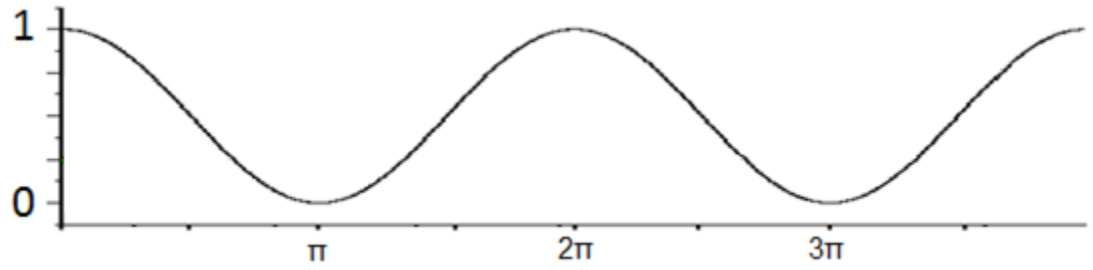

Figure 2.20: A single channel varies with phase difference, but as the signal passes through an inflection point, the direction of change becomes ambiguous.

In our system, the probing and reference arms are input to two of the three inputs of the 3x3 coupler [2.19]. Each input is coupled to all three outputs, and so the reference and measurement signals are combined onto each of the three outputs. Due to the alignment of the E field maxima in each of the fused fibres that the coupler is comprised of, the outputs are 120° out of phase with each other. As a signal changes between zero and maximum amplitude, it is obvious which way the signal is developing, as the other two signals are not at zero or maximum amplitude, figure 2.21.

The triature system provides three out of phase signals, which are then collapsed onto quadrature axes, and analysed using the THRIVE method outlined in the Sandia report by Scott and Dolan [2.9]. In a perfect triature system, the phase angle is the ratio of the three signals from the detectors, D1, D2 and D3, related by:

$$\tan(\emptyset) = \sqrt{3}\frac{D3-D2}{2D1-D2-D3} \quad \text{(Eq. 2.20)}$$

In a physical system, however, things are not quite so perfect. The nominally 2π/3 angular offsets between the three channels, referred to as lead and lag angles (taken relative to output 1) are rarely exactly so. The coupling between each of the three channels of the 3x3 coupler will not necessarily be unity, either. A characterisation phase is required prior to each measurement to quantify these variables before proceeding with the main analysis.

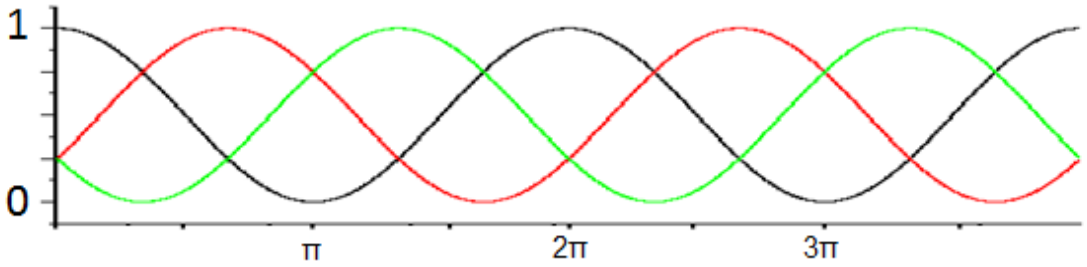

Figure 2.21: The triature system suffers no null points in the phase shift that are suffered by other fibre-based interferometers.

Characterisation is a step that is required to quantify the operation of the 3x3 coupler, which can vary slightly over time, thought to be caused by temperature fluctuations in the lab (this could be confirmed by placing the coupler in a temperature-controlled cabinet or on a thermoelectric plate). It is required before and after each experiment. The characterisation encompasses the behaviours of the entire system, not just the 3x3 coupler, but it is understood that the 3x3 varies the most over time. Characterisation requires that the system undergoes multiple full fringe shifts, in order to provide information on the behaviour of the 3x3 coupler, and the variation between minimum and maximum amplitude. Mapping the response through a full fringe allows the lead and lag angles, along with the coupling coefficients, of the channels of the 3x3 coupler to be measured.

If the system was coupled with exactly 2π/3 between channels, and a 1:1 coupling ratio, it would yield an ellipse like the synthetic example in figure 2.22. If the channels were 90° out of phase, the figure would be circular, at 120° an ellipse forms. Proper system characterisation requires the system undergoing multiple fringe shifts so that the analysis software is able to identify the coupling co-efficient and phase shifts between the three channels. A pair of ellipses is created, showing both the angle and coupling co-efficient between detector 1 and 2, and detector 1 and 3. In a system with a good signal to noise ratio, the line denoting the ellipse is quite narrow, but gets broader as the ratio decreases, making it more difficult to see where the ellipse's fit should lie. If the vibrations only pass through a small part of a fringe, the elliptical fit fails because the fit is bounded by the width of the partial ellipse's line.

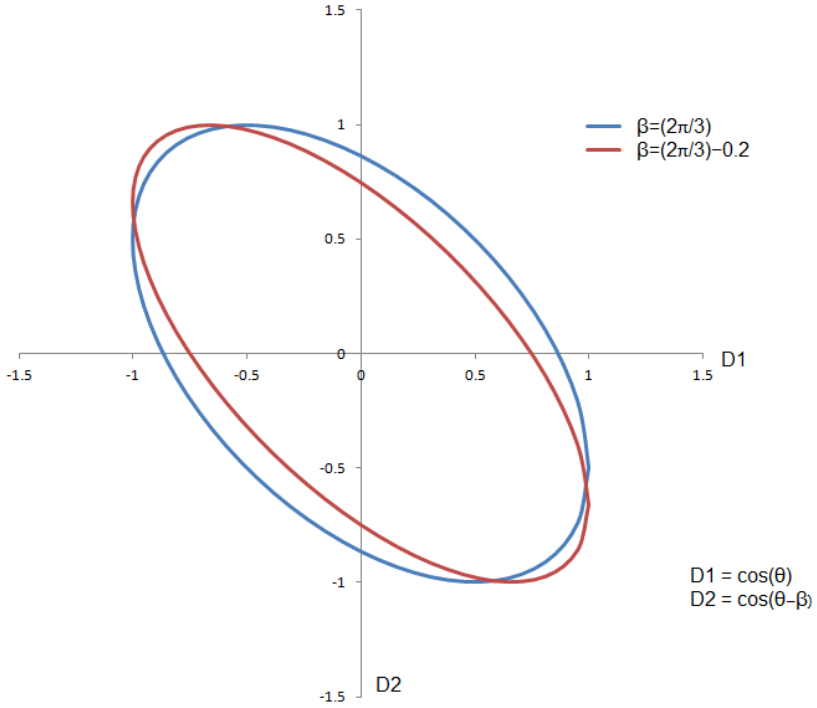

Figure 2.22: A (normalised) synthetic example of a perfect coupling between two channels. Also shown is the result of a slightly different lead / lag angle.

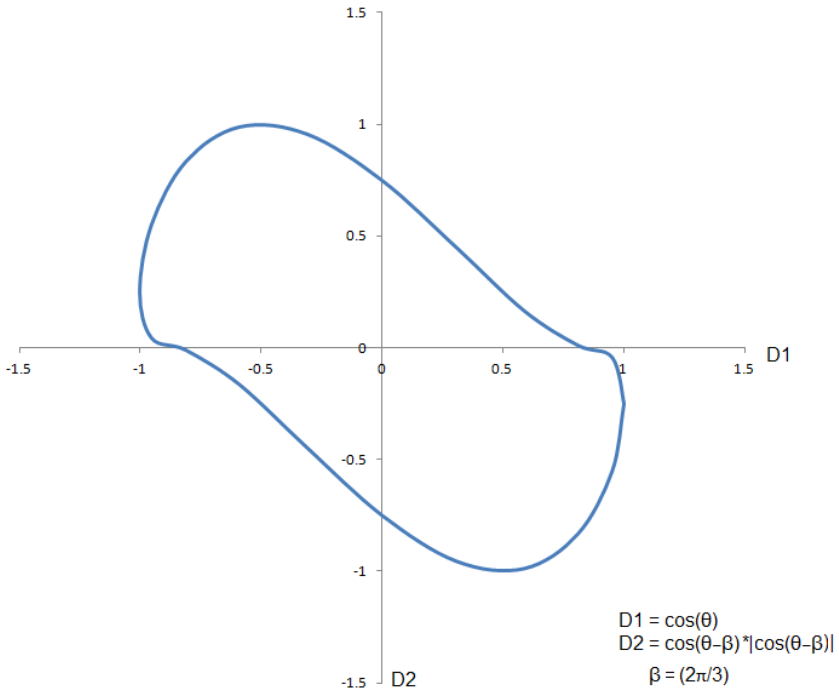

Figure 2.23: A synthetic example showing the ellipses in a system demonstrating a non-linear response over the phase range. In this example, this was induced by simply multiplying the signal by the absolute value of itself.

In the case where only a low power is detected, the ellipse begins to acquire straight sides, giving rise to, say, a triangle with rounded vertices. This behaviour is due to the fact that the 3x3 coupler relies on the EM field of the optical signal in one channel passing through into the other channels. As

the signal strength reduces, the coupling between channels deteriorates. Figures 2.22 and 2.23 show synthetic examples of an ellipse from a modified detector response.

In the case where the signal decays rapidly, the ellipses take a spiral form, which also precludes characterisation. Characterisation depends on the detector in use. Simple DC bias detectors, such as ThorLabs Det01cfc are sensitive to DC components of vibrations so it is possible to characterise the system using low frequency mechanical vibrations. The signal from these detectors can be very low though, making their use in these experiments difficult. Amplified detectors, such as the MITEQ DR-125-G, incorporate a DC block which makes characterisation much more difficult.

Figure 2.24 shows a good characterisation ellipse at the top, where the signals combine to form a well-defined ellipse. The middle and lower examples show very interesting poor ellipses. These were obtained when trialling a technique using a piezo fibre stretcher to minutely alter the length of the fibre to induce a phase shift. At present, the behaviour demonstrated in these examples is not fully understood. It is thought that the voltage used to power the crystal was too low to properly deform it, and so it was not stretching the fibre in a useful and stable manner, disrupting the phase stability of the signal. The behaviour seems to be a quite extreme non-linear response, coupled to a varying offset angle. Further work is planned to investigate this though this will not be as part of this study.

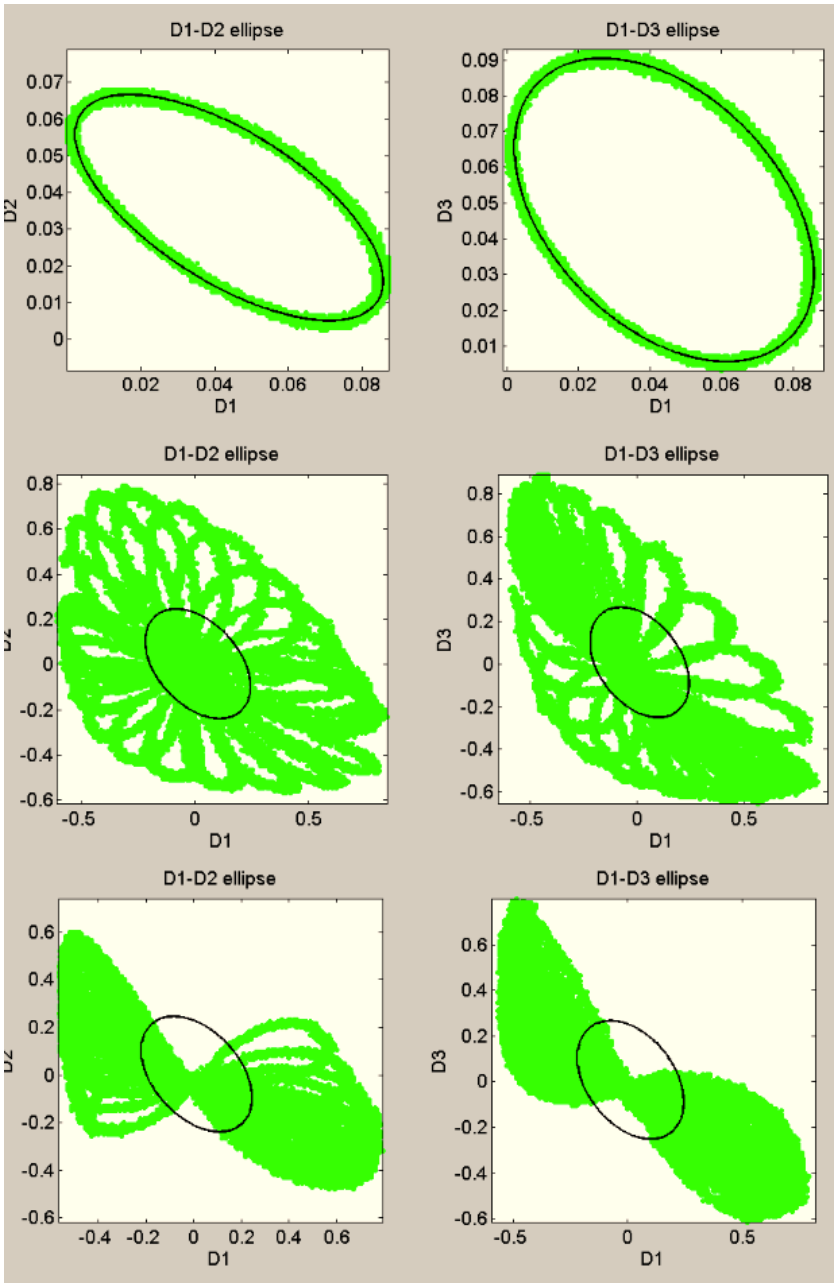

Figure 2.24: The uppermost image shows a typical pair of successful characterisation ellipses. The other two pairs are examples of failed characterisations.

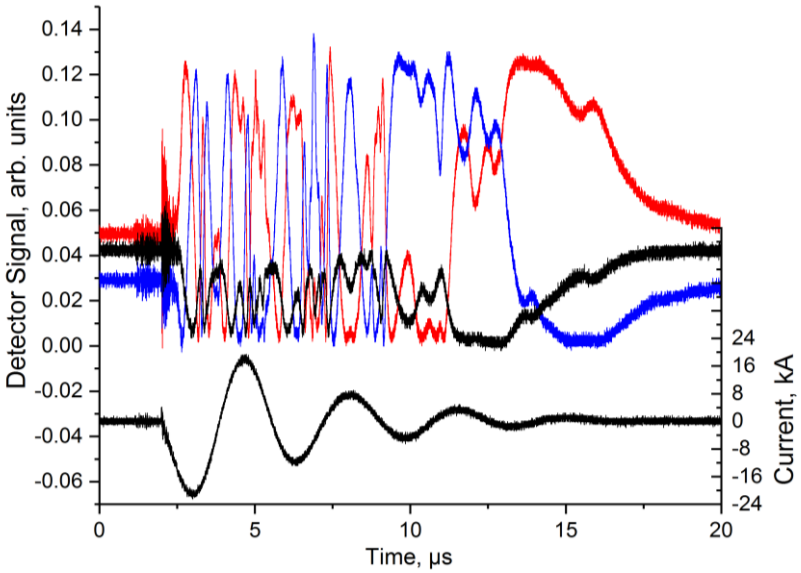

Figure 2.25: The raw signals from the triature photodetectors indicate a captured event, though its precise nature is not immediately obvious.

Once the system has been characterised, measurements can be taken. In the case of a plasma gun output a set of signals like those in figure 2.25 can be obtained. Using the THRIVE method, the three signals are combined to provide a trace of how the phase varies. By multiplying the phase shift by the fringe constant, the line-integrated density can be calculated using the method outlined in [2.18], as shown in figure 2.26.

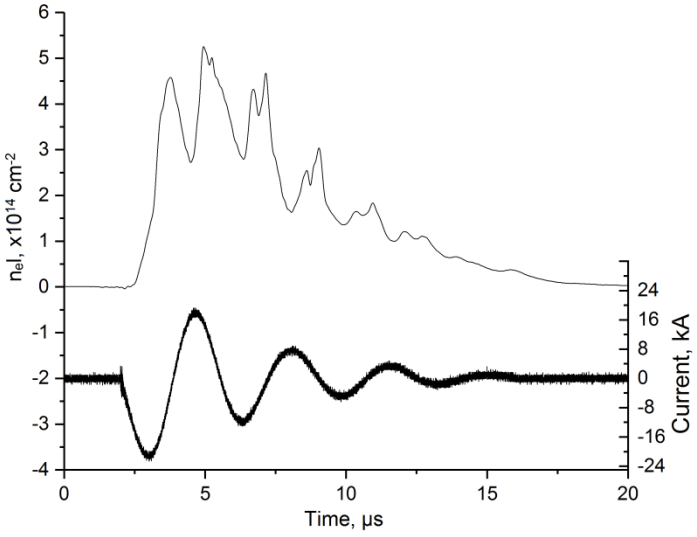

Figure 2.26: An example of the processed triature signal giving line-integrated electron density, nel. It is assumed that there are no neutrals present.

2.2.2.3: Dual wavelength CW Interferometry

The CW interferometer provides a time-resolved, continuous measure of the changing refractive index of the probed region. As shown earlier, the refractive index is composed of the effects from electrons and neutrals, $\eta = \eta_{med} - \eta_e + \eta_0$ (where η_{med} is the refractive index of the medium before any plasma is generated). If only a single wavelength is used, it is not possible to discern the individual changes, only their combined effects. By adding a second system operating with a different wavelength, two measurements are made, whereby they will differ as a result of the electron density refractive index change being different for each wavelength, due to the differing n_c values, which are dependent on the probing laser frequency. It now becomes possible to separate the two effects, and better understand the medium under study. Electron density increases lower the refractive index, whereas neutral density increases increase it. The result obtained from interferometry is thus dependent on the wavelength used. This can be exploited by the use of two wavelengths to make interferometry measurements. Over the course of the thesis a second fibre laser a 1064 nm, 110 mW Rock laser was utilised to investigate the possibility of fielding a two colour system.

There are several approaches to separating neutral density and electron density.

Method using the Drude model and Gladstone-Dale constant

[2.20] derives a set of equations in their paper using two wavelength interferometry to study discharges in air. [2.21] also uses these questions to calculate the electron and neutral densities. They start by using the Drude model [2.22] to find the free electron polarisability, which they simplify using the fact that the probing laser frequency is significantly greater than the electron-neutral collision frequency:

$$\vec{P}_f = -\varepsilon_0 \frac{r_e \lambda^2}{\pi} n_e \vec{E} \quad \text{(Eq. 2.22)}$$

where $\vec{E}$ is the electric field of the laser.

Next, they consider bound electrons as harmonic oscillators, oscillator strengths f_k associated with the k^{th} resonance ω_k:

$$\vec{P}_b = \frac{e^2}{m_e}\left(n_i \sum_{k_1} \frac{f_{k_1}}{\omega^2{}_{0,k_1} - \omega^2} + n_n \sum_{k_2} \frac{f_{k_2}}{\omega^2{}_{0,k_2} - \omega^2}\right)\vec{E} \quad \text{(Eq. 2.23)}$$

They neglect the first term of the right-hand side of the equation because they assume low ionisation levels, meaning $n_0 >> n_i$, and ionic polarisability is less important than that of the neutrals. These simplifications lead to:

$$\vec{P}_b = \varepsilon_0 \frac{r_e}{\pi} n_0 \sum_k f_k \frac{\lambda^2 \lambda^2{}_{0,k}}{\lambda^2 - \lambda^2{}_{0,k}} \vec{E} \quad \text{(Eq. 2.24)}$$

as their laser has a weak intensity, and the plasma is not magnetised, they consider it to be locally linear and isotropic, which gives:

$\vec{P} = \varepsilon_0(\varepsilon_r - 1)\vec{E}$, where ε_r is linked to the plasma's optical refractive index by $\varepsilon_r = \eta_p^2$:

$$\eta_p^2 = \frac{r_e \lambda^2}{\pi} n_e + \frac{r_e}{\pi} n_0 \sum_k f_k \frac{\lambda^2 \lambda^2{}_{0,k}}{\lambda^2 - \lambda^2{}_{0,k}} \quad \text{(Eq. 2.25)}$$

$$\eta_p \approx 1 - \frac{r_e \lambda^2}{2\pi} n_e + \frac{r_e}{2\pi} n_0 \sum_k f_k \frac{\lambda^2 \lambda^2{}_{0,k}}{\lambda^2 - \lambda^2{}_{0,k}} \quad \text{(Eq. 2.26)}$$

The rightmost term is almost wavelength independent, and equal to $\beta n_0/n'$, where β is the dimensionless Gladstone-Dale constant, $\eta = 1+\beta$ at a particular neutral density, n'. The authors calculate a value of 2.7×10^{-4} for $n' = 2.47 \times 10^{25}$ m^{-3}. Using the Gladstone-Dale relation, eq 2.26 simplifies to:

$$\eta_p = 1 - \frac{r_e \lambda^2}{2\pi} n_e + \frac{\beta}{n_0} n_0, \quad \text{(Eq. 2.27)}$$

which leads to the phase change of the probing laser beam due the change in the refractive index, n_p:

$$\Delta\varphi(\lambda) = \frac{2\pi}{\lambda}\int_{s_1}^{s_2}\left(\eta_p(\lambda) - 1 - \beta\right)ds \quad \text{(Eq. 2.28)}$$

For two wavelengths, the contributions of the free and bound electrons can be separated:

$$n_e L = \frac{1}{r_e}\frac{\phi_{1550}\lambda_{1550} - \phi_{1064}\lambda_{1064}}{\lambda_{1064}^2 - \lambda_{1550}^2} \qquad n_0 L = \frac{\rho_0}{2\pi\beta}\frac{\phi_{1550}\lambda_{1064} - \phi_{1064}\lambda_{1550}}{\lambda_{1064}/\lambda_{1550} - \lambda_{1550}/\lambda_{1064}} \quad \text{(Eqs. 2.29 and 2.30)}$$

Method using polarisabilities

A different set of equations is presented in a paper studying laser ablation of graphite targets [2.23]:

$$\varphi_1(t)\lambda_1 = 2\pi L\alpha_0(\lambda_1)n_0(t) - \alpha_e(\lambda_1)n_e(t) \text{ (Eq. 2.31)}$$

$$\varphi_2(t)\lambda_2 = 2\pi L\alpha_0(\lambda_2)n_0(t) - \alpha_e(\lambda_2)n_e(t). \text{ (Eq. 2.32)}$$

These equations rely on knowing the polarisability of the electrons and the neutrals, α_e and α_0 respectively. The electron and neutral polarisabilities are given by:

$$\alpha_e \approx -\frac{r_e\lambda^2}{2\pi} \text{ (Eq. 2.33) and}$$

$$\alpha_0(\lambda) \approx \frac{r_e}{4\pi}\sum_m \frac{f_{m_0}\lambda^2}{1-\left(\lambda_{m_0}/\lambda\right)^2} \text{ (Eq. 2.34)}$$

Where f_{m0} is the strength of the absorption transition oscillation from the m^{th} state to the ground state.

In the triature system, it was possible to add a second system reasonably easily, using components made to operate at 1064 nm. The two interferometers were joined into one path by using a bespoke 1064 / 1550 nm splitter / combiner. Commercially available components called Wavelength Division Multiplexers (commonly referred to as WDMs) exist. WDMs combine a range of wavelengths into one fibre. They do not normally cover such a large range as is used in this experiment though, usually just covering a wavelength range in the region of one or two nm. This is a very lossy method, in that each pass through this device passes 50% of the beam into the other channel, where it is rejected. This is a loss that cannot be avoided when using standard couplers, and just needs to be

factored in when purchasing the lasers. An achromatic collimating lens assembly, available from ThorLabs, was used to collimate both the 1064 and 1550 nm beams (achromatic lenses are designed to focus all different wavelengths within a broad range to the same point, something "ordinary" lenses cannot achieve).

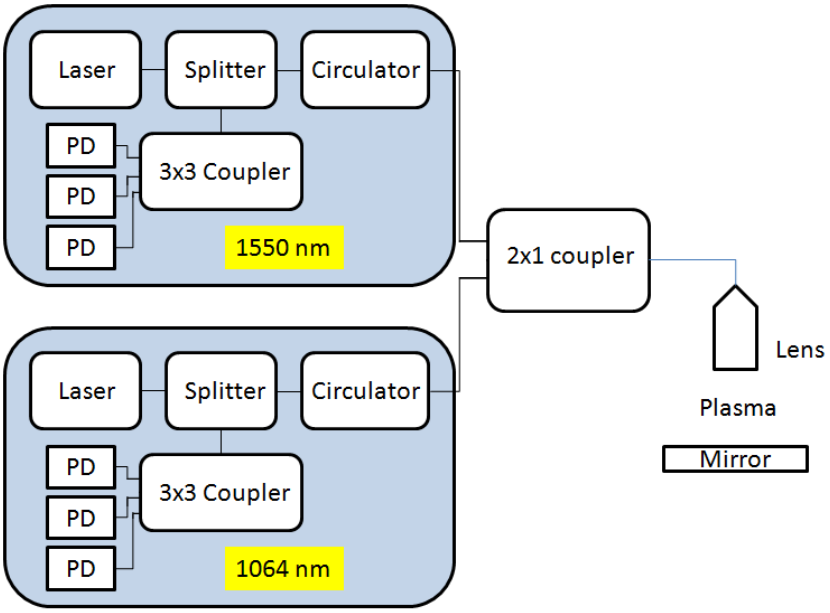

Figure 2.26: The integration of two wavelength systems was enabled by the bespoke coupler.

2.2.3: Spectroscopy

Whilst interferometry can give details on electron and neutral densities, spectroscopy can give details on temperatures of species in the plasma, as well as details on ion species present. It is capable of temporal and spatial resolution. Spectroscopy is a non-invasive method of measuring the state of atoms in a plasma by studying the emitted / absorbed radiation between their quantum energy levels.

Spectroscopy studies the nature of the light emitted or absorbed by the plasma. The state of an electron bound to the atom is described by a quantum wavefunction, which can only take a definite number of values, known as eigenvalues. Each eigenvalue relates to a specific energy level. Through spontaneous emission, when the electron relaxes to a lower energy level, a photon is emitted,

through the relation $E_{final} = E_{initial} - h\nu$. The difference in energy between states the electron can assume very specific values, leading to very specific wavelength emission [2.24].

An atom will have a collection of electrons in various configurations and changes its state through electrons gaining or losing energy. The ground state is the electron's most stable one, and it can acquire a higher energy state through collisions with other particles, or by absorbing an incident photon of the correct energy. Once excited, the atom will eventually relax, emitting the excess energy at a characteristic wavelength.

As the temperature and density of a plasma increases, the emission/absorption wavelengths gradually transition from well-defined peaks to broadened ones. Doppler broadening [2.22] captures information about the average movements of the atoms in the plasma and so relates to the temperature. If the particle is moving away from the detector, the emitted wavelength is Doppler shifted to a longer wavelength than the wavelength associated with the peak. If the particle is moving toward the detector, the wavelength is shortened. Averaging over the population leads to the specific emission peak becoming a narrow distribution centred on the specific wavelength, rather than a single narrow line. The width of the distribution tells us about the velocities of the particles. If there is a general biasing of the movement, such as would be caused by ion drift, this shows up as a shift of the central peak. Another cause for line broadening is collisional broadening, also known as pressure broadening. Atoms are perturbed by their neighbours, the EM fields giving rise to changes in the energy levels through the Stark effect [2.25]. Energy levels (and hence lines) can also be split in the presence of magnetic fields, known as the Zeeman effect [2.26]. Ions and neutrals tend to dominate these effects, as the scattering is performed by electrons bound to them, divulging information about the underlying conditions.

Instead of installing a spectrographic diagnostic in the lab, a suitable system already present on the MAGPIE pulsed power facility at Imperial College [2.27] was used. On this system, the light is gathered by optics focussing it into a bundle of optical fibres, which allows for a line of points in the

plasma to be studied. The fibres transport the signal to the spectroscope, an Andor spectrometer. There are 14 fibres in the bundle, spanning 3.5 mm. Light emitted from the plasma is collected from 2.5 mm along the axis of the ejection, starting near the nozzle.

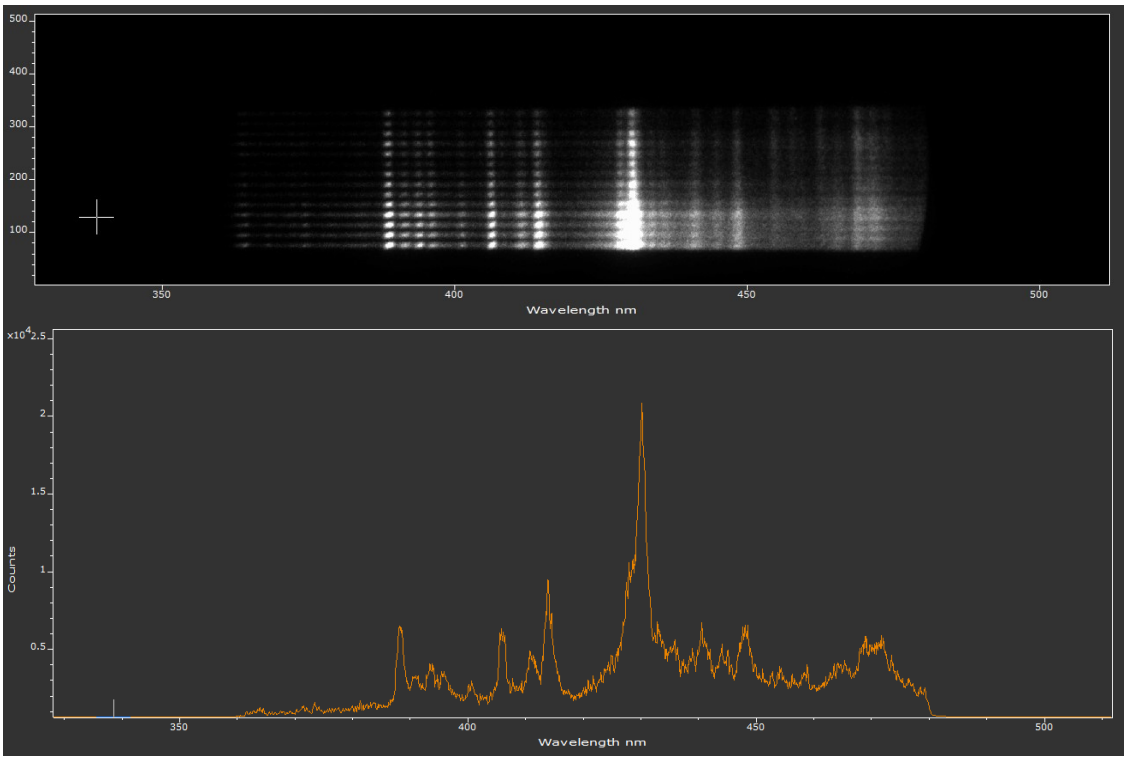

Figure 2.27: An example spectrograph as presented in Andor's Solis software, each horizontal line represents one fibre's input (in this example the cross in the upper image marks the fibre), spread over a range of wavelengths, 350-500 nm, taken using a 300 line/mm grating, 2.7 µs after the plasma gun fired. The bottom trace was closest to the nozzle.

The heart of the spectrometer is a diffraction grating with 300 lines/mm that splits the light into its components, which are then recorded by an Andor iStar CCD. An example of the data acquired is shown in figure 2.27. The captured image is then analysed in special software, such as Andor's Solis [2.28], and lineouts can be taken, yielding a wavelength vs intensity plot. The same device is utilised in the Thomson scattering diagnostic, but with a much finer grating of 2,400 lines/mm.

2.2.4: Thomson scattering

Thomson scattering is a technique used to understand the populations of species in a plasma. It is possible to gain knowledge of the electron density and temperature, and in some cases, the ion density and temperature. It is understood from previous work at Imperial College that there should be a measurable effect at plasma gun densities where $n_e = 10^{15} – 10^{18}$ /cm^3 [2.29].

The EM radiation, for example laser light, impinges on a charged particle (for example, an electron), leading to an exchange of energy. The incident wave causes the particle to oscillate, which affects the outgoing wave, essentially acting as elastic scattering. As the particle is already in motion, it "sees" a Doppler-shifted incident wavelength. The wavelength of the scattered light is also slightly shifted, according to the velocity of the scattering particle. The Thomson scattering cross-section [2.30], a measure of the likelihood of a photon being scattered by an electron is given by:

$$\sigma_{Th} = \frac{8\pi}{3} {r_e}^2 = 0.655 \times 10^{-24} cm^2 \quad \text{(Eq 2.35)}$$

The method relies on light being scattered off particles in the plasma. The detected signal is a compound of various factors, such as the amount of light entering the volume under study, the size of the volume under study, the likelihood of it scattering off something, and the likelihood of that scattered signal entering the detector. To increase the chance of a detection, a powerful, though brief, burst of laser light is used. Increasing the laser power increases the number of photons that may be scattered, thereby increasing the chance of a photon being scattered in the direction of the detector. The easiest way to gauge the likely output of the diagnostic is by simulating the result using software [2.31].

The scattered spectrum, generally denoted as S(k,ω), is comprised of two components, the electron and ion components, $S_e(\mathbf{k_s},\omega)$ and $S_i(\mathbf{k_s},\omega)$ respectively, where k_s is the scattered wavevector.

Incoherent scattering arises when the incident light is scattered off individual electrons, conveying information about their density and temperature. The individual interactions occur because the Debye length, λ_D, the distance below which electrons act to screen the ion's charge, is greater than the wavelength of the probing beam, and so the beam interacts directly with the electron. This is also referred to as non-collective scattering. The scattering is random, and so the recorded signal is a sum of all of the individual electron contributions. When the Debye length is shorter than the wavelength of the probe beam, it interacts with the electrons collectively, responding to the nature

of the charge they are screening. The collectively scattered signals from the electrons shielding the ions tend to dominate the recorded spectrum. This behaviour can be described by a parameter called the scatter factor, α, given by:

$$\alpha = \frac{1}{k_s \lambda_D} \approx \frac{\lambda_0}{4\pi\lambda_D sin\frac{\theta}{2}} \quad \text{(Eq. 2.36)}$$

where θ is the scattering angle. For $\alpha << 1$, large angle scattering, the probing wavelength is less than the Debye length. For $\alpha >> 1$, the wavelength is longer than the Debye length and so the scattering occurs from many electrons, acting together, screening the ions' charge. The final spectrum is a combination of the spectrum acquired from the scattered signal from the free electrons, and that from the electrons which are tied to the motions of the ions they are screening:

$$S(\mathbf{k_s},\omega)=S_e(\mathbf{k_s},\omega)+S_i(\mathbf{k_s},\omega) \quad \text{(Eq. 2.37)}$$

In summary, as α increases, the spectrum alters, initially containing only a single broad electron feature, perhaps with a small sharp ion peak embedded on it, through to two very distinct side peaks. Each feature conveys information through its form. The distance of the side peaks from the central one gives information on electron densities, and the shape of the peak yields temperature. In non-collective scattering, the central peak becomes widened due to the contributions of the random motions of the electrons.

[2.32] proposes a theoretical spectrum and [2.29] provides a concise summary of it in a paper describing the Thomson scattering diagnostics fielded on Magpie. According to these sources, the theoretical spectrum can be written as:

$$S_e(\boldsymbol{k_s},\omega) = \frac{1}{\sqrt{\pi}} \frac{n_e}{\sqrt{2k_s^2 k_B {}^{T_e}/_{m_e}}} \Gamma_\alpha(x) \quad \text{(Eq 2.38)}$$

$$S_i(\boldsymbol{k_s},\omega) = Z\left(\frac{\alpha^2}{1+\alpha^2}\right)^2 \frac{1}{\sqrt{\pi}} \frac{n_e}{\sqrt{2k_s^2 k_B {}^{T_i}/_{M}}} \Gamma_\beta(y) \quad \text{(Eq 2.39)}$$

where:

$$\Gamma_\alpha(x) = \frac{\exp(-x^2)}{(1+\alpha^2(1-f(x)))^2+\pi\alpha^4x^2\exp(-x^2)}, \beta = Z\frac{T_e}{T_i}\frac{\alpha^2}{1+\alpha^2}, x = \frac{\omega-\omega_0}{\sqrt{k_s^2 k_B T_e/m_e}} \text{ and } y = \frac{\omega-\omega_0}{\sqrt{k_s^2 k_B T_i/M}}$$

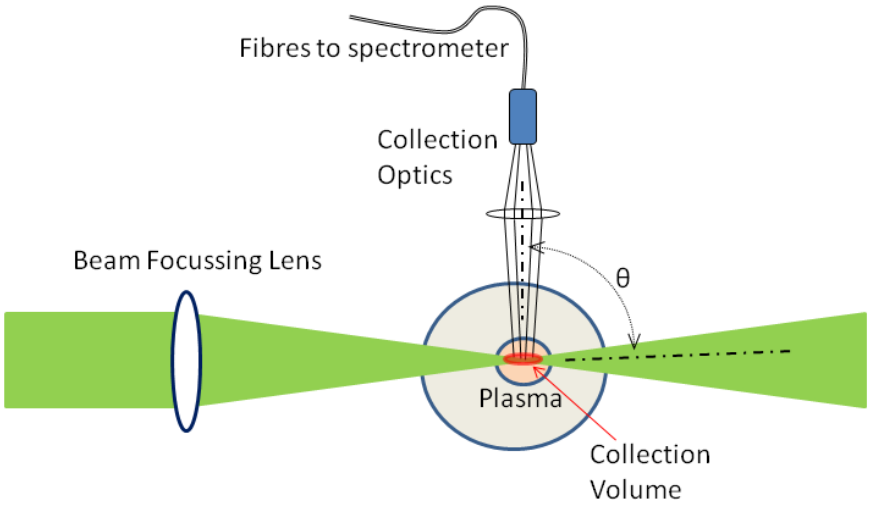

Figure 2.28: The main elements of a Thomson scattering experiment

Figure 2.28 shows the basic configuration used for Thomson scattering experiments, and figure 2.29 shows two predicted spectra, representing low and high α scenarios.

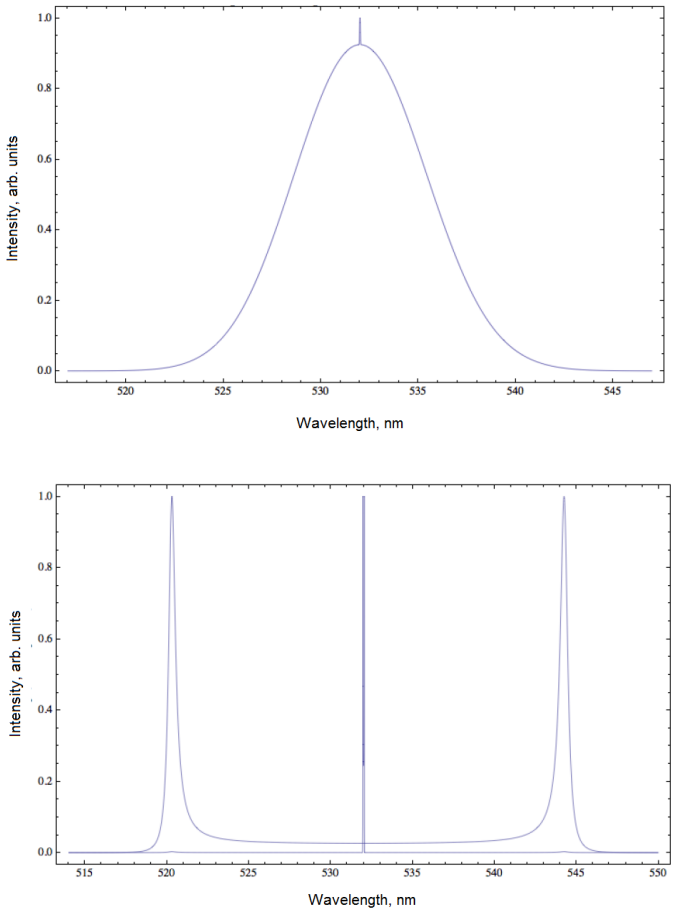

Figure 2.29: (reproduced from [2.29]) Showing the different between (top) low and (bottom) high α spectra, using theoretical spectra.

The direction of observation is set by consideration of several factors. Primarily, it will be governed by the availability of suitable ports on the plasma chamber. Small angles will lead to non-scattered light, direct from the laser source, entering the detector, possibly damaging it. For a given plasma, the range of acceptable angles can be discerned by a range of α that retains the characteristic of non-collective scattering. At small angles, α grows large, and so the so-called forward scattering regime is good for collective effects, and backscattering is better for free electron measurements. With careful design, it can be possible to devise an experiment that captures both ion and electron characteristics using a high α regime. Another approach to obtain information can be to implement a second set of collection optics at a different angle.

The design of the Thomson diagnostic on the MAGPIE chamber is previously documented, see [2.27, 2.29 and 2.33]. Important features of the design are measures to limit the incident beam from

entering the diagnostic equipment following reflection off equipment. Measures are implemented to cut down on the stray light, such as beam dumps to absorb the unaffected probe beam and prevent it re-entering the system, and baffles, structured surfaces inside the optics system to reduce the light entering the system from unwanted directions. Details are also given on the collection optics, namely bundles of optical fibres, which carry the scattered light to the Andor spectrometer, where a 2400 line/mm grating provides the resolution to analyse the scattered spectrum. In [2.29] a capillary discharge plasma gun with this system was studied, using 300 and 600 line/mm grating yielded measurements of electron density 7.5×10^{13} cm^{-3} at a temperature of 1.72 eV. Errors were estimated at ±0.35 eV for the 600 line/mm, using a 200 μm slit. Errors would be improved by a finer grating and a narrower slit. Errors in the measurement of electron density were felt to be less than the errors potentially caused by assumptions in the method of separating distributions from different effects, such as Rayleigh scattering from air, due to the chamber only being pumped to a low vacuum (10 mbar). The values measured are in the same range as are expected to be present in the plasma created by a plasma gun.

Some changes to the original system have been made since the system was first documented, the most significant being an improvement to the laser beam profile by passing it through a spatial filter which improved the beam profile by removing unwanted high frequency components. Due to the high energy in the laser pulse (2 Joules delivered in 3 ns, equivalent to a power of 200 MW), the beam is brought to a focus and passed through the aperture providing the filter in a vacuum.

The form of a spectrum can be predicted in software [2.31], which includes the convolution of the theory and experimental measurement factors, such as camera blur and focussing tolerances. For the range of plasma energies and densities expected in the plasma from a plasma gun gives a range of α values ranging from 0.25 for 1 eV / 10^{15} cm^{-3} to 0.81 for 10 eV / 10^{18} cm^{-3}. Simulations of the expected spectra are shown in figure 2.30.

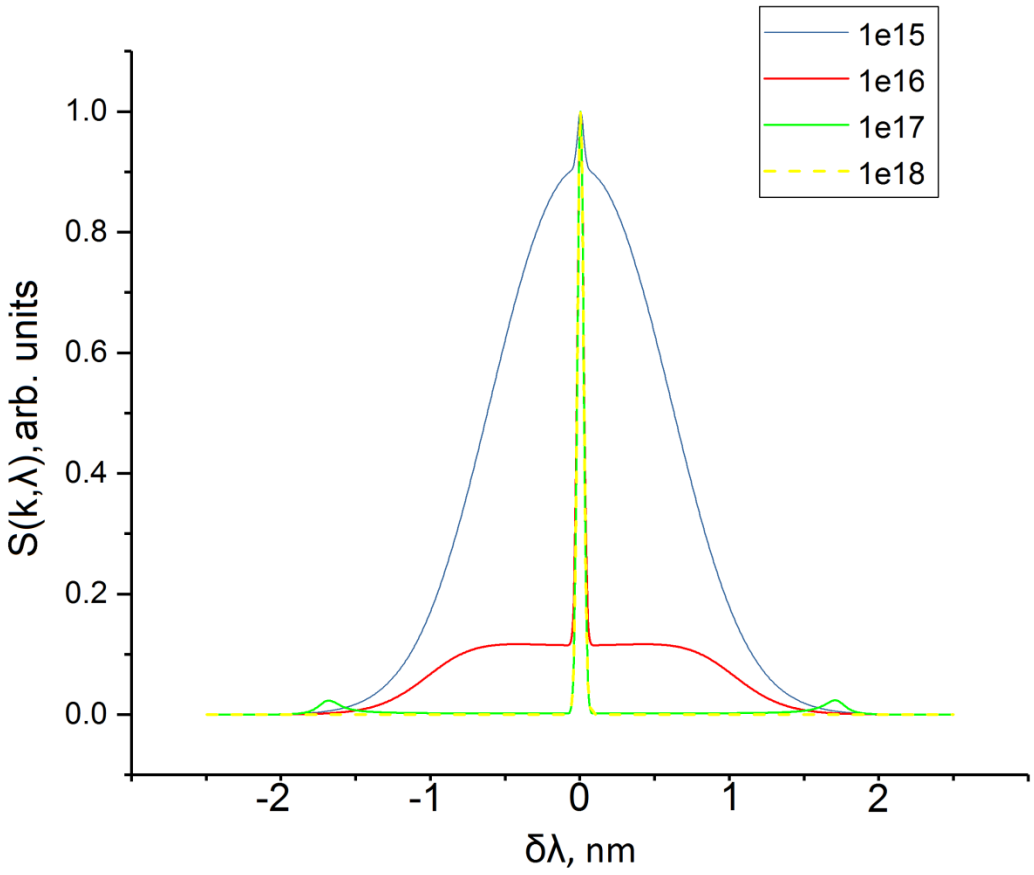

Figure 2.30: Simulated Thomson Scattering spectrum, including convolution of measurement broadening, for a range of densities ($1x10^{15}$ -$1x10^{18}$ /cm3), at a scattering angle of 90°, Ti=Te=1 eV.

The equipment is aligned by passing the Thomson diagnostics laser, on a low power setting, through the diagnostics chamber, and moving a needle within the chamber until it scatters the laser. The needle is used to provide a point in space off which the laser scatters to give accurate location information and match the physical location in the chamber with the optics. The needle location is then adjusted until the scattered light primarily enters the middle fibre in the bundle. The scattered light is focussed into the collection bundle by a telescope type system made of two lenses, see figure 2.31. Focus is checked by moving the collection bundle back and forth. At focus, the light will enter only the central fibre, and not its neighbours. Next, the needle is moved until the scattered light enters the first of the seven fibres in the collection optics bundle. The needle is then moved along the path of the laser until the last of the seven fibres is illuminated. The limits of these locations bound the collection volume, and the plasma gun is then located a distance above the volume directed downwards, such that the seven collection points form a line across the plasma, figure 2.32.

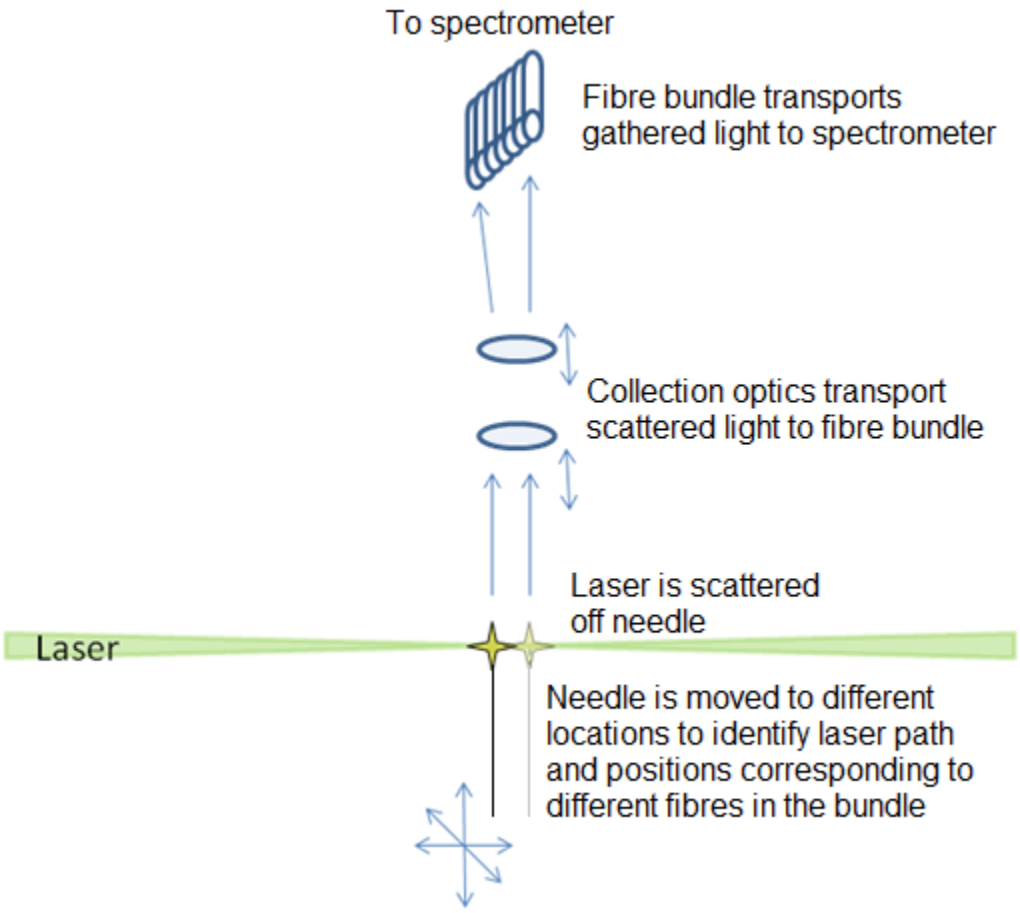

Figure 2.31: A needle mounted inside the vacuum chamber can be manipulated under vacuum to locate the correct locations along the beam corresponding to the different fibres in the bundle, as well as allowing for focus adjustment of the optics.

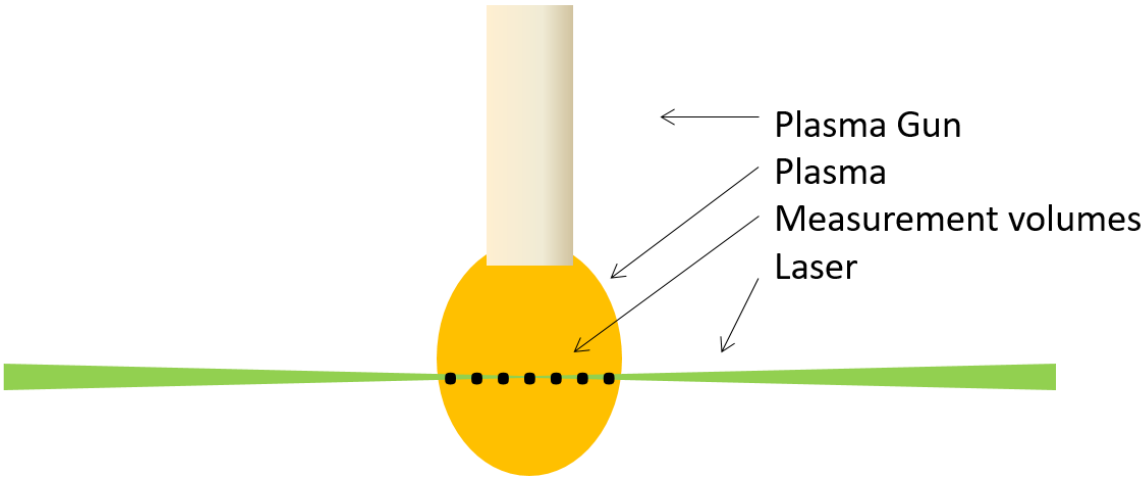

Figure 2.32: Sketch showing the orientation of the plasma gun and the Thomson scattering measurement volumes. Spatial interferometry was also taken in the same plane.

Chapter 3: Experimental results and discussion

As discussed in the introduction, the experimental research first concentrated on exploring the characteristics of the plasma from a single gun, and then that of an array of six guns as found in a PFRP.

3.1: Single Gun

In the initial experiments, a single plasma gun was used, firing into a vacuum chamber with viewing ports positioned such that the interferometry lasers can pass through the chamber at a short distance in front of the nozzle of the plasma gun. This configuration allowed a side-on view of the plasma with a degree of adjustability allowing the position of the chord to be varied.

One recurring challenge encountered in early experiments was that a gun would simply stop firing, causing a breakdown elsewhere in the driver circuitry. The failure generally occurred when the gun had been fired many times, and the chamber had been pumped for a long period (~5 hours). It is felt that the cause of the failure was that the surface of the nozzle was too clean, and so the initial breakdown couldn't happen, as there were no defects or impurities to concentrate the electric field. When the nozzles are initially machined, the edges of the conductors are quite sharp, and feature rough burrs. Over the course of a series of shots, these surfaces get eroded smooth, and so the dielectric becomes polished giving fewer features from which breakdown may initiate. [3.1] notes a similar effect when they were investigating plasma guns. After many (~100-200) shots, the edges of the conductors become eroded and the performance of the plasma gun becomes degraded. The nozzle must then be refurbished by simply re-machining the nozzle.

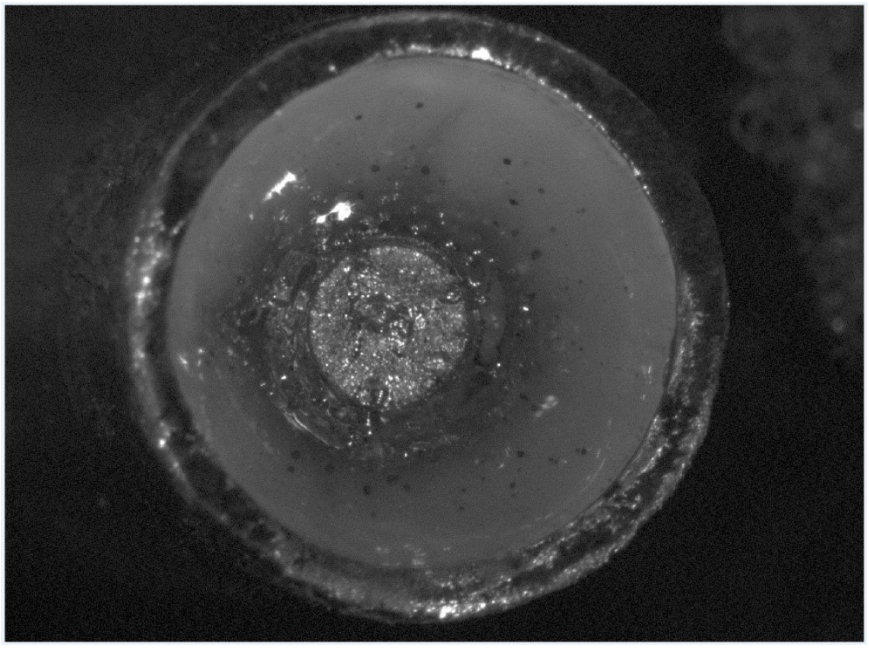

Figure 3.1: Erosion of the nozzle can be clearly noted after a low number of shots (~25). The central conductor becomes more eroded as the shot number increases.

Using the current trace, it is possible to estimate the resistance of the gun's discharge if the assumption of constant resistance is made. By simulating the plasma gun driver as a lumped LCR circuit and iterating the values until the simulated current trace matches the measured one. Using this technique, and setting C= 0.7μF, the values obtained were L= 0.451 μH, and R= 0.13 Ω. Appendix 1 provides a brief summary of this.

The quoted value of R represents a maximum value, as some energy will be lost in the circuit, for example in the heating of the cables, or being dumped to earth through the inductors, the switch will also dissipate energy. Energy will be dissipated through the ionisation of the ablated species. As current flows through the plasma between the electrodes, it may also be the case that the current path increases, staying frozen into the plasma. This will lead to an increase in the inductance of the current path, reducing the current. A more accurate estimate of the resistance of the plasma could be obtained by measuring the voltage across the gun during a discharge. It was not possible to do this in this experiment however.

3.1.1: Self-emission photography of the face of the plasma gun

End-on shots, using a turning mirror to enable a useful view, were performed as a means of establishing symmetry of the surface breakdown and the subsequent plasma emission from the plasma gun. If the fill was not symmetric, it would affect later analysis, such as line integrated densities and Abel inversions. Self-emission of the discharge provided the illumination, but no spectroscopy was used. Images were successfully obtained, and as can be seen in figure 3.2, showing a close-up, end-on image of the initial stages of the plasma creation, the plasma is not initially generated in a radially continuous discharge, but rather in distinct locations, distributed around the nozzle of the plasma gun.

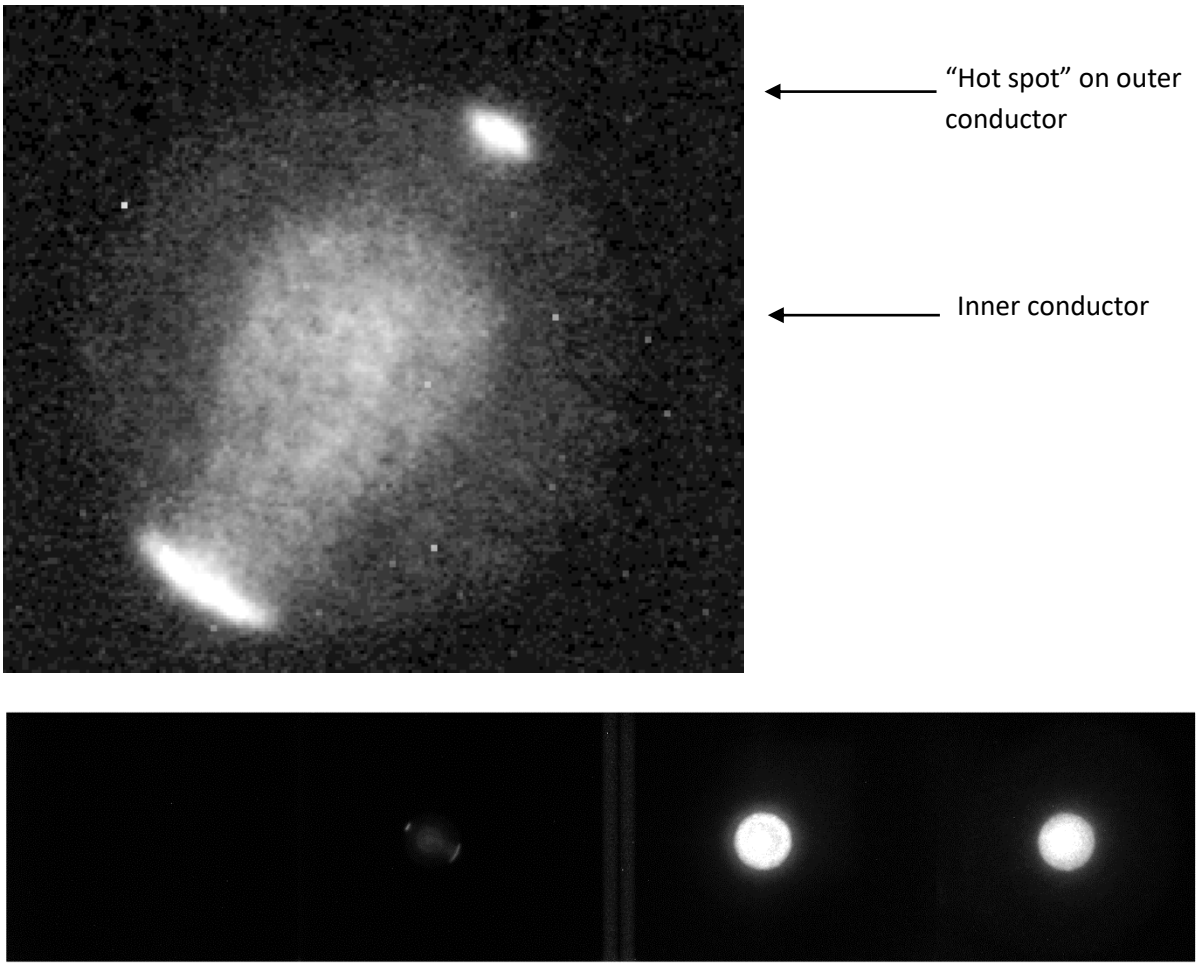

Figure 3.2: An early-time breakdown end-on image, top, showing how the breakdown occurs at specific points around the outer conductor. The discharges later progress to encompass the whole nozzle over approximately 300 ns, as shown in the sequence, bottom. (exposure = 50 ns, 200 ns between the start of each frame). The discharge lasts for the duration of the current pulse and dies away as the current decreases.

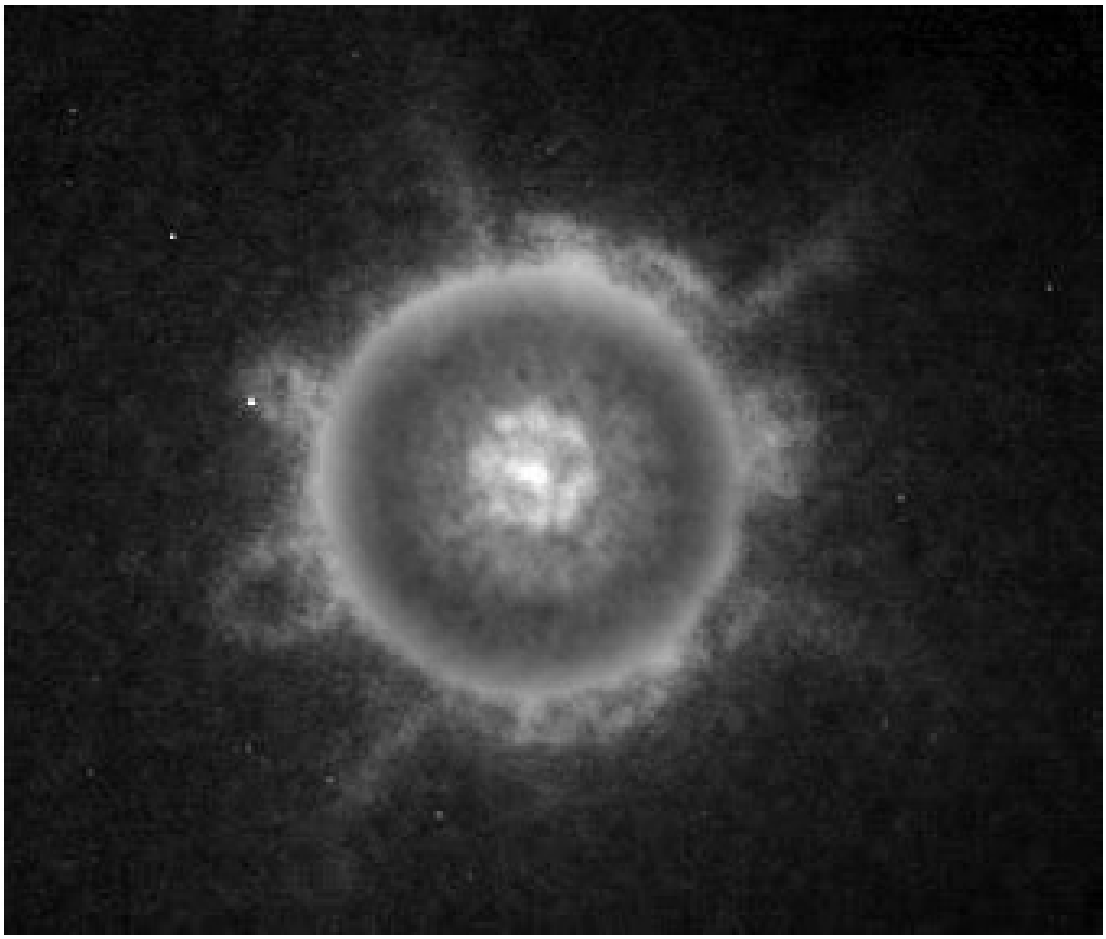

Figure 3.3: End-on captures of the visible emission from the plasma occasionally show what appear to be loops. (Image has been modified to enhance clarity of outer region.)

Some shots show what appear to be loops, similar to coronal mass ejections on the surface of the sun, see figure 3.3. It could have a simple explanation, namely that the loops are not loops, but the cooling edges of a localised discharge, visible as it cools and emits in the visible part of the spectrum. This could arise from a localised discharge giving a small plasma region, rather than a plasma covering the entire nozzle. A more exotic explanation could be that it suggests quite complex behaviour is occurring in the nozzle during a discharge resulting in magnetic field lines being trapped in loops. Further work would be required to confirm that this is what is happening.

PrismSpect [3.2] simulations of carbon plasma in the density range of 10^{15} - 10^{18} /cm^3 and temperature range of 1-10 eV suggest that visible emission in the 6-10 eV range would be from C III and C IV, and only at the denser end of the range.

[3.3] suggests that these levels of ionisation would only be seen at voltages above those used in these experiments, a statement supported by [3.4]. This information can be used to add a constraint to the plasma temperature range that can be expected. At the lower end of the density range, 10^{15} /cm^3, PrismSpect shows very little emission across the 1-10 eV range, which, in conjunction with the first statement, informs us that the self-emission regions are the higher density ones at energies of 1-6 eV.

3.1.2: Single Gun Spatial Interferometry

An example of the results from the 12 frame spatial interferometer developed for this study is shown in figure 3.4, demonstrating a movement of the fringes close to the end of the nozzle. The plasma gun shown in the images was driven at the ~25 kA level by one of the doghouse capacitor banks loaned to the project by NRL, as described in the previous chapter. This unit is very similar to those typically used in the PFRP on Gamble II.

There is a trade-off between spatial resolution of fringe movement and overall system sensitivity. If the fringes are close together, it becomes easier to see if any move, but as the sensitivity of the system is governed by the fringe density, this can mean that lower density changes simply aren't recorded or are very easy to miss. Wider spacing allows for the fringe density be met over a wider area.

The interferometry systems did not exhibit perfectly straight fringes. It is generally preferable to have straight fringes, as this assists analysis. Fringes are essentially circular, but in a well-aligned system, they appear straight because their radius is sufficiently large as they are far from the centre. Couple this with a small field of view and the curvature of the fringes is not detectable. In the large field of view system, the curvature becomes more evident, even if the system is well aligned.

It is possible to take line outs across the plasma density map in order to ascertain the divergence of the plasma.

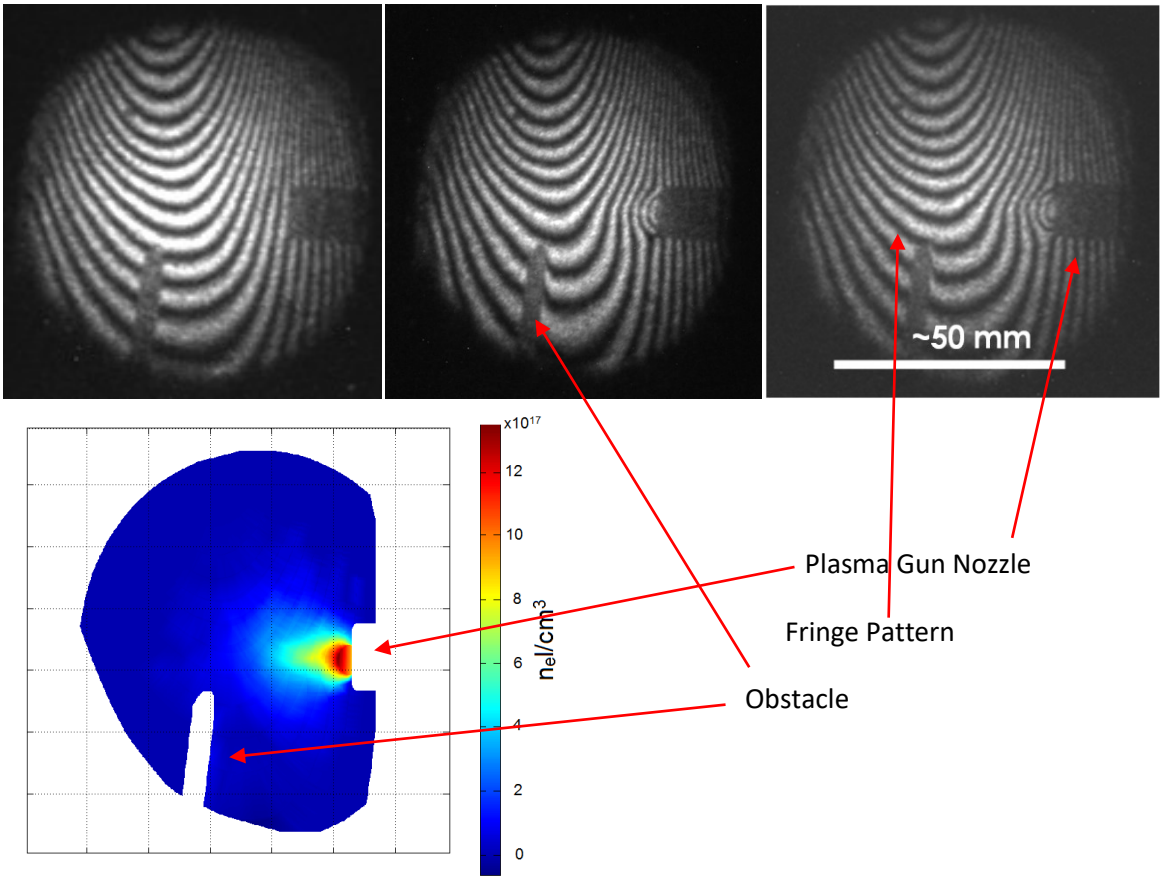

Figure 3.4: An example of frames from a typical sequence from the high-speed camera, frames 1, 5 and 10. (Exposure: 10 ns, final frame taken 5.465 µs from current start, slightly after current peak of 25 kA). The full sequence of captured frames for this shot can be found in appendix 2.

A typical plot of $n_e l$ obtained using the analysis described is shown in figure 3.5 from a fringe pattern obtained at 2.8 µs after the current starts, as the circuit rang and the current reached a second peak. The plasma can be seen developing from the right of the image (please note: this is from a different shot to the image above, in figure 3.4). The density at specific distances from the nozzle can be determined using linear extractions from the 2D plot. These are very useful at showing how quickly the density drops with distance from the nozzle and the divergence of the plasma.

As there is not a firm edge to the plasma, a density contour needs to be chosen in order to consistently and quantitatively study it. Once chosen, this contour can be followed through the sequence of images to understand how the plasma distribution changes over the duration of a discharge. Plasma expansion velocities can be estimated by measuring the progression of the density contour over a set time.

Although the peak density, found at the nozzle, is 1.5×10^{18} /cm^3, the density decreases rapidly as the distance from the nozzle increases, by roughly three orders of magnitude in just 50 mm. The plasma density quickly drops below the threshold of reliable measurements. In order to understand how the plasma behaves once it reaches the anode, an obstacle was inserted in the path of the plasma expansion. Initially, this was a small copper paddle, later changed to a length of thick copper wire to more closely reflect the geometry of the anode rod. When the plasma front collides with the obstacle, the density increases and is once more detectable. This makes it possible to estimate the speed of the plasma expansion using a second method, over a longer distance. At the 532 nm wavelength of laser light used, the fringe constant is 6.65×10^{16} /cm^3, at densities below this, the fringes move by less than one whole fringe, and so errors can creep in during the manual process of tracing the fringes. Estimated errors are as much as 1/8 of a fringe (8.3×10^{15} cm^{-2}), and so the divergence measurements in particular need to be limited to a region where the measurements are reliable.

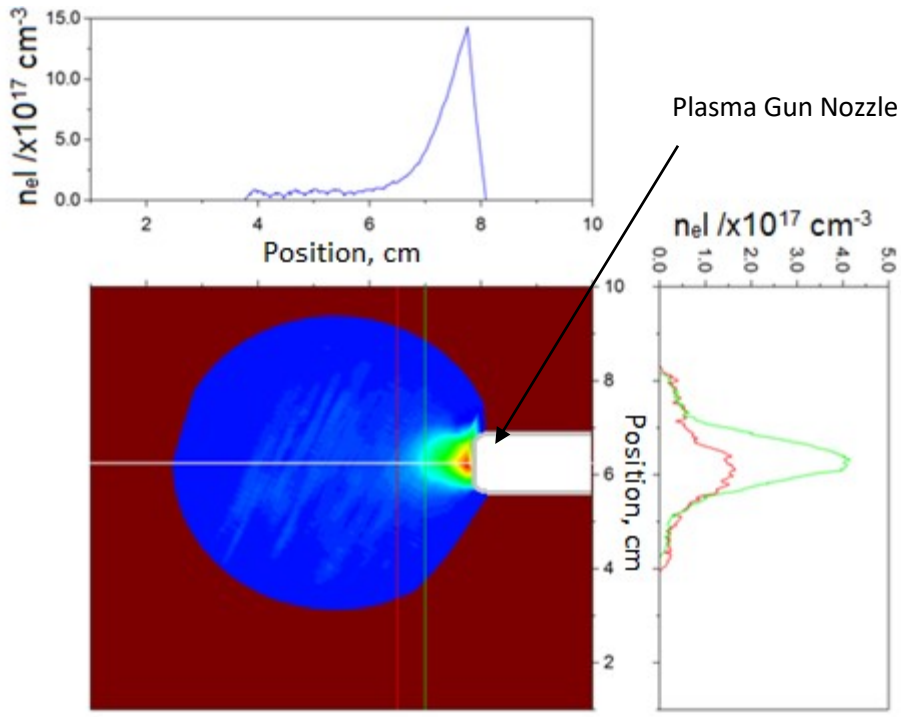

Figure 3.5: A frame from a single plasma gun density-mapped in Magic and then imported into Origin for analysis. (A sketch of the plasma gun has been added to show its location) The use of multiple frames from a single shot enables the evolution of the plasma to be understood by analysing the plasma at each point in time and quantifying the changes between frames.

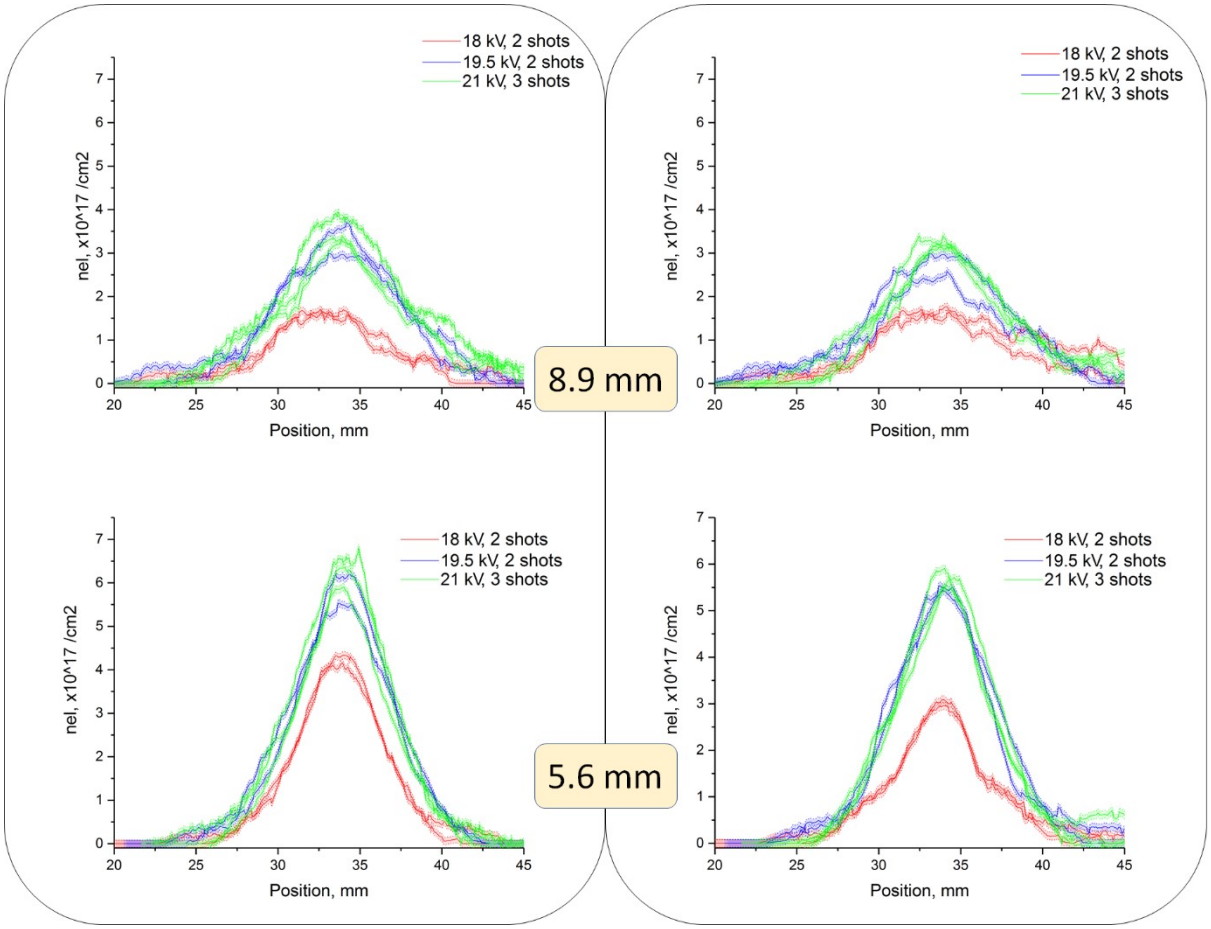

Figure 3.6: lineouts from 7 different shots, two lines taken at different distances from the nozzle, at frames 8 (left, top and bottom) and 12 (right, top and bottom). The time to the frame used in each shot varied a little, due to the varying charging voltages. Frame 8 timings are: 18kV: 2.7 µs, 19.5 kV: 3 µs, 21 kV: 3.2 µs after current start, frame 12 is 1.6 µs later (T_{abs}=4.5 and 6.1 µs), half a time period of the decaying ringing frequency.

The lineouts in figure 3.6 show how the plasma evolves over time at different distances from the nozzle. The lines are taken across the plasma at distances of 5.9 and 8.6 mm from the end of the nozzle. The "full width half maximum" measurements at these distances are the widths of the profiles, taken at a value that is half of the peak value. This is not necessarily the only measure of the profiles that could be used, for example looking at the 10-90% values could also be useful, but the noise floor on the profiles is not very high, and so the FWHM is a reasonable metric to use. The lineouts for the 18 kV shots were generated at an earlier time in the pulse evolution, so the absolute densities cannot be compared directly, but the behaviour can still be discerned.

All of the profiles for the higher voltage (21 kV) shots are tightly grouped and show FWHMs of 5.9 mm and 8.6 mm for the lines close to, and further from, the nozzle. These values are unchanged

between the two times. Using these, along with the timings, and the peak $n_e l$ of 3.3, 6.4, 3.1 and 5.5×10^{17} /cm^2 for each of the four lines (two positions at two times), it is possible to compare Gorgon simulations with these experiments (see later chapters). It is interesting to note how the peak densities are slightly lower in the later frame, due to the oscillatory nature of the drive current. As the plasma recombines rapidly, the density varies with the current as the circuit rings. The lower voltage shots form a second distinct group. It is interesting to note that the later density of the 18 kV shots decreases more noticeably than the 21 kV shots, despite the current pulses decaying by the same extent. This suggests recombination is occurring more often, as the plasma temperature is lower and the plasma species are moving more slowly. The electron density is less variable in the higher voltage shots, evidenced by the electron density remaining similar at both times.

Studying the current traces shows an interesting effect. For the lower voltage shots, 18 kV, the jitter of the system is quite severe, at 1.2 μs. This made it very difficult to synchronise the high-speed camera frames reliably. The large jitter is due to the spark gap at the heart of the driver circuit relying on high voltage breakdown across the gap. At lower voltages, this breakdown mechanism is much less reliable than at higher voltages causing the switch to operate more slowly at the lower voltages. The current start times vary by 650 ns if all the shots are studied, falling to 330 ns if the 18 kV shots are removed. The variation of the timing leads to the frame numbers for each shot not necessarily aligning with each other. In the shot sequence above, the current for the 18 kV shot started roughly 0.5 μs later.

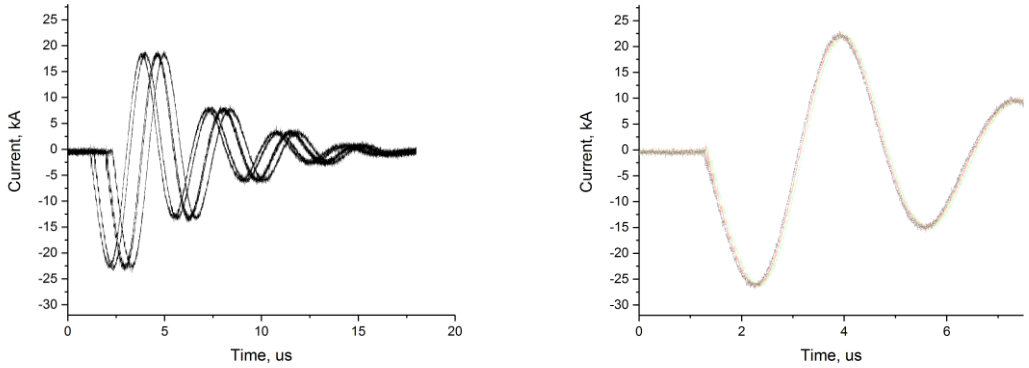

Figure 3.7: Lower voltage shots (18 kV, left, showing data from 5 shots) show large jitter, whereas the jitter is significantly reduced at higher voltages (19.5 - 21 kV, right, showing data from 4 shots) See Appendix 2 for a plot of density against current.

The interferometer was used to study the velocities and gave estimates in the range of 8.5×10^3 for 18 kV to 14.5×10^3 m/s for 21 kV. Velocities were estimated by analysing the expansion of the plasma over multiple frames.

The results are in the range published in the literature [3.3, 3.4] but the measurement suffers errors due to the poor illumination of the plasma, and the narrow field of view restricting the timescale over which velocity can be measured, reducing the certainty of the value calculated for the plasma density. There is also an error associated with the uncertainty of the time of flight, as the interferograms are taken with 400 ns between them.

As the plasma is projected from the gun and continues to expand, there are questions on whether or not it remains collisional, that is, is the mean free path of collisions less than the characteristic length of the plasma. Using the definitions outlined in [3.5], the mean free path can be estimated for each time of interaction (i-i, e-e, e-i, i-e).

The subscripts *s* and *s'* describe the effects on species *s* from interactions with *s'*:

$$\lambda_{mfp,ss'} \equiv v_{ts}\tau_{ss'} \quad \text{(Eq. 3.1)}$$

Generally, $\tau_{ss'} \equiv \frac{3\sqrt{\pi}}{8}\frac{m_{s'}}{m_s+m_{s'}}\frac{m_s^2(v_{ts}^2+v_{ts'}^2)^{3/2}}{\gamma_{ss'}n_{s'}}$, but ion-ion and electron-ion collisions are excepted:

$\tau_{ii} = \frac{3\sqrt{\pi}}{8}\frac{m_i^2 v_{ti}^3}{\gamma_{ii} n_i}$ and $\tau_{ei} = \frac{3\sqrt{\pi}}{8}\frac{m_e^2 v_{te}^3}{\gamma_{ei} n_i}$, respectively, where $\gamma_{ss'} = \frac{e_s^2 e_{s'}^2 \log \Lambda_c}{8\pi\varepsilon_0^2}$ (Eqns. 3.2)

Log Λ_c is known as the Coulomb logarithm, which provides a measure of the closest approach in a Coulomb collision, m is the atomic mass of the particle, in the plasma, m_i is taken as 12 amu, for carbon. e_s is the charge of the particle, and v_{ts} is the thermal speed of the particle.

Table 3.1 gives mean free paths (MFP) for densities between 10^{15} and 10^{18} /cm^3, with the temperature varying between 1-10 eV, as measured in this study, illustrates that the mean free path for the electron-ion interactions is very small and likely to dominate, once the density reaches 10^{17} /cm^3, with a temperature in the lower end of the range, 1 eV or so.

MFP	10^{15} /cm^3, 1 eV	10^{17} /cm^3, 1 eV	10^{18} /cm^3, 1 eV	10^{18} /cm^3, 5 eV	10^{19} /cm^3, 1 eV
ee	98.8	1.58	0.23	2.97	$3.92\text{x}10^{-2}$
ii	$2.57\text{x}10^{6}$	$4.11\text{x}10^{4}$	$5.86\text{x}10^{3}$	$7.93\text{x}10^{4}$	$1.03\text{x}10^{3}$
ei	0.50	$7.96\text{x}10^{-3}$	$1.14\text{x}10^{-3}$	$1.51\text{x}10^{-2}$	$1.94\text{x}10^{-4}$
ie	$3.23\text{x}10^{4}$	$5.17\text{x}10^{2}$	73.7	$9.88\text{x}10^{2}$	12.8

Table 3.1: Various mean free paths (in metres) for a range of plasma densities and temperatures. Collisional regimes are highlighted in grey. These have been calculated with the ion and electron velocities set to be equal, to approximate the values measured by using the interferometry, rather than using thermal velocities. Velocities are set to be equal to maintain quasineutrality.

The changes made to the interferometry system, with massively improved beam profile and brightness, and a wider beam, lead to much improved results. The better illumination provided greater clarity of fringes across the image, and the wider field of view allows for longer distances for the velocity to be measured over. These improvements led to estimates of $5.5\text{x}10^3$ m/s for plasma created by firing at 18 and 19.5 kV, and 9-$12\text{x}10^3$ m/s at 21 kV. It is not possible with this system to measure the ion velocities, only the combined electron and neutral density which causes a change to the refractive index.

3.1.3 Single Gun CW Interferometry

As the exposures on the 12 frame camera are discrete in time, a single point temporal interferometer, employing two CW wavelengths, was fielded. This enabled estimates of ionisation

and how this varies with time. This work was the logical extension to the single wavelength CW triature interferometer presented in [3.6].

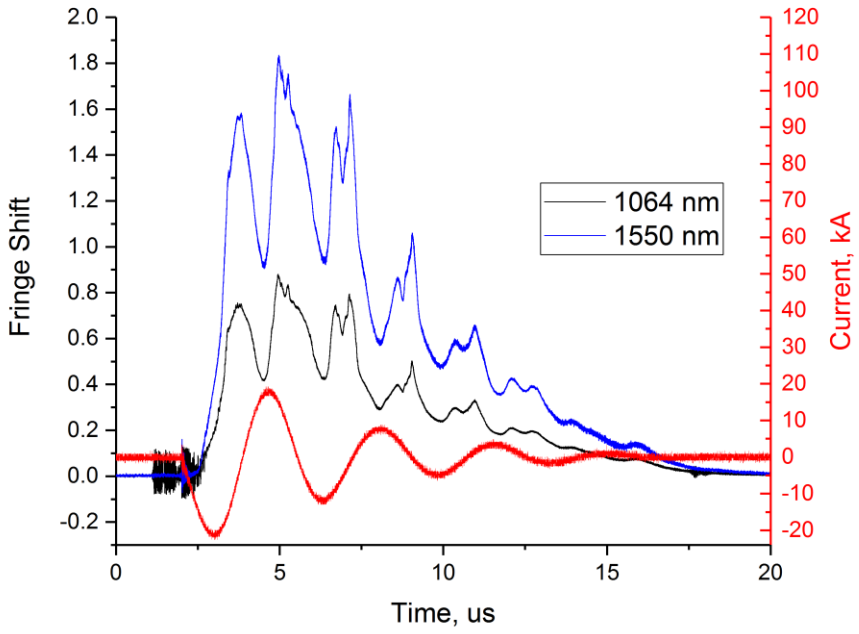

Figure 3.8: Showing fringe shift traces for 1550 nm and 1064 nm for one shot, interferometry chord 15 mm in front of the nozzle, on axis.

Typical plots of fringe shift vs time for two wavelengths is shown in figure 3.8, along with current. As can be clearly seen, there are coincident fringe shifts for both wavelengths occurring over 20 µs. They are delayed relative to the start of the current pulse by a combination of time of flight and time required for the current pulse to reach a value where plasma is created at a rate fast enough to give rise to a significant enough density to be measurable.

Comparing the traces for 1550 and 1064 nm shows that there is a difference in the fringe shifts of the two wavelengths. Adding a second CW wavelength allowed for the testing of the assumption that the species present in the plasma are 100% ionized.

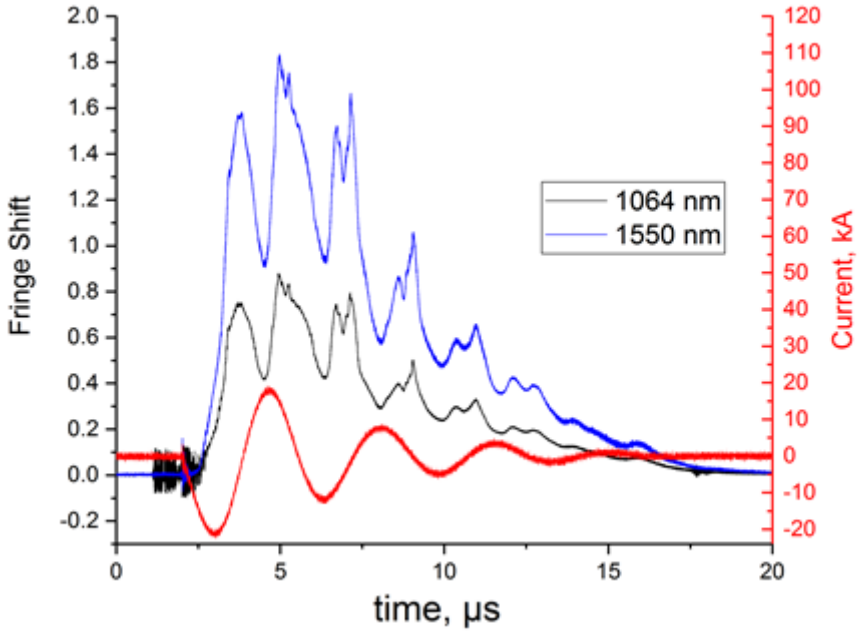

Figure 3.9: $n_e l$ and $n_0 l$ from a 21 kV shot, $n_e l$ shows as being ~$n_0 l$/5. The values near t=0 us should be disregarded, as there is significant noise in the signal from the spark gap firing.

Figure 3.9 shows $n_0 l$ (calculated using the Drude model and Gladstone-Dale constant method) varying over time, and not directly following the electron population density. A curiosity is also evident, that undermines the reasonableness of the data, that the values are negative at some points in the trace, which clearly is erroneous. This result is echoed in some independent analysis carried out on data acquired using the dual wavelength interferometer on the MAGPIE diagnostic chamber, as shown in figure 3.10. Smoothing the phase shift data does not improve the situation, but normalising it does, which suggests that the method will work for certain ranges in electron density and ionisation state. Normalising the data is not an acceptable step to add as it fundamentally changes the nature of the signals acquired. [3.7] presents results that contain a brief negative neutral density which is ascribed to anomalous dispersion, refractive bending or detector response differences. Absorption lines could also be a cause, which would lead to a wavelength dependence for the neutral component of the refractive index.

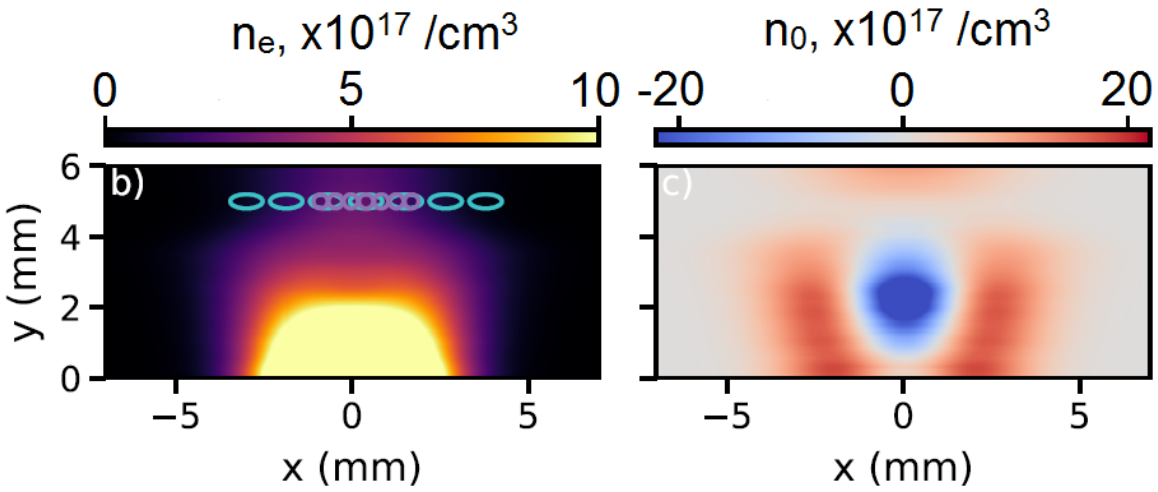

Figure 3.10: 2D plot showing the results of 2 wavelength analysis using the 532 and 355 nm beams in MAGPIE. The left image also features the locations of the Thomson scattering collection volumes. Figure 2.32 shows orientation details. [3.8]

The simultaneous equations used to calculate the electron and neutral densities can be found in two forms, as discussed in the previous chapter, the method using the Drude model and the Gladstone-Dale constant, and the method using the electron and neutral polarisabilities [3.7, 3.9, 3.10]. The electron and neutral polarisabilities are given by:

$$\alpha_e \approx -\frac{r_e \lambda^2}{2\pi} \quad \text{(Eq. 3.3)}$$

and $$\alpha_0(\lambda) \approx \frac{r_e}{4\pi} \sum_m \frac{f_{m_0} \lambda^2}{1-(\lambda_{m_0}/\lambda)^2}, \quad \text{(Eq. 3.4)}$$

The electron polarisability is very dependent on wavelength, but that of the neutrals is considered largely independent throughout the visible (and near visible) range. The neutral polarisability is obtained by summing over the range of resonant transitions between the level m and the fundamental state, with oscillator strength f_{m0}. Using the NIST database [3.11], [3.10] gives a value of 6.08x10^{-24} cm^3 for α_0. This calculation is quite complex, and α_0 can vary between materials, even those of a similar z, so the value presented in [3.10] will be used in this instance, knowing that more refined calculations that reflect the actual species present in the plasma will be needed for a more accurate value.

The other set of equations use the Gladstone-Dale constant, β. [3.8] shows how the Gladstone-Dale relation is used to calculate the polarisability of the neutrals, and is usually written as:

$$\frac{r_e}{2\pi} n_n \sum_k f_k \frac{\lambda^2 {\lambda_{0,k}}^2}{\lambda^2 - {\lambda_{0,k}}^2} = \frac{\beta}{n_0} n_n \qquad \text{(Eq. 3.5)}$$

The Gladstone-Dale constant has a value that is set for a given gas at a given density, and is used to calculate the neutral density in the following alternative pair of equations:

$$\int_{s_1}^{s_2} n_e(s) ds = \frac{\lambda_1 \Delta\varphi_1 - \lambda_2 \Delta\varphi_2}{r_e({\lambda_1}^2 - {\lambda_1}^2)} \quad \text{(Eq. 3.6)}$$

and $$\int_{s_1}^{s_2} (n_n(s) - n_0) ds = \frac{n_0}{2\pi\beta} \frac{\lambda_2 \Delta\varphi_1 - \lambda_1 \Delta\varphi_2}{{\lambda_2}/{\lambda_1} - {\lambda_1}/{\lambda_2}} \quad \text{(Eq. 3.7)}$$

Analysis using the Drude model / Gladstone-Dale constant approach, eqs. 3.6 and 3.7, has thus far yielded neutral densities that do not presently seem reasonable as they take negative values at various times. Use of the polarisabilities method, eqs. 2.31 and 2.32, gives results that seem more feasible, as shown in figure 3.11. The neutral density varies as the current pulses develop, tracking the increasing current.

Plotting $n_0 l / n_e l$ is not as straightforward as one would imagine, as the ratio very quickly becomes nonsensical when both values are close to zero, signal noise causes the ratio to swing wildly. Significant smoothing is required to draw out any sort of signal. If the regions either side of the main pulse region (0-~20 μs) are ignored, a time-varying ratio can be obtained, though using the information from it is not useful due to the fact that it also takes on negative values. The pair of equations from [3.10], once rearranged, yields a single multiplier to translate between n_e and n_0, with n_e being roughly 0.5% of n_0.

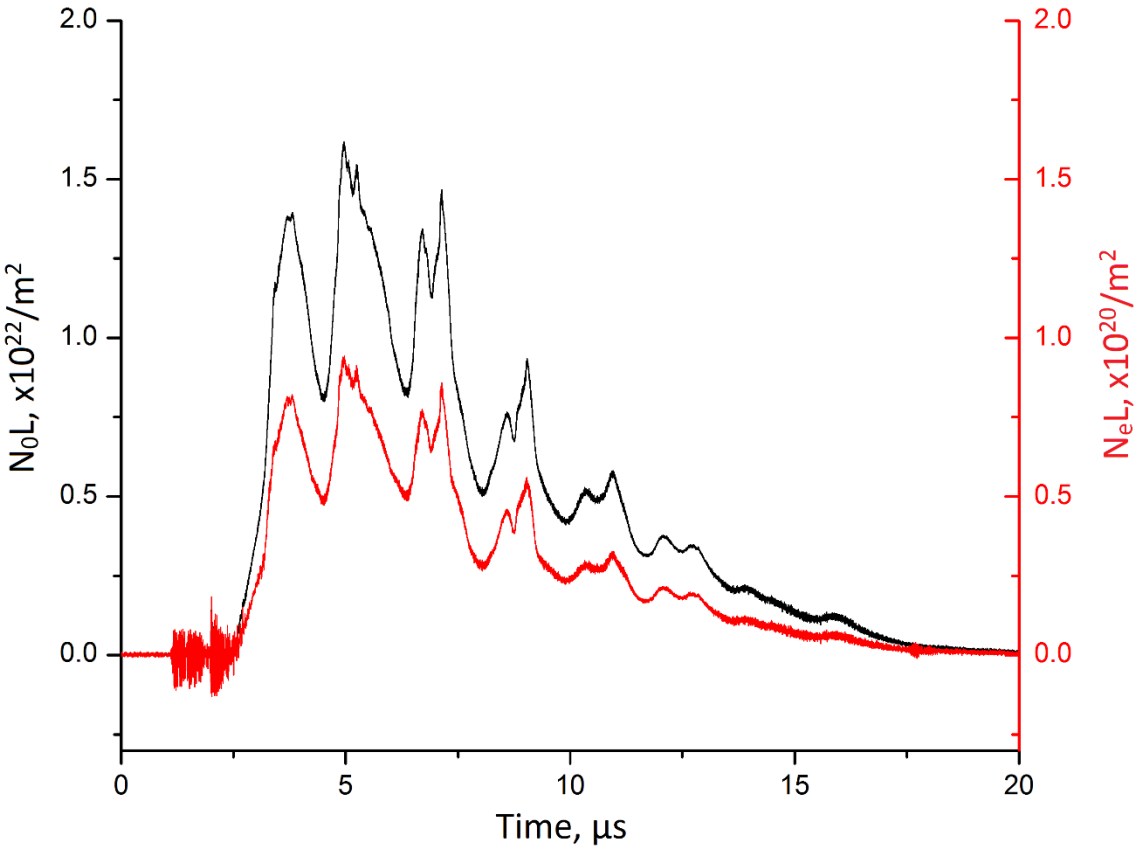

Figure 3.11: Using the simultaneous equations introduced in [3.10] yields a different relationship between the neutral and electron densities.

If local thermal equilibrium is assumed, and a further assumption about the state of ionisation can be made, the Saha equation [3.12] can be used to make an estimate of the ionisation fraction:

$$\frac{n_{j+1}n_e}{n_j} = \frac{2U_{j+1}}{U_j}\left(\frac{2\pi m_e k_B T}{h^2}\right)^{\frac{3}{2}} e^{-e\varepsilon_{iz}/k_B T} \quad \text{(Eq. 3.8)}$$

ε_{iz} is the energy required to ionize to the j^{th} state, n_j is the number of ions in the j^{th} state, the U-based terms relate to the degeneracy of the ion species. Solving the equation using software [3.13] suggests that for the range of plasma densities and temperatures expected in the experiment, the degree of ionisation would be in the range of 50-95%, that is, the ratio of n_e to n_0 is 5-50%. For the "feasible" results, those which do not take on negative values, the ratio is 0.5%, whereas for the times when the other method's results are positive, the ratio is roughly 2-5%. The “feasible” results are physically reasonable but disagree slightly with the Saha prediction.

The single wavelength CW measurements of n_e compare well with the literature, such as [3.1] and [3.2]. Current modulation is obvious in the density traces over multi microsecond timescales. [3.9] shows three distinct density peaks arising from the different times of flight for the different plasma species, whereas the recent measurements show, at most, two main peaks on each pulse. The difference could be attributed to variations in experimental technique, composition of the insulator or the current pulse from the plasma gun driver. One major difference is the distance between the nozzle and the interferometry chord, [3.9] measures at 50 mm, whereas these measurements were made at 15 mm. Increasing the distance will allow for differences in times-of-flight to increase.

Related to this might also be distinct differences that were noted in plasma density found from guns manufactured from different cable stock, though still meeting RG401 specifications. Peak densities were noted to differ by a factor of three, meaning comparative measurements had to be made using cables from the same batch. Montgomery Smith, Keefer and Wright also noticed similar results [3.1]. The two-wavelength measurements of n_e agree within a factor of two but vary in estimates of n_0.

3.1.4: Single Gun Spectroscopy

The Andor spectrometer system is capable of measuring wavelengths in the range of 300-1100 nm. A series of shots was undertaken on the MAGPIE diagnostics suite to gain an understanding of the species present in the plasma, with measurements spanning 25 mm in front of the nozzle. The time after the trigger that the spectra are taken can be varied to understand how the plasma composition varies with time, as the time of operation of the CCD using to capture the image can be controlled.

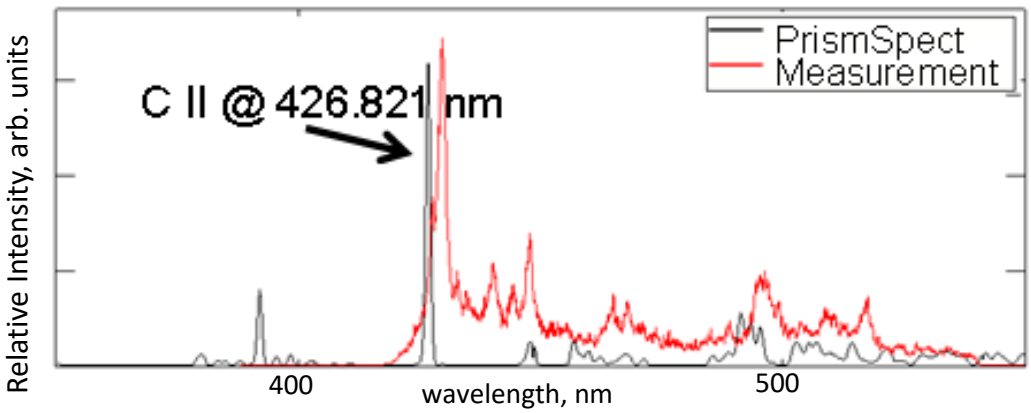

Figure 3.12: Comparing a section of spectroscopy data with PrismSpect predictions. In this example, the trace was acquired at 1480 (± 50) ns after gun current starts.

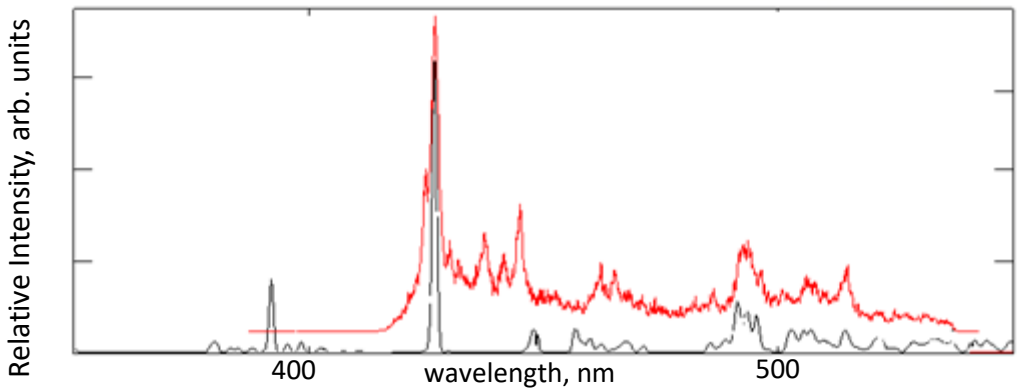

Figure 3.13: Alignment of peak becomes more obvious when the 3.1 nm offset is removed, measurement trace is positioned higher than PrismSpect trace for clarity.

The obtained results contain a constant 3.1 nm offset due to calibration errors during set-up, figure 3.13 shows how the peaks can be matched between the spectroscopy data and the PrismSpect data, the example shown being for the 426.821 nm peak for CII. The offset renders analysis within the Andor Solis software meaningless, as the peaks get identified as obviously incorrect elements. It is interesting to note the discrepancies in the small peaks around 450 nm. These are not due to misalignment, as the more prominent peaks either side are correct. This difference suggests that the measured spectra could potentially contain different proportions of elements, and even extra ones that were not modelled in the PrismSpect simulations.

By running PrismSpect simulations with different compositions and comparing the results, it is possible to discern that the plasma contains C II, C III, F II, F III, Cu II and Cu III. This is not a surprising result, as the PTFE in the plasma gun is comprised of carbon and fluorine, and the electrodes are

copper. In order to estimate the density and temperature of the plasma under study, the density and temperature modelled in the simulations were varied. The proportions used initially were O 5%, H 5%, F 40%, C 20%, Cu 30%. The relative densities of the F and C were chosen to approximately reflect the proportions of each within PTFE (1:2 ratio of C:F), assuming that each is similarly ablated and ionised. The oxygen and hydrogen were included to account for any water vapour left in the chamber after pump down. The copper was included to allow for the erosion of the electrodes of the plasma gun. Existing literature puts the electron temperature in the region of 1-15 eV [3.3] so this is the range that was initially modelled.

Three spectrographs were studied, taken at varying times into the plasma evolution and PrismSpect simulations were performed, aiming to match the measured emission. These simulation results suggest that the plasmas present at each of these times can be characterised as: 1480 (± 50) ns after drive current starts: ~2 eV, 10^{16} /cm^3, 2060 (± 50) ns: ~2 eV, 10^{18} /cm^3 and 3220 (± 50) ns ~2.8 eV, 10^{18} /cm^3. The graph on the right in figure 3.7 shows an indicative current pulse. These parameter values were chosen by performing a two-variable parameter scan, simulating the density ranges and the energy ranges gained from experiment and from the literature, and matching the simulated spectra with those acquired by experiment. Figures 3.14 to 3.19 show how peaks change as the nature of the plasma varies, which provides a rough estimate of the temperature and density of the plasma. It is sensible that the density of the plasma would increase as the pulse progresses.

The measured spectrographs are more complicated than the simulated ones as the MAGPIE chamber contains traces of previous experiments, and even just atmospheric air will contain more elements than the PrismSpect simulation contains, as that is a "pure" plasma containing only species known to be present. At the pressure that the gun is fired at, 10^{-4} mbar, the number density of background neutrals (atmospheric air now under vacuum) will be roughly 10^{12} /cm^3, which is at least three orders of magnitude less dense than the plasma is expected to be (10^{18} /cm^3 at the nozzle, 10^{15}

at 50 mm from the nozzle), so any spectroscopic signal from that background will be overwhelmed by that of the plasma, although sometimes contaminants can cause a significant signal.

The spectral resolution of the equipment can be mimicked in the simulation, so that sharp peaks are suitably broadened to aid comparison. The suggested setting for the MAGPIE system is $\lambda/\delta\lambda = 400$.

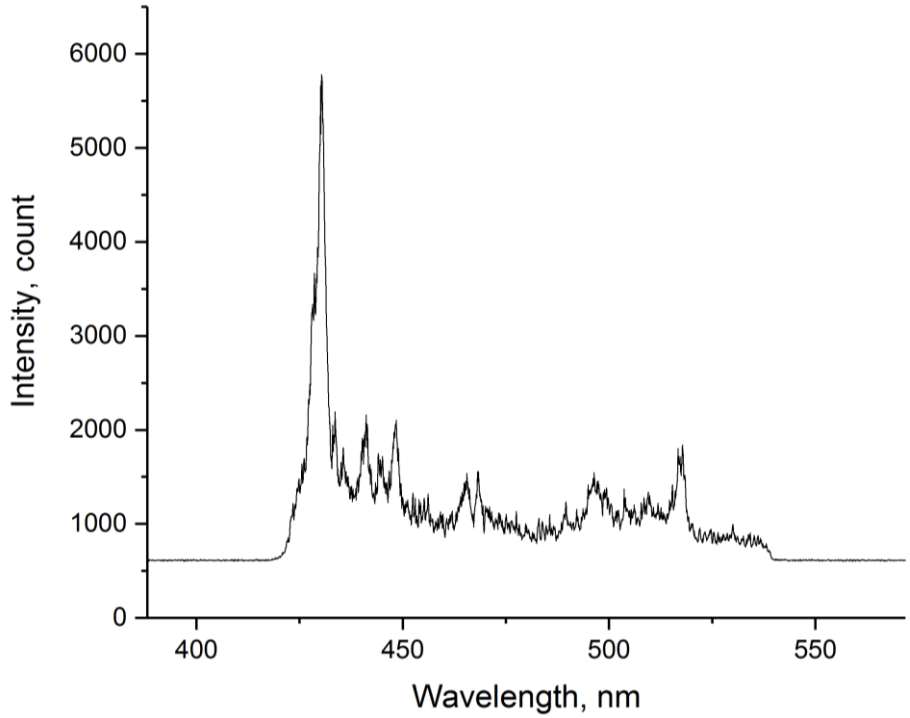

Figure 3.14: Taken 1480 (± 50) ns after the trigger, centred on 480 nm, with a 10 ns exposure, gain set to 120, this spectrum compares well with the PrismSpect trace in figure 3.15.

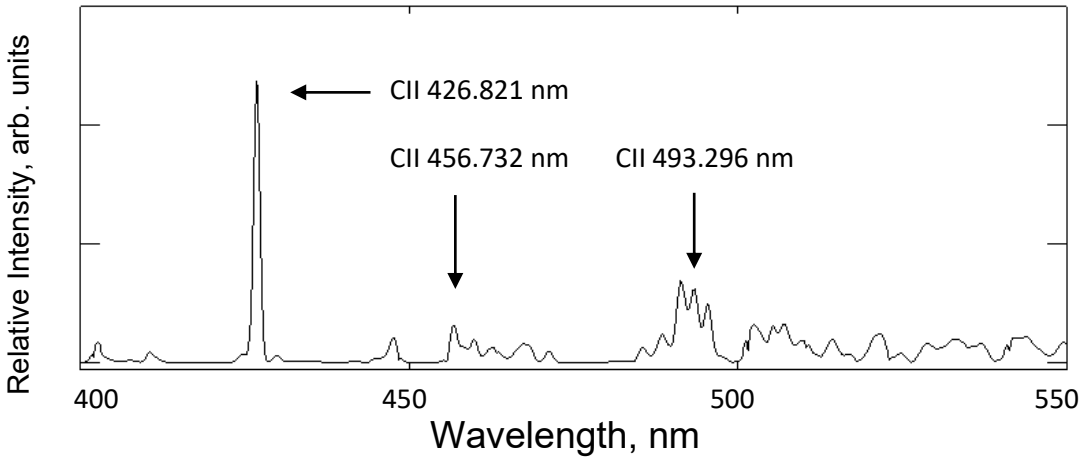

Figure 3.15: PrismSpect results 2 eV, 1e16 cm3

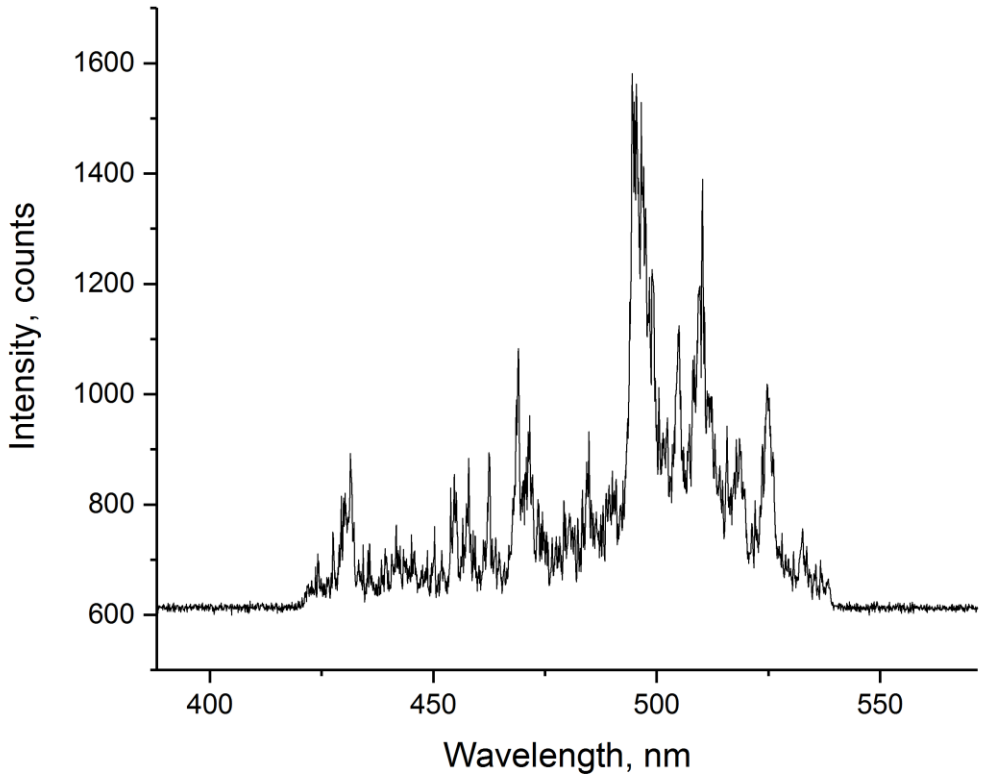

Figure 3.16: Spectrum taken at 2060 (± 50) ns after trigger, same settings as above

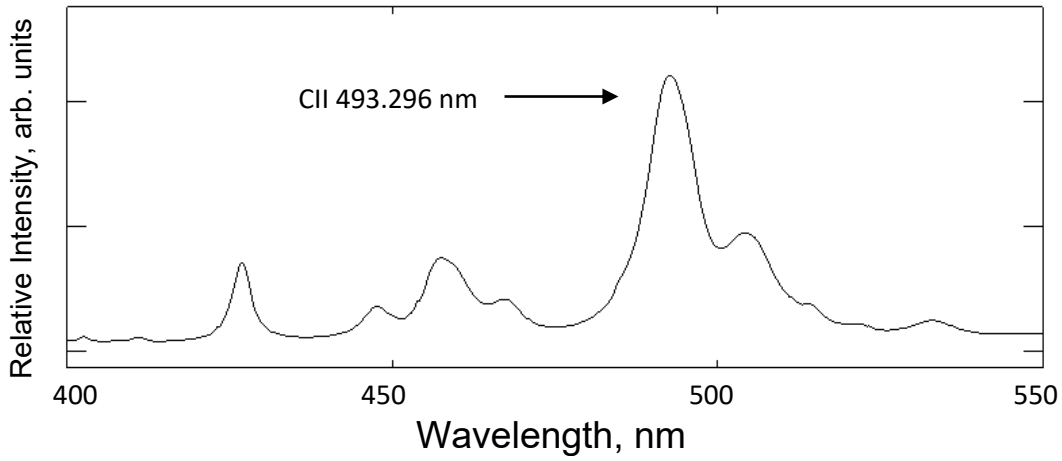

Figure 3.17: PrismSpect results 2 eV, 1e18 cm3

The three pairs of traces shown are intended to compare experimental results, taken at the same point in the plasma, though at different times after the trigger, with different points in the simulation that closely match the measured spectra.

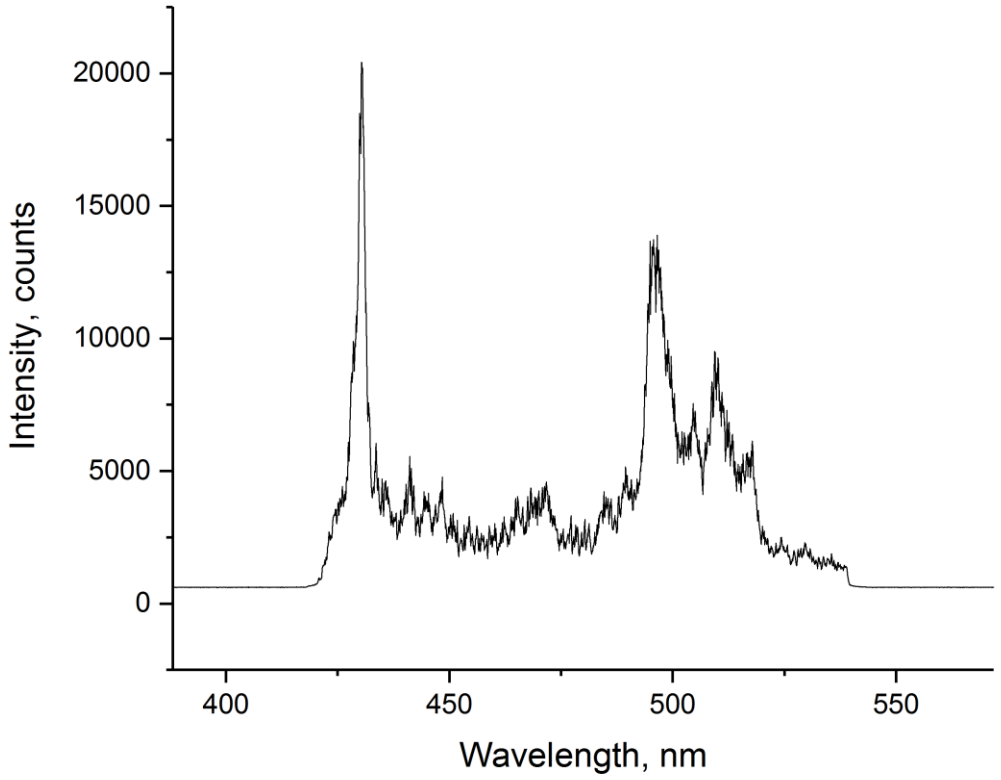

Figure 3.18: Spectrum acquired 3220 (± 50) ns after trigger, gain increased to 175.

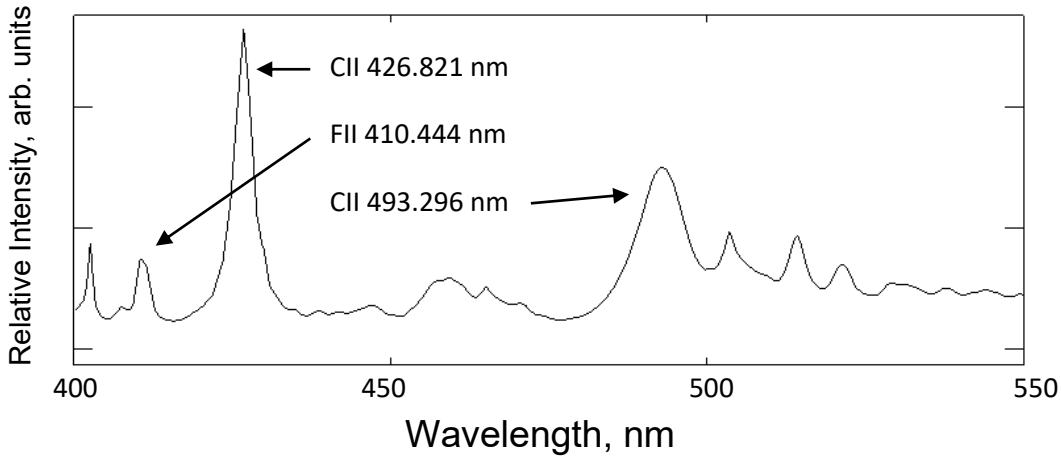

Figure 3.19: PrismSpect results 2.8 eV, 1e18 cm3

The simulations suggest how the plasma characteristics vary over time, with the density increasing from $1x10^{18}$ /cm^3 to $1x10^{18}$ /cm^3 initially, and then the temperature increases from 2 to 2.8 eV. Intuitively, this makes sense, as the insulator will continue to ablate more material into the plasma, and further ionisation will occur as the current flows.

3.1.5: Single Gun Thomson Scattering

Thomson scattering experiments were performed on a single gun output using the diagnostics chamber on MAGPIE. Two scattering angles were investigated, using bundles of fibre optics to collect the scattered light. Each bundle contains 7 fibres, arranged in a horizontal row. The bundles were located at scattering angles of 90° (referred to as "Bundle F") and 157.5° ("Bundle E"), with the scattered light being focussed into the bundle through two achromat lenses, both f=150 mm, acting as a telescope with a magnification factor of 1. The collection region for bundle F was 200 μm, the diameter of the collection fibres. Bundle E was situated at quite an oblique angle to the laser beam, leading to an elongation of the collection zone, meaning that the width of the 200 μm region is stretched to roughly 500 μm.

The collected light was captured by two iStar CCD cameras, after passing through Andor spectrometers with a 2400 line/mm grating, the gain was set to 3,500 for all shots.

The experiment output is an image from the CCD, showing the narrow linewidth of the 532 nm laser, delivered as a 10 ns, 3 J pulse. Because of the very low likelihood of a light being scattered into the fibre, it is necessary to use a high-power pulse to maximise the acquired signal. The timing of the laser relative to the plasma gun trigger was varied from ~0.5 μs to ~2 μs, to gain an understanding of the evolution of the plasma in the same timeframe as covered by the interferometry experiments. The plasma gun nozzle was 5 mm above the collection volume.

A sample image is shown in figure 3.20 acquired 1.1 μs after the start of the plasma gun current. The image shows 14 lines illuminated by the scattered light. The bottom seven are for the 90° scattering angle, from fibre bundle F, and the top seven are from the low angle scattering, from fibre bundle E. The image is very interesting, as it shows the utility of obtaining data from different scattering angles, accessing significantly different α regimes. The upper seven show a bright zone in the centre, at 532 nm, but also bright patches further out, whereas the lower seven show a broad central zone. The bright central zone is the minimally shifted scattered light. These different profiles are indicative

of the different regimes that Thomson scattering can investigate, collective, and non-collective. Non-collective behaviour arises from the random motion of the electrons, and manifests as a broadened central peak, as seen in the lower seven lines. Collective behaviour betrays information about the ion motion, such as the motion due to waves in the plasma and is seen in the upper seven. The distance between the central peak and the outer peaks on a collective profile provides information about the plasma density. The width of the outer peaks provides information about T_e. The central peak is broadened in both regimes, and is the sum of the central electron feature, giving information about T_e, and the ion peak, from which T_i can be discerned if the resolution of the system were higher.

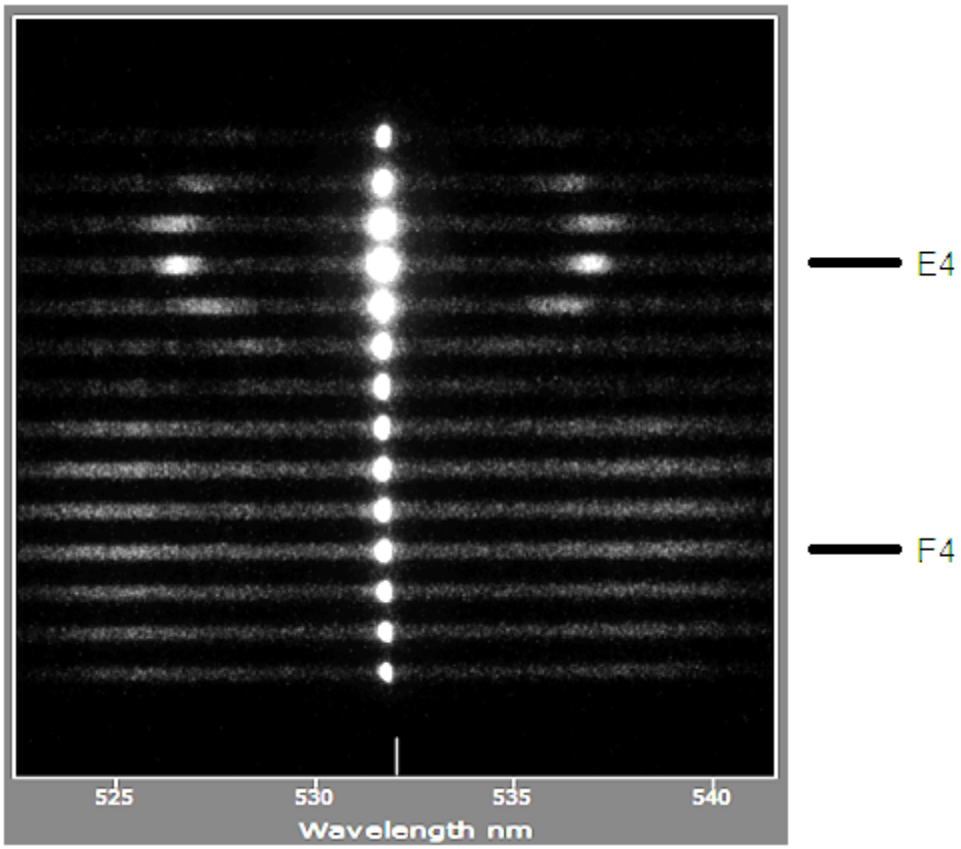

Figure 3.20: Image acquired for shot 23, 1.1 µs after plasma gun current starts, displayed in Andor's Solis software. E4 and F4 are the central fibres in each of the two fibre bundles.

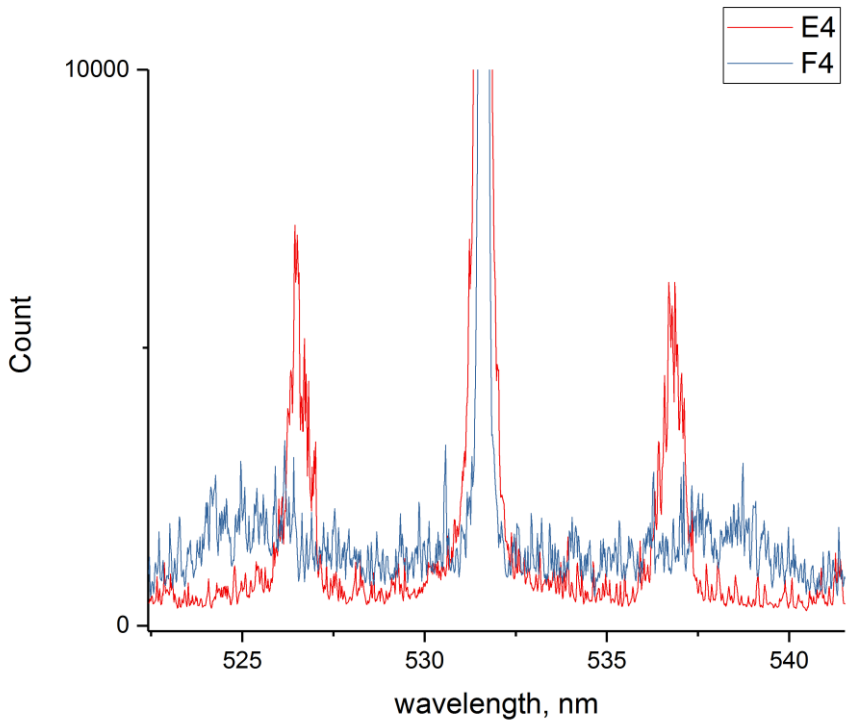

Figure 3.21: Raw profiles for fibre 4 from each bundle. Fibre 4's collection region is in the same location for both bundles, and so provides a good comparison of the different α regimes. Taken from shot g023. The central peak is clipped in order to show the detail of the side peaks, which have a much lower brightness. E4 is in the collective regime, F4 is non-collective.

The first observation to note is that the central peak does not change width under the different regimes, as the velocities in the plasma are too low to exhibit Doppler broadening to an extent measurable by the equipment. The image from the shot shows another very interesting feature. In the upper seven lines, changes in the distance away from the central peak at which the outer peaks appear are clearly evident. Fibre 4 is aligned with the centre of the plasma, and thus 5-7 and 3-1 move progressively further away from the centre. The change in the distance reflects the changing plasma density.

In order to extract the information about the plasma, the profiles need to be fitted to a form factor. This was calculated using software based on the process presented in [3.14], [3.13].

The analysis fits the profiles to an electron density of 1×10^{17} /cm^3. The electron temperature is fitted as 9 eV in the non-collective plot, from E4. These values are within the range presented in the literature, however, fitting F4's plot yields a less feasible temperature of ~20-30 eV. The fitting

process estimates the temperature of the electrons from, amongst other factors, the width of the outer electron features. In the trace from E4, these electron features are broadened, similarly to thermal broadening, which gives rise to the over-estimation of T_e. The broadening could be caused by a number of different factors, such as instrumentation broadening. Another potential cause is that the collection region covers a relatively wide area. Ordinarily, the MAGPIE system is focussed onto much smaller regions, but in this experiment, the region is 500 μm wide. It is perfectly reasonable that the plasma density is varying sufficiently over the collection width that the profile could contain contributions from many different densities, which when merged into a continuum, would appear as a broadened peak, skewing the fit to a higher T_e. These peaks are also not symmetrical about their peak value, either, another sign that they are not an ordinary peak, but a collection of superimposed peaks from slightly different distributions all contributing to a distorted single peak.

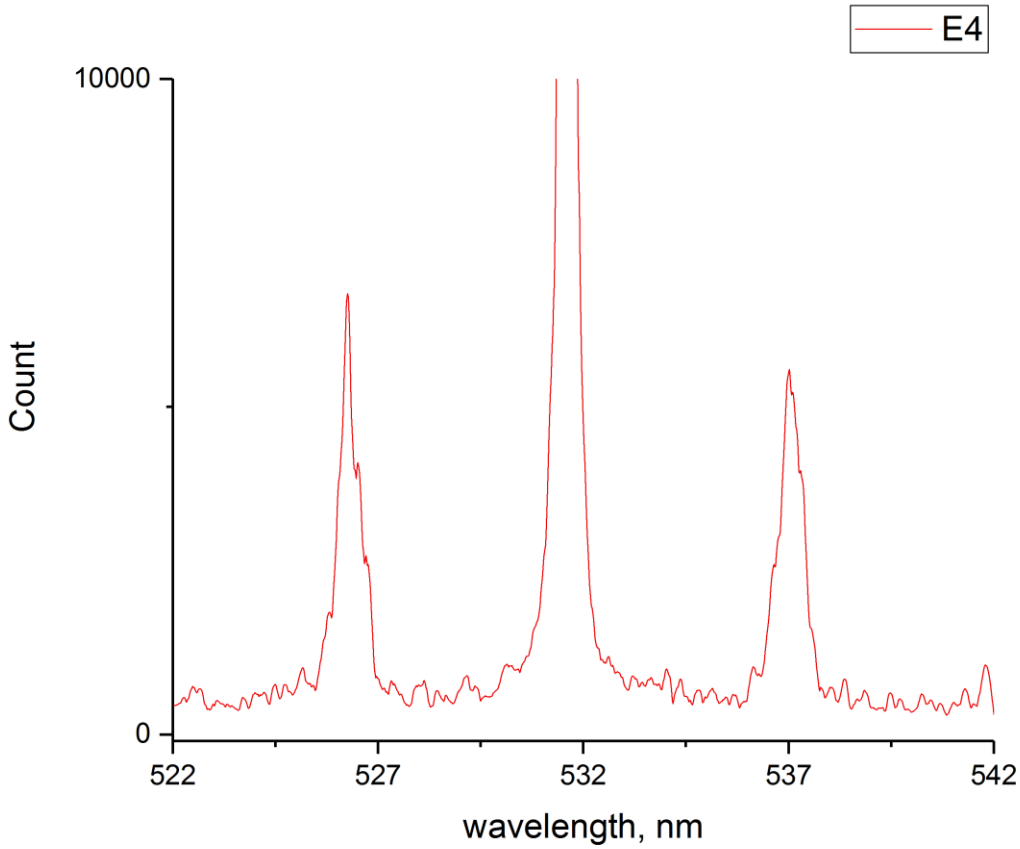

Figure 3.22: Smoothed (15 pt SG smoothing) profile from E4, from same shot. Note the asymmetry in the height of the outer electron peaks.

Another interesting point to note becomes evident once the profile data is smoothed slightly (using Savitzky-Golay, [3.15], with a window of 15 points). The outer features show a difference in height. The most likely cause is geometric elongation of the collection volumes. Another explanation could be that the CCD sensor has an uneven flat field, meaning that even illumination across the width of the device could lead to a gradient in the recorded signal or electron drift causing preferential scattering of the light. Most of these options have been largely discounted, as the lines from the F bundle do not show this same asymmetry, geometric elongation remains the most likely explanation.

3.2: Six Gun Results

Single gun experiments give detailed information to feed into Gorgon simulations, but do not convey anything about the interaction of converging streams from multiple guns, as they are configured in

the PFRP. For this, the study was extended to explore 6 guns firing in a configuration similar to the usual PFRP arrangement, with and without a rod at the centre.

3.2.1: Spatial Interferometry

3.2.1.1: Convergence tests

Spatial interferometry measurements of six guns converging helps determine how the plasma from the guns collide and interact. On the axis of the PFRP, the plasma will collide with the solid rod and the density will increase. The images can also show the effects of collisionality between adjacent plasma ejections. Figure 3.23 shows the electron line density measured in an experiment with 6 plasma guns and a central rod. Despite best efforts, alignment of the rod with the guns could vary by +/- 2mm (due to the restricted access, and the way in which the rod was mounted to minimise the impact on the interferometry); which also illustrates how difficult it is to achieve accurate alignment in actual PFRP experiments. As expected, the plasma density increases close to the rod, but is slightly distorted around it due to the misalignment.

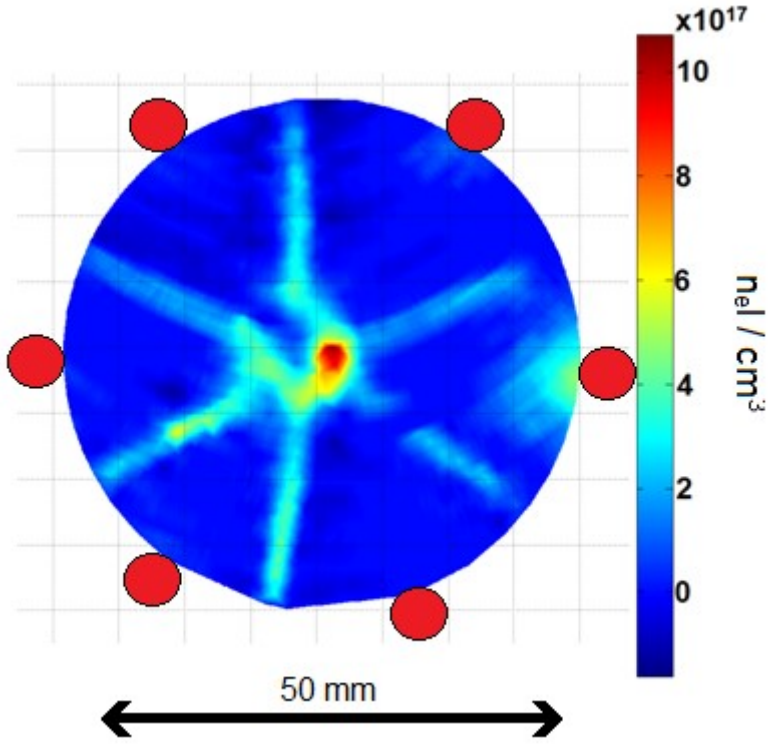

Figure 3.23: A symmetrical six gun convergence pattern, converging onto a rod centred on axis to within ~2mm. Red markers denote plasma gun locations.

The lines of increased density that stretch from the outside of the figure to the centre, however, do not directly originate from the guns, but from the region in between the guns – where the diverging plasma meet, demonstrating that the plasma is indeed collisional over this distance.

3.2.1.2: Asymmetries in plasma convergence

On several occasions during the single gun experiments, it was noted that a gun could fail to produce any plasma but the Rogowski coil would still register a current, suggesting an internal breakdown had occurred. With the six gun configuration any similar gun failure was detectable through interferometry, as can be seen in the left image of figure 3.24. With one non-working gun, the density map extracted from the interferograms was obviously not axisymmetric.

Experiments also showed how important it is to carefully align the six guns around the rod. The image on the right in figure 3.24 shows spatial interferometry results from all six guns firing but with one gun being bent slightly out of the plane of the rest of the guns. A simple alignment ring was 3D printed to help correct this problem.

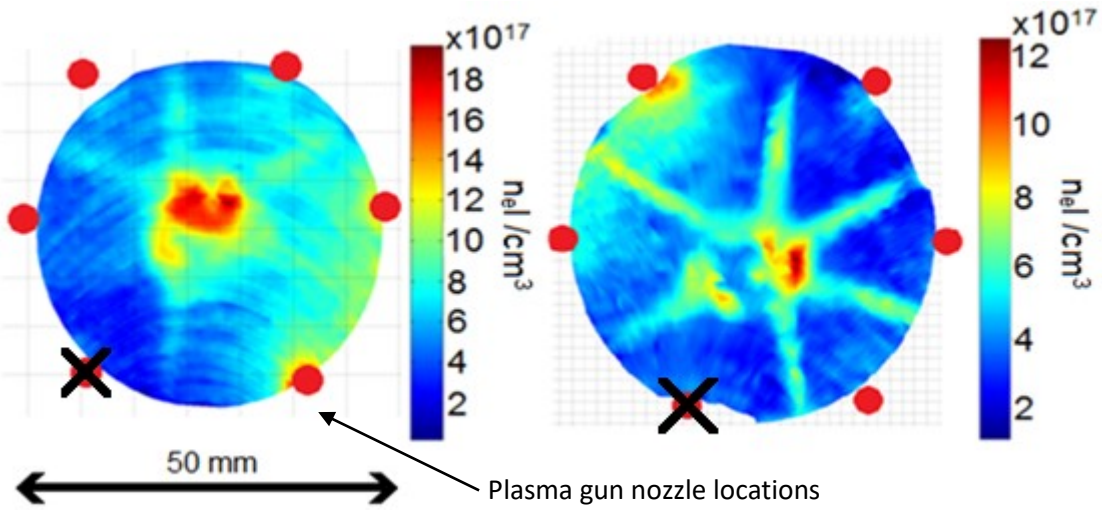

Figure 3.24: An example of asymmetric convergence resulting from a non-firing plasma gun, left, marked with an "X" and a misaligned gun, right, also marked with an "X". (Note: Dense regions at the edges of the examples are plasma guns firing as the system rings. Note also that the regions of mapped density are displayed as elliptical in the plots above, this is due to the space of the mask used during the fringe tracking stage, chosen to maximise the area capturing useful fringes).

Chapter 4: MagnetoHydroDynamic simulations

The previous chapters have focussed on the experimental characterisation of the plasma ejected from the plasma guns. The second aspect of the study is to develop a computer model of the PFRP that can be used to understand the plasma dynamics and factors that may affect the operation of the PFRP.

There are two main types of plasma simulation code, PiC and MHD. PiC, or Particle in Cell, codes apply the electromagnetic forces to discrete particles. Due to the huge numbers of particles, calculating the behaviours of every particle is not feasible with present computers, even for a small volume, on a modern supercomputing cluster. To improve the situation, particles are grouped together into so-called quasiparticles, also known as macroparticles. The volume being simulated is divided into a 3D mesh-like grid, and the motion of these grouped particles in each cell is calculated at each time step. MHD codes operate according to the rules of magnetohydrodynamics, a technique of predicting plasma behaviour by reducing the countless particles to a set of equations. These equations describe the behaviour of the particles as if they were a contiguous fluid, describing their behaviour in terms of quantities such as pressure and velocity. The behaviour of the plasma "fluid" is calculated on small volumes at each time step.

So, whilst PiC codes predict the collective behaviour of particles and variations to the distribution function, MHD codes model the macroscopic behaviour of the whole plasma, assuming certain distributions, such as Maxwellian. It is generally impracticable to model large systems using the PiC approach, as the requirements for large numbers of macroparticles to obtain reasonable statistics is simply too huge for even modern supercomputer clusters. PiC simulations can cope much better with systems that feature vacuum, and they can model particle transport and surface emission.

[4.1] modelled the PFRP in 2D only using Mach 2D (MHD) to model the snowplough phase, switching to LSP (PiC) for the low density regions. They used a C+ plasma, at 1 eV, with a radial velocity

towards the rod of 20 mm/μs. They noted a denser plasma region forming a current sheath, a few mm thick. They did note a discrepancy between their experiment and simulation data though. Their interferometry showed a denser region of plasma at the surface of the rod, which was absent in the simulation results. They felt that this difference is due to the MHD code not simulating the processes causing the increased density, such as heating of the rod, ion bombardment or the ionization of neutrals.

Once the current sheath has travelled down the rod, the plasma density at the tip decreases to a value below that which the code treats as a plasma, instead it treats it as a resistive immobile medium. LSP was able to provide insights into the behaviour of the region at the rod tip, showing how a beam can form there at the end of the low impedance MHD phase. The same paper also investigates the plasma formed by the anode as it expands due to heating as the current flows.

In this study, similar to [4.1], an MHD code was chosen to investigate the plasma pre-fill formation and the subsequent snowplough phase. The chosen code, Gorgon, is a fully 3D code, so can simulate 3D phenomena directly, rather than calculating in 2D and then inferring symmetry, as has been done in previous studies. This will enable effects such as asymmetric plasma flows from the guns to be explored. Gorgon, however, does not have an operational PiC module so the formation of the electron beam at the end of the snowplough was not modelled and is left for future research.

4.1: Equations and assumptions in MHD

MHD arises from fluid dynamics, the equations are derived by taking moments from the Vlasov-Fokker-Planck equation [4.2], which describes the evolution of the distribution function, f:

$$\frac{\partial f}{\partial t} + \boldsymbol{v}.\nabla f + \frac{q}{m}(\boldsymbol{E} + \boldsymbol{v} \times \boldsymbol{B}).\nabla_v f = \left(\frac{\partial f}{\partial t}\right)_{coll} \quad \text{(Eq 4.1)}$$

The Vlasov equation describes the evolution of a single fluid. The term on the right contains all the collisions (including recombinations), the terms on the left (in order) represent local changes to the distribution function, changes caused by moving the volume into a different region and Lorentz

forces. To obtain equations relating to macroscopic quantities, moments of the equation need to be taken. Taking the *k*th moment involves $\int f v^k d^3v = n\bar{v}^m$. [4.2] cover this process well.

The zeroth order moment gives the mass conservation equations, providing the fluid densities. There are two equations for the fluid, one for the electrons, and one for the ions. First order moments give momentum and second order moments give energy equations. For each additional order moment, new variables are introduced, so the third order moment is replaced with the generalised form of heat flow vector.

By combining these equations with Maxwell's equations gives the resistive MHD equations, according to [4.3]:

$$\frac{\partial \rho}{\partial t} = -\rho \nabla . \boldsymbol{v} \quad \text{(Eq. 4.2, conservation of mass)}$$

$$\frac{\rho \partial \boldsymbol{v}}{\partial t} = (\nabla \times \boldsymbol{B}) \times \frac{\boldsymbol{B}}{\mu_0} - \nabla P \quad \text{(Eq. 4.3, conservation of momentum)}$$

$$\frac{\partial P}{\partial t} = -\gamma P \nabla . \boldsymbol{v} + (\gamma + 1)(\nabla \times B)^2 / \sigma \mu_0 \quad \text{(Eq. 4.4, conservation of energy)}$$

$$\nabla . \boldsymbol{B} = 0 \quad \text{(Eq. 4.5, Gauss' law, magnetic divergence constraint)}$$

$$\boldsymbol{E} = \frac{(\nabla \times \boldsymbol{B})}{\sigma \mu_0} - \boldsymbol{v} \times \boldsymbol{B} \quad \text{(Eq. 4.6, MHD version of Ohm's law)}$$

$$\boldsymbol{j} = (\nabla \times \boldsymbol{B}) / \mu_0 \quad \text{(Eq. 4.7, Ampere's law)}$$

$\mathbf{E}$ is the electric field, P_e is the electron pressure, ρ is the mass density, dominated by the ion mass, v is the macroscopic fluid velocity, P is the total pressure, equal to the sum of the ion and electron pressures, and taken as a scalar following the fact that the plasma is assumed to be highly collisional. σ is the plasma conductivity, $\boldsymbol{j}$ is current density. Eq. 4.4, where the plasma is modelled as a conducting gas is not generally used.

The Ideal MHD Ohm's law **E** + **v** x **B** = 0 can also be written as **j** = σ(**E** + **v** x **B**). Using Ampére, **j** = $(\nabla \times \boldsymbol{B})/\sigma\mu_0$, leads to **E** = $\frac{\nabla \times \boldsymbol{B}}{\sigma\mu_0}$ - **v** x **B**.

As $\nabla \times \boldsymbol{E} = -\partial \boldsymbol{B}/\partial t$, according to Faraday, the equation describing the evolution of the magnetic field, known as the induction equation can be derived, (Eq 4.8), which can contain an extra term, (**j** x **B** - $\nabla \mathbf{P}\mathrm{e}$) to describe the balance of forces on the electrons when the plasma is collisional:

$$\mathbf{E} + \boldsymbol{v} \times \mathbf{B} = \frac{1}{en}(\mathbf{J} \times \mathbf{B} - \nabla Pe) + \frac{\boldsymbol{J}}{\boldsymbol{\sigma}} \text{ (Eq. 4.8)}$$

In ideal (non-resistive) MHD, the second term on the right (J/σ), which describes the dissipative resistivity, is assumed to be negligible. Resistive MHD codes however, implement it. The first term on the right is the Hall term, which is not typically implemented in MHD codes.

[4.3] explains how ∇Pe can be neglected if the length scales of the phenomenon are much greater than the ion Larmor radius. Estimates discussed below suggest this to be the case, so the equation describing the evolution of the magnetic field (Eq. 4.8) becomes:

$$\frac{\partial \boldsymbol{B}}{\partial t} = \nabla \times \left(\frac{\nabla \times \boldsymbol{B}}{\sigma\mu_0}\right) + \nabla \times (\boldsymbol{v} \times \mathbf{B}) - \nabla \times \left(\frac{\mathbf{J}}{\mathrm{n_e e}} \times \mathbf{B}\right) \text{ (Eq. 4.9)}$$

Within each MHD iteration, the electromagnetic equations are solved. The timescales required to be resolved are much smaller than for the MHD cycles, so these steps are performed within each MHD cycle. Measures to prevent numerical instabilities are also calculated within each iteration.

4.1.1: A Simple MHD framework

- The timescales of interest are significantly longer than collision frequencies. This leads to Maxwellian population distributions, electron and ion temperatures being equalised.
- Frequencies applied to the system are much lower than the plasma frequency, and the electron cyclotron frequency, meaning the electrons will be able to respond to any changes imposed on the system.

- Length scales are longer than both the Debye length and the ion Larmor radius. Specifying this restriction means the plasma can be considered quasi-neutral and Larmor-radius scale effects can be neglected.
- Electrons are not relativistic.
- Due to the collisional nature of the plasma, pressure is isotropic.

In ideal MHD, magnetic field lines are "frozen in", that is, they move with the plasma and the plasma moves with them. If the plasma compresses or stretches, the field lines compress or stretch with it. If the magnetic field expands, it can "push" the plasma. This behaviour is due to the fact that the timescales of the changes applied to the system are longer than the response times of the plasma. There are different formats of the MHD group of equations. Ideal MHD features no dissipation terms, whereas resistive MHD includes a resistivity term that enables the magnetic field lines to diffuse through the plasma.

4.2: Applicability of the MHD assumptions in the case of the PFRP

In the case of a plasma gun ejection, the density is in the range 10^{15} - 10^{18} /cm^3. The species present are mostly carbon and fluorine from the ablated PTFE insulator. [4.4] found that the plasma temperature is in the range of 3-10 eV; this is corroborated by the results of the experimental phase of the present work, where spectroscopy estimates the temperature to be in the region of 2-3 eV, and Thomson scattering estimates it at 9 eV. The length scale is a few centimetres, the magnetic field arising from the current pulse passing through the rod evolves over a couple of hundred nanoseconds. Checking the plasma pre-fill against the requirements for applicability of MHD shows that they are all met during the phase of operation where the plasma travels along the rod. The requirements are:

Collision frequency: calculations in chapter 3 show the plasma is collisional in certain regions, such as around the rod. The electron density distribution maps obtained from the spatial interferometry experiments support these calculations.

Debye length: The Debye length describes the scaling of the shielding of the ions by the electrons. If phenomena occur over length scales less than the Debye length [4.5], the quasineutrality of the plasma is not relevant, the discrete charges can be affected. Given by:

$$\lambda_D = \sqrt{\frac{\varepsilon_0 k_B T_e}{n_e e^2}} \quad \text{(Eq. 4.12)}$$

The Debye lengths pertaining to the plasma regimes in the pre-fill are sub-mm to sub-µm, much less than length scale of plasma.

Ion Larmor radius: In the presence of a magnetic field, the ion trajectory is curved. In intense fields, the curvature closes to an orbit around the field line. This helical path greatly increases the chances of the ion colliding with another particle, and so the ions can be approximated as a single fluid, rather than individual particles.

The radius of curvature is given by $r_L = v_i/\omega_i$, where $\omega_i = eB/m_i$. Using the equation for a field induced in a wire, $B = \mu_0 I/2\pi r$, it is possible to estimate the fields in the PFRP. Taking r as just outside the radius of the 1 mm rod, the ion cyclotron radius is in the micrometre range, much less than the length scale of the plasma. Further from the rod, the radius grows, being only sub millimetre at 25 mm.

Electron velocity, v_e = ~5×10^3 m/s - not relativistic. This is estimated by calculating the thermal velocity [4.5] of the electrons using:

$$v_{th} = \sqrt{\frac{3k_B T_e}{m_e}} \quad \text{(eq. 4.13).}$$

There could also be acceleration due to electric fields. If they are absent, the plasma evolution would be driven by pressure alone and would be isotropic. If there are accelerating forces acting on the plasma, it would evolve faster in a particular direction, moving faster than the thermal speed of the electrons. This behaviour was indeed noted in the previous chapter, where the spatial interferometry showed the plasma expansion front to be travelling nearly three times faster than the thermal velocity. If quasineutrality applies, the presence of a pressure gradient sufficient to cause supersonic flow would need to be present. As the face of the plasma nozzle is machined to form a concave cone, the colliding outflows from the opposing faces would be potential source of a

suitable pressure gradient. [4.6] found their plasma gun simulations showed that a machined nozzle maintained a near constant flow velocity over a few μs, whereas a flat face showed significant modulation as the current oscillated. This suggests that the flow velocity of the plasma is affected by the fact that the machined nozzle provides the density gradient required.

Plasma frequency, w_p: If a phenomenon occurs on a timescale shorter than the plasma period, the plasma cannot react to it. The plasma frequency [4.5] is given by:

$$\omega_p = \sqrt{\frac{n_e e^2}{\varepsilon_0 m_e}} \quad \text{(eq 4.14)}.$$

The plasma frequency is in the THz range. As the current varies in tens of ns timescale, this requirement is met. The plasma density varies markedly across its extent, in the main varying between 10^{15} and 10^{18} /cm^3, leading to variations of the plasma frequency from ~2x10^{12} Hz to ~6x10^{13} Hz.

As the pre-fill meets all of the requirements of MHD, the use of MHD code for modelling the snowplough phase of the PFRP is justified.

4.3: Gorgon - a 3D MHD code

Gorgon [4.7, 4.8] is a 3D Eulerian MHD code written and maintained at Imperial College London and used in several universities and national laboratories to model the behaviour of plasmas in dense z pinches and inertial confinement capsules. It approximates the plasma as a single fluid, in that the ion and electron velocities are kept equal, but different temperatures for electrons and ions are possible. This can be for multiple materials, the natures of which are governed through Equation of State tables. The MHD equations are solved through iteratively stepping through time, calculating the motions of the plasma volume and then advecting them to adjacent cells, depending on the local and neighbouring cell properties. The equations are then solved for the next time step, accounting for the new properties of the plasma volumes.

The electromagnetic part of the solution is provided by the A-field solver. The EM equations are solved separately to the hydrodynamics ones, as in a vacuum region the magnetic fields can

propagate significantly faster than the plasma would move. Equations for the magnetic and electric fields are combined through the definition of the vector potential $\boldsymbol{A}$, $\nabla \times \boldsymbol{A} = \boldsymbol{B}$. Faraday's law leads to $\boldsymbol{E} = -\frac{\partial \boldsymbol{A}}{\partial t}$. Combining the resistive MHD Ohm's law, $\mathbf{E} + \mathbf{v} \times \mathbf{B} = \eta.\mathbf{j}$ and Ampére's law and re-arranging gives the equation that the A-field solver uses:

$$\frac{\partial A^2}{\partial t^2} = -c^2 \nabla \times (\nabla \times \boldsymbol{A}) + \frac{c^2 \mu_0}{\eta}\left(v \times (\nabla \times \boldsymbol{A}) - \frac{\partial \boldsymbol{A}}{\partial t}\right) \quad \text{(Eq. 4.15)}$$

Various simplifications are applied along the route to the MHD equations used in the simulations. At present, the effects of an additional term, the Hall term, are not included. The result of the Hall effect could be that the magnetic piston that compresses the pre-fill and pushes it off the rod is actually able to slip through into the plasma, often described as a leaky piston. This would modify the behaviour of the current passing through the pre-fill, potentially disrupting the behaviour of the PFRP. Without the Hall term, Gorgon may not accurately model the relatively very low density plasmas in the PFRP, particularly at the edges of the plasma, and when the plasma travels off the end of the rod.

Gorgon uses B field calculations to maintain the Maxwellian population in each cell in regions of low density where MHD would not strictly apply.

The two regimes are discussed in [4.4], and scale requirements to decide which occurs.

4.3.1: Modelling a single gun

It was decided early on in the study that modelling the plasma gun from first principles would be too computationally intensive and present more complications than benefits, so it was decided to simply represent it as a plasma source, specifying only a few parameters, namely density, temperature and injection velocity. The injection velocity term is included to provide a **j**x**B**-like propulsion of the plasma away from the nozzle. By varying the parameters, it was possible to approximate the behaviour of the plasma gun using this simplified method. The timescales and distances of interest are relatively constrained, as the plasma needs to be representative only during the operation of the PFRP, so a small window of a couple of μs is sufficient. Estimates of the velocity of the plasma front

were presented in the previous chapter, with values between 8,500 and 14,500 m/s being recorded, using the time taken by the plasma to reach the rod.

The 3D cartesian single gun simulation is comprised of a volume of vacuum, and a thin disk of cells set to be plasma with specific parameters, with a radius of 5 mm. The plasma source was chosen to be this form in order to simplify the modelling and reduce the computational load.

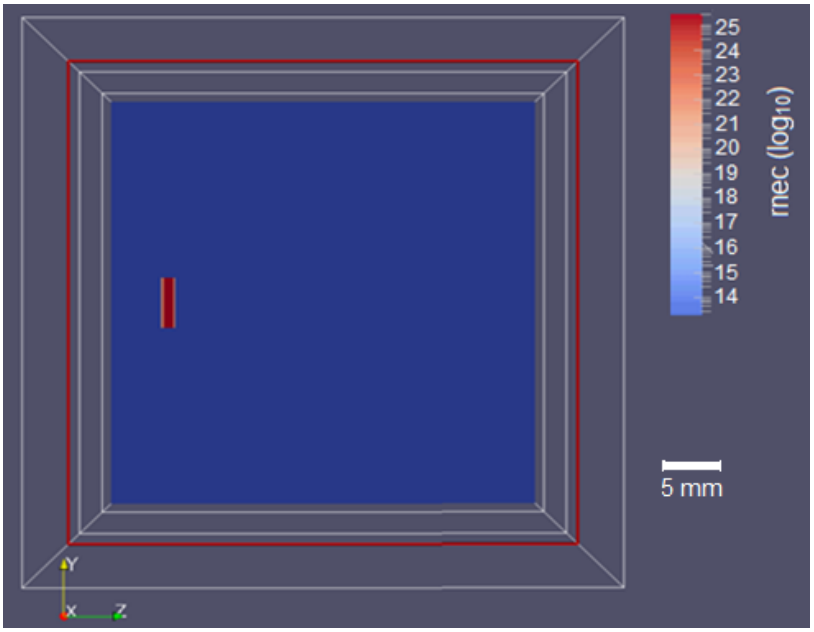

Figure 4.1: At the start of the simulation of the single plasma gun, the cells that act as the source of the plasma can be seen to the left of the image.

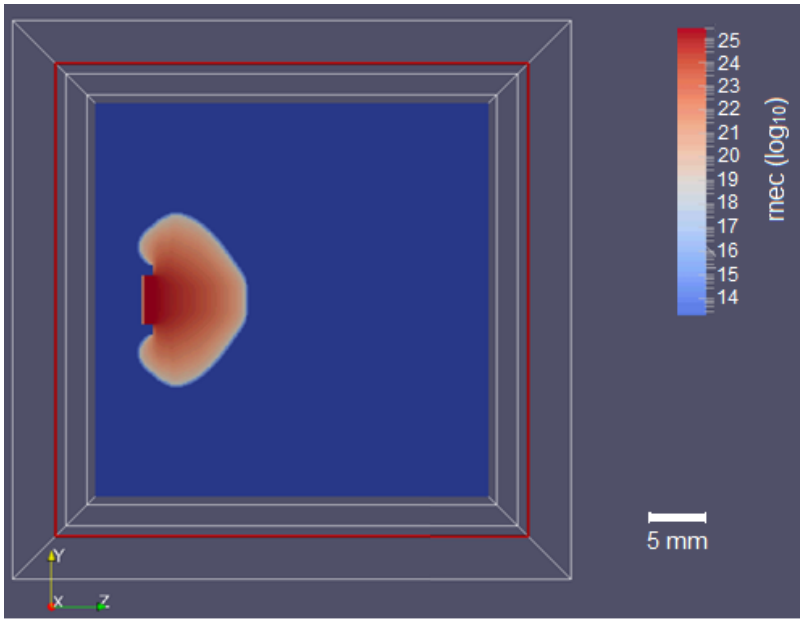

Figure 4.2: As the simulation evolves, here at 200 ns, the plasma diffuses out from the dense region of the source cells.

As the simulation runs, the plasma evolves away from the cells. Plasma is prevented from travelling backwards, behind the source, by zeroing the momentum for regions behind the source. It is not necessarily the case that the values of the parameters for the physical plasma match those used to generate the plasma in the simulation, as it is a simplified case being modelled, not the complete set of physical processes.

The state of the plasma at any point is determined by the equations of state, EoS, for each material, which govern the values of parameters such as pressure, internal energy and neutral-neutral bond strengths at a given temperature and density. Only the EoS for carbon was used in these simulations, there was no EoS available for fluorine.

The model space is a cube 270 cells on each side. The model space is split across 6,6,5 (x,y,z) domains, and so requires 180 computer cores to run, taking roughly 3 hours. The results from the spatial interferometry were used to inform the development of the simulation. These results do not convey very much detail about the plasma beyond about 15 mm as the density falls below the resolution of the technique at the wavelength used.

4.3.2: Multigun simulation

Once the correct values for the plasma source were identified, the model was extended to include the convergence of six guns around a rod. Extending the system to include six sources allowed comparison with six gun interferometry shots which include regions of increased density where the plasma converge or overlap. Once agreement was reached, the rod and cathode ring were added to the model. The rod was modelled as extending along the z-axis at the centre of the simulation space, protruding 25 mm in front of the cathode ring, and was set to be 0.5 mm in diameter. As interferometry was performed with a rod-like addition to the chamber, this gave further detail to the comparison. As with the usual configuration for the PFRP, the six plasma sources were located radially around the central axis, at 25 mm from the central rod. The anode rod and cathode ring were defined by specifying that the cells in certain regions are populated with an "electrode"

material. There were no anodes or cathodes in the simulation, just electrodes. Their relative polarities were governed by the current induced in them.

For the sake of testing the correctness of the plasma convergence quickly, the simulation is only run up to the point where the main current into the rod starts to flow (This is T_0).

The final stage of the simulating process was to add a current to the rod. This is achieved through the application of a magnetic field at the boundary, which is sized to give rise to a current in the rod. The basic current drive is a sinusoidal one, with amplitude and frequency set to be similar to the pulsed power drive applied by Gamble II, the machine providing the pulsed power in the paper presented by Weber et al. The parameters used were 75 ns to reach the peak current of 650 kA, with the current starting 800 ns after the plasma starts. This timing was chosen to match the usual timing of a PFRP shot.

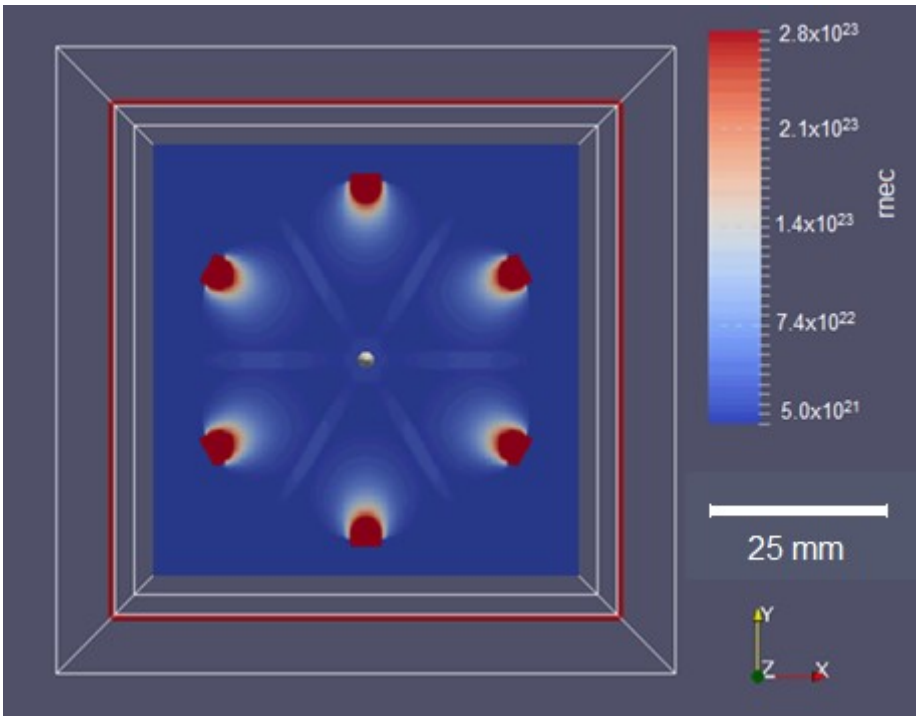

Figure 4.3: On axis view of simulated plasma convergence. The quantity rnec is the electron density, /m3 (Plasma sources are located 25 mm from the central axis, T=T0).

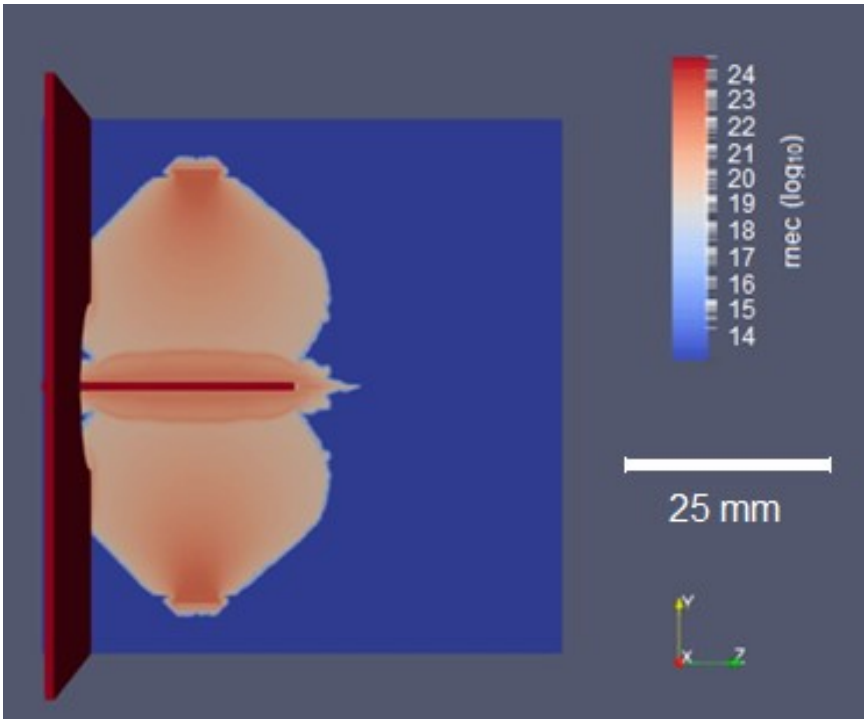

Figure 4.4: Side on view of a simulation, showing electrode placement, in dark red.

A full simulation took approximately 6 hours to run, with the workload divided over 144 cores. The simulation space is 64 mm per side, with 276 cells per side for the initial test runs, higher resolution to be used once a working model has been developed. Doubling the resolution in each axis increases the number of cells by a factor of eight, so it isn't wise to run a too high a resolution unless the model is known to be correct. A cubic simulation space was chosen because the region past the end of the rod was also of interest.

4.3.3: Analysing results

Presented in the following chapter, the results of simulations are primarily viewed in Paraview [4.9], a widely-used software capable of visualising large 3D datasets. VTKExplorer is a program written at Imperial College to support analysis of the data created during a simulation run. It has many switches and options but has been used here to integrate the densities of chosen parameters, such as plasma density, over the line of sight through the plasma from a detector of specified dimensions. In this mode of usage, it is possible to generate an output that enabled direct comparison between the simulation and experimentally obtained interferograms. Origin [4.10] is capable of plotting the data from both Magic and VTKExplorer, which facilitates the comparison.

Chapter 5: Simulations based on experimental data

5.1: Single Gun simulations

The simulation phase of this study initially focussed on a single plasma gun simulated as a volume plasma source defined by three parameters, density, injection velocity and temperature (gun_rho, gun_v and gun_T respectively). As described in chapter 4, the plasma in the volume will flow outwards as a result of the pressure gradient and the injected flow. These parameters were varied to understand how they affected the nature of the plasma. The main characteristics of the plasma under investigation were the divergence angle, velocity and density distribution of the plasma in the plasma. Starting values used for the parameter scan were gun_rho = $2x10^{-5}$ kg/cc, gun_v = $1x10^{4}$ m/s, and gun_T = 2 eV. Initially, values were varied by a factor of ten in order to quickly understand the nature of the effects of each parameter.

Line-integrated electron density maps were created from the simulations, allowing direct comparison with the experimental results. Such a comparison is shown in figure 5.1, with lineouts taken across the plasma were taken at 5.9 and 8.6 mm from the nozzle, to match those taken on the experimental data.

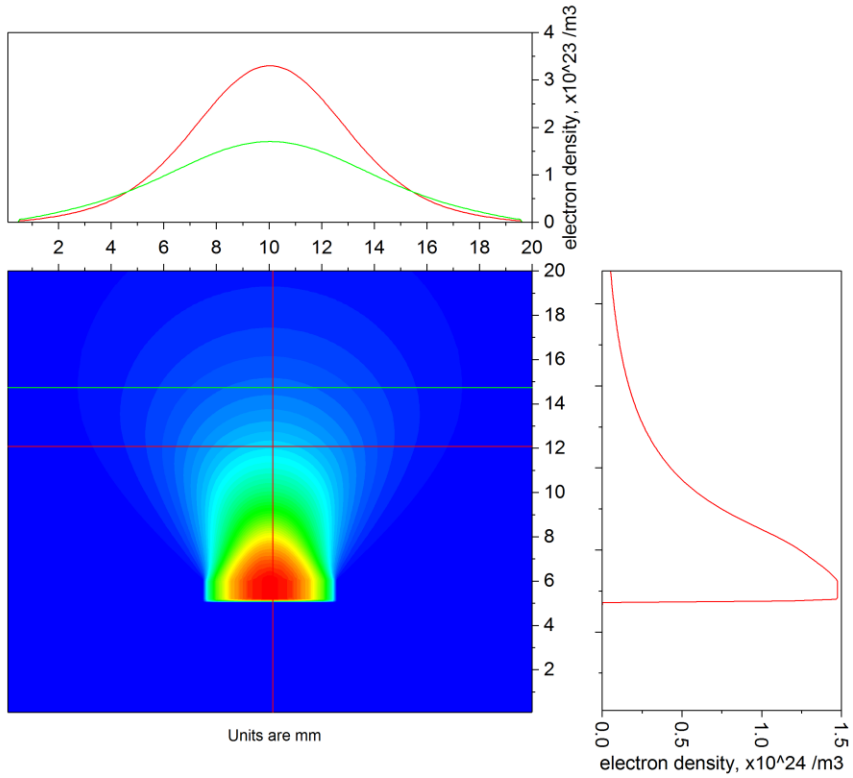

Figure 5.1: This is an example of the output of a simulation of a single gun. In this case, the plasma was generated by using the values: gun_rho=2x10^{-4} g/cc, gun_T=4 eV, gun_v = 2x10^{4} m/s. The green lineout is at 8.6 mm, the red is 5.9 mm.

It was noted that variations to the injection velocity didn't make very much difference to the plasma until the value was increased to at least 1x10^{5} m/s, at which point the expansion becomes strongly collimated, wherein the Alfvén Mach number, a dimensionless ratio of flow velocity to Alfvén velocity, becomes roughly 10. If the plasma is injected with sufficiently high velocity, the forward velocity will be greater than the thermal or sound velocities. For lower velocities, however, the mean free path between collisions is shorter, and the injected particles are slowed down, and thermalised, by the rest of the plasma.

Figure 5.2 shows the effect of the injection velocity becoming greater than the thermal velocity of the plasma with collimation becoming evident.

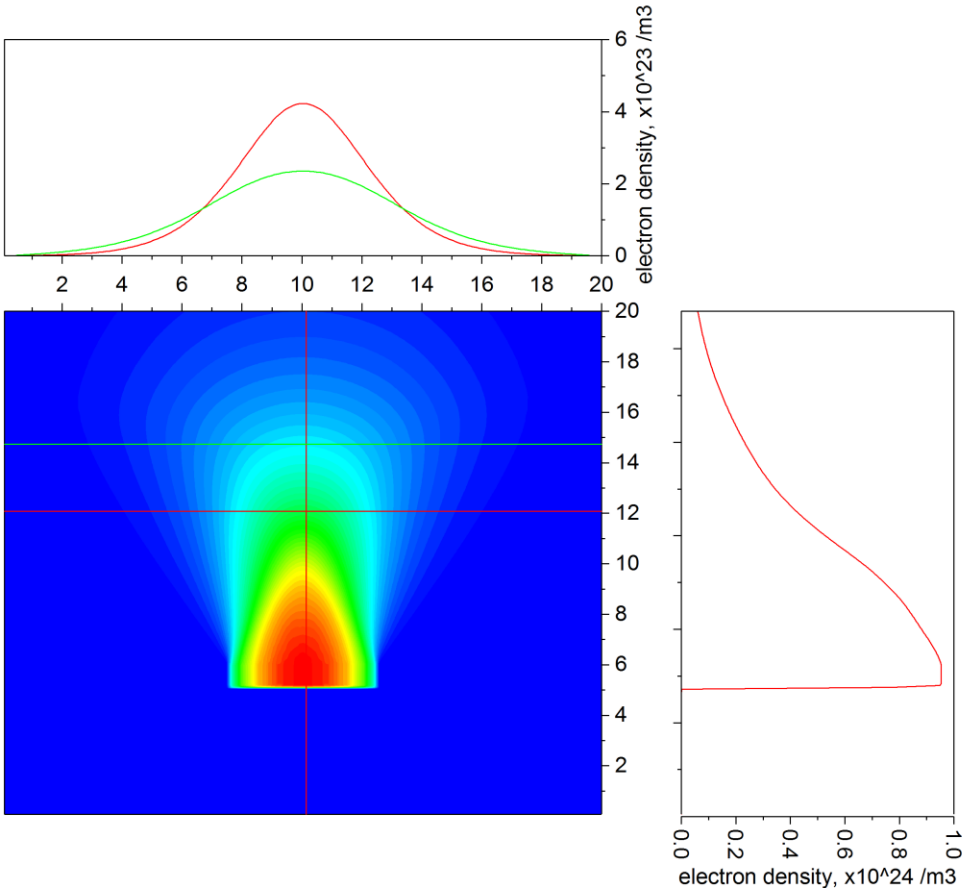

Figure 5.2: When the injection velocity is too high, the plasma becomes more collimated. The axial density profile no longer matches experimental results, see figure 5.8 for comparison (gun_rho=2x10^{-4} g/cc,gun_v=2x10^{4} m/s,Te=2 eV) The green lineout is at 5.9 mm, the red is at 8.6 mm.

Altering the temperature of the plasma gives rise to variations in the plasma shape, higher temperatures leading to greater divergence as the thermal velocity overrides the influences of the injection velocity. Density variations affect the behaviour as well. In this case, it is the density gradient that drives the plasma outward.

This is best illustrated by comparing the lineouts for the two above examples, one is the results from 2 eV, the other is for 4 eV, taken at the same time in the plasma evolution, at two distances from the nozzle.

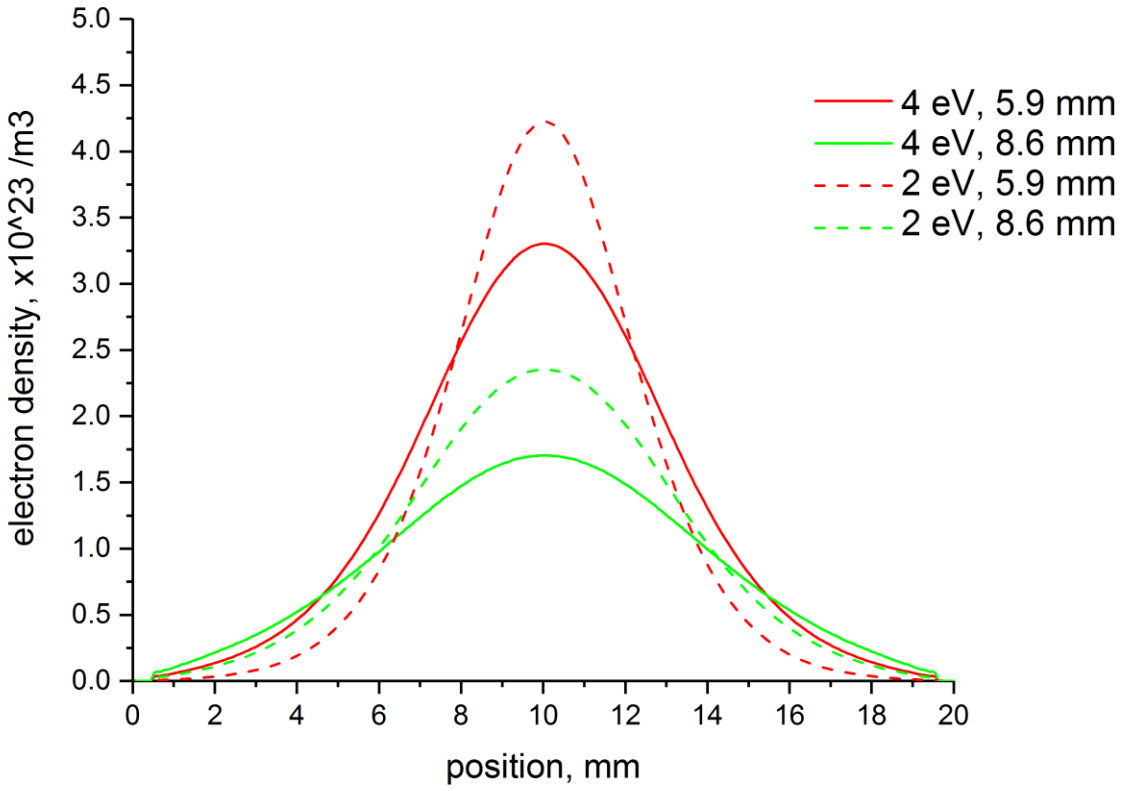

Figure 5.3: Comparing lineouts for two simulations of different electron temperatures. Divergence is ascertained by studying the increase in the width of the plasma at different distances from the nozzle.

The same analysis can be performed for two simulations using different densities, as shown in figure 5.4. Increasing density leads to greater divergence and a more rapid expansion.

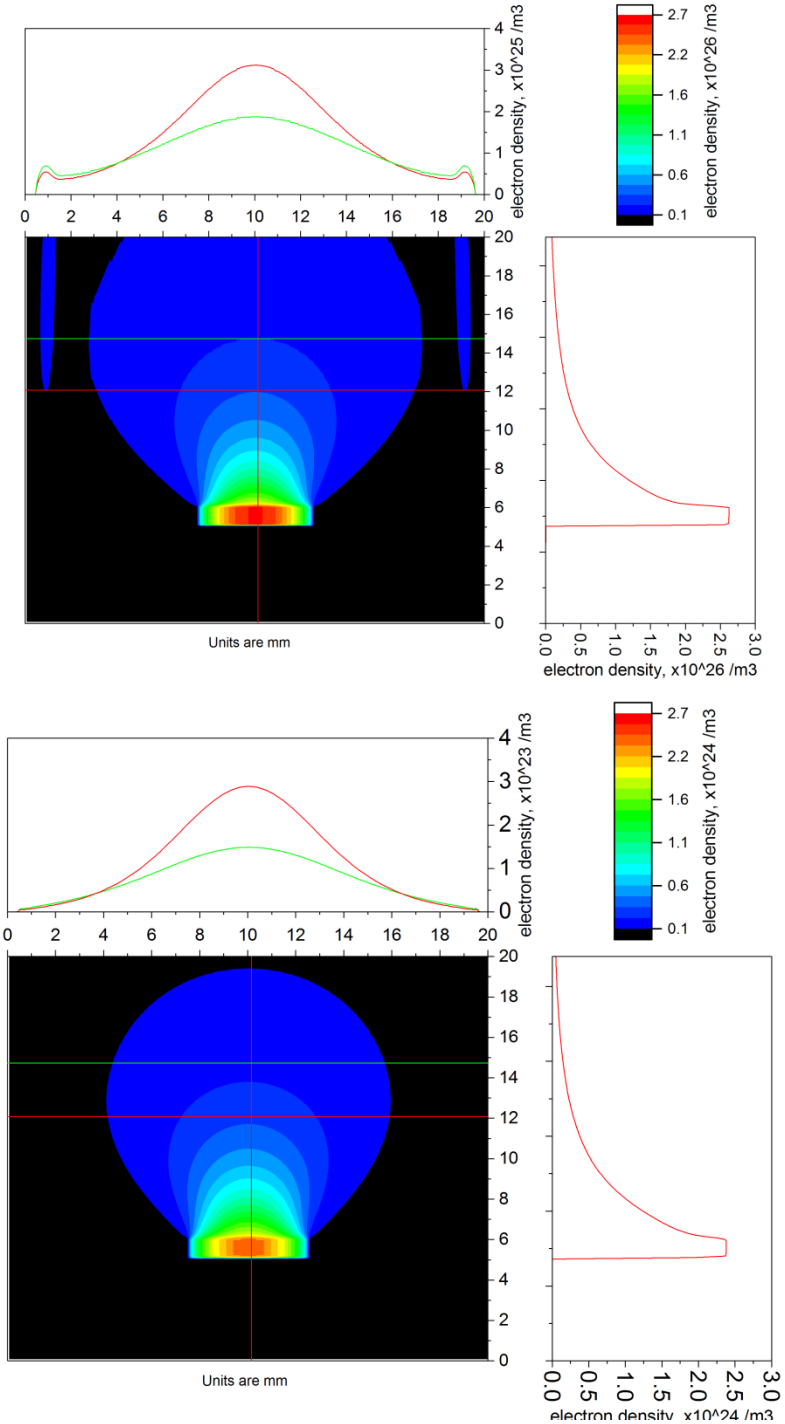

Figure 5.4: Keeping temperature and injection velocity equal and varying only density leads to a difference in the divergence of the plasma. The upper image used gun_rho=2x10^{-2} kg/cc, the lower one used gun_rho=2x10^{-4} kg/cc. The lower density contour limit is set to 2% of the maximum density on both images. The lobes visible on the upper image are purely an artefact arising from the boundary conditions on the simulation volume and can be disregarded.

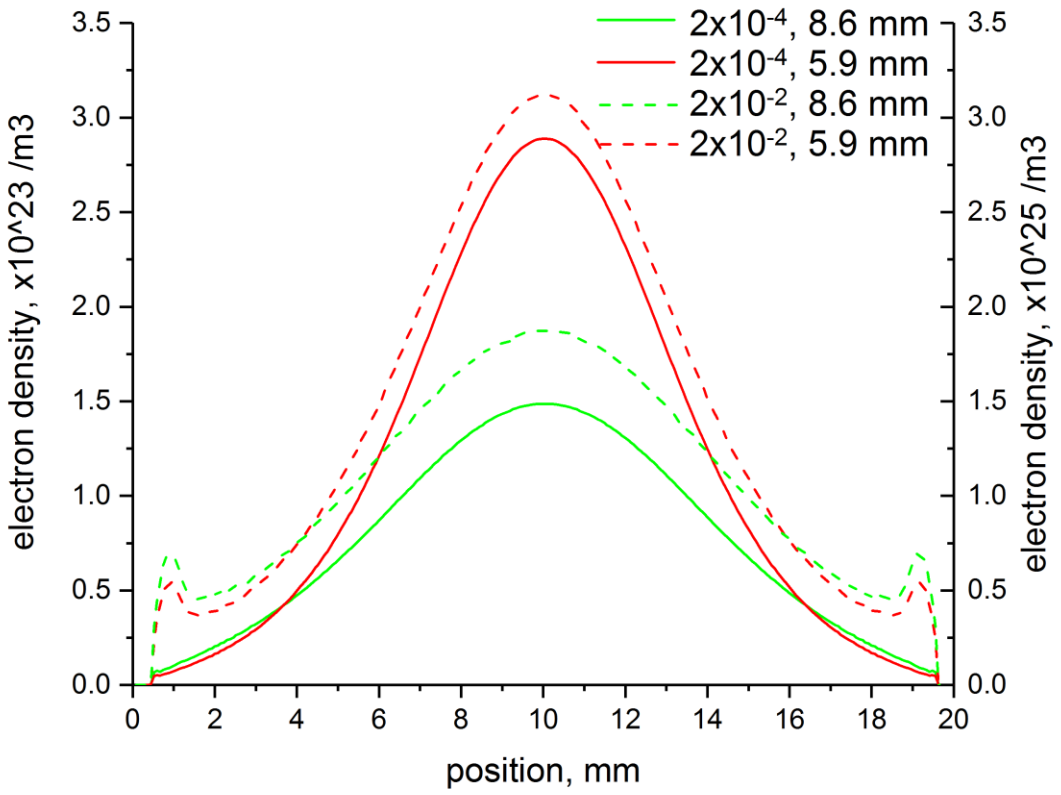

Figure 5.5: Comparing the lineouts directly, the solid lines relate to the lower image in the previous figure, the lower density variant. Left axis applies to lower density result, right axis applies to higher density variant.

By adjusting velocity, density and temperature simultaneously, it was possible to find a set of parameters that lead to the plasma exhibiting similar behaviour to that which was noted during the interferometry investigation of plasma behaviour. The parameter scan was performed over a large range of values for each variable, gun_rho was varied from $1x10^{-6}$ and 0.1, gun_T ranged between 1 and 10 eV and gun_v varied between $1x10^{2}$ and $1x10^{5}$ m/s. This wide range of values bracketed those expected from the literature, with considerable margin. The size of the ranges necessitated large steps in each value, gun_T was varied in 1 eV steps, gun_rho and gun_v were varied by a factor of ten initially, in order to converge on a suitable value. This tactic enabled a good understanding of how these factors affect the plasma evolution to be gained very quickly. Changes this significant are required to discern a marked difference in shape, not density, between simulations, and so the

resultant parameters are guidelines insofar as they provide a good match to the physical results without having to run many extra simulations to home in on exact values.

The main method of comparison was to first measure the velocity of the plasma expansion, and qualitatively compare the shape of the plasma. Velocity measurements were made by measuring the extent of the plasma (at a given density contour) at different times. The contour plot function within Origin features a line out tool, which was used to quantitatively study the plasma extent. The interferometry frames were chosen that provided the clearest signals of the position of the expansion front. One option is to use the frame showing the movement of fringes at the rod (in initial experiments, a small copper plate was used as an obstacle, serving a similar function to the rod). The rod is a known distance from the nozzle, and so, velocities can be judged. There is ambiguity in this method however, as it isn't always perfectly clear when the expansion front arrives at the rod. It may arrive in between frames, for example. The expansion front is not perfectly defined either, and the density resolution of the interferometer is best estimated as 25% of the fringe density, which for the 532 nm laser is approximately 7×10^{16} /cm^3.

In a similar way to experiments, the expansion velocity estimates from simulations were obtained by generating line-integrated electron density plots at times similar to the frames taken from the interferometry, and the same density isobar used to determine the extent of the plasma. For the removal of ambiguity, lineouts were taken to ascertain the density profile. The Thomson scattering and spectroscopy experiments discussed in chapter 3 provide information on the temperature, estimating it to be 8-24 eV in the central region of the plasma.

Comparing the images in figure 5.6 of a slightly underdivergent plasma shows the difference that the temperature value can give. The plasma divergence increases as the temperature increases, a result of the thermal velocities of the plasma species being higher. When varying the multiple parameters to obtain a specific shape and speed, other combinations arose that led to the seemingly correct

velocities and divergences, but once density is also taken into consideration, however, the number of combinations is dramatically decreased.

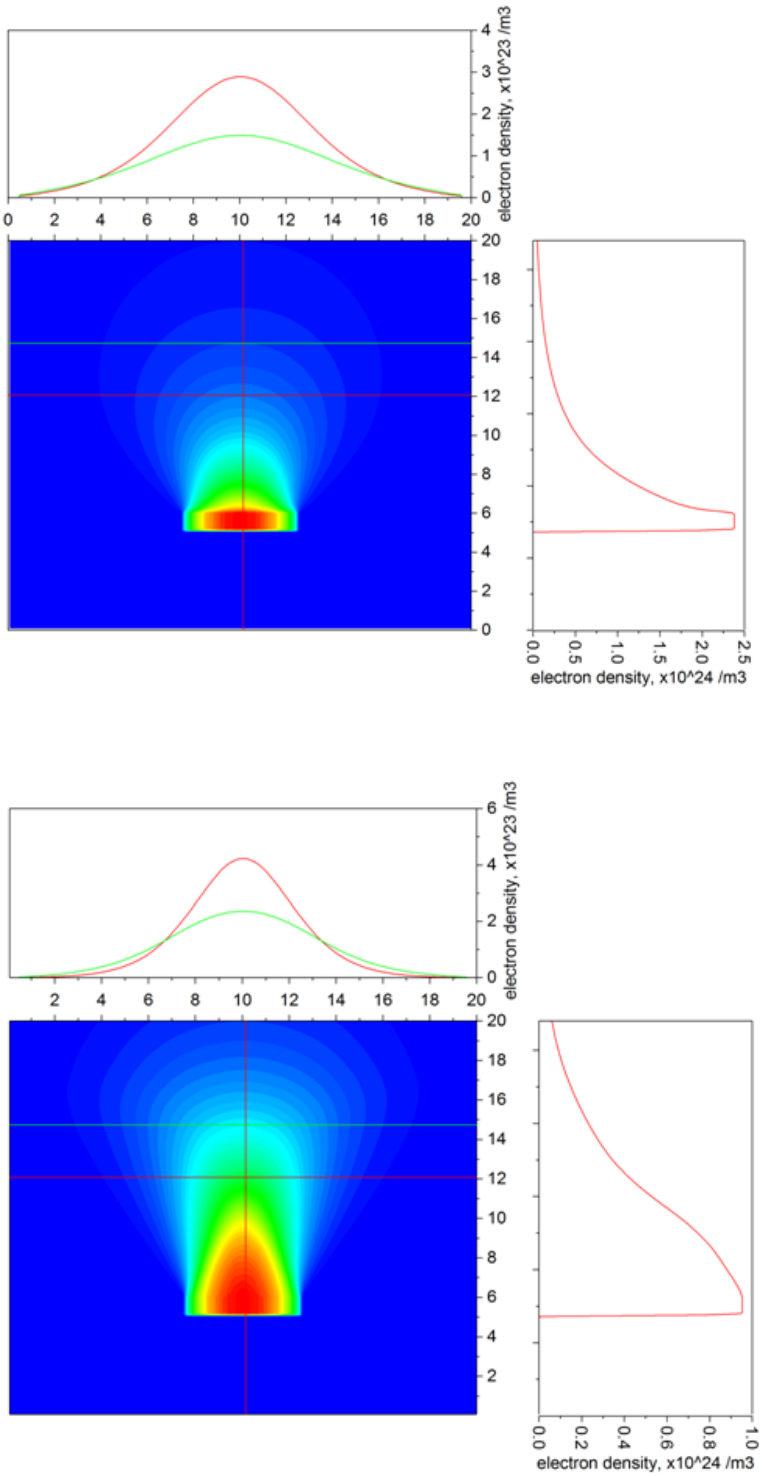

Figure 5.6: Varying the temperature of the plasma affects its divergence angle. The upper plot is a 10 eV plasma, the lower one is 2 eV. (Other parameters are equal, gun_rho= $2x10^{-4}$, gun_v=$2x10^{4}$ m/s, dimensions are mm).

Comparing densities in simulations, the axial density profile peaks at a much higher value at the nozzle and decreases much more quickly away from the nozzle in the higher temperature simulation. The divergence of the plasma can be better understood by choosing a density contour and setting the colour map of the plot to show only above it. Figure 5.7 shows the plots from above recoloured to emphasise the 10^{21} /m^3 profile line, less dense regions are coloured black. The higher peak and more rapid decrease away from the nozzle are explained by the fact that the hotter plasma will have a greater pressure gradient and it could start to dominate the nature of the plasma.

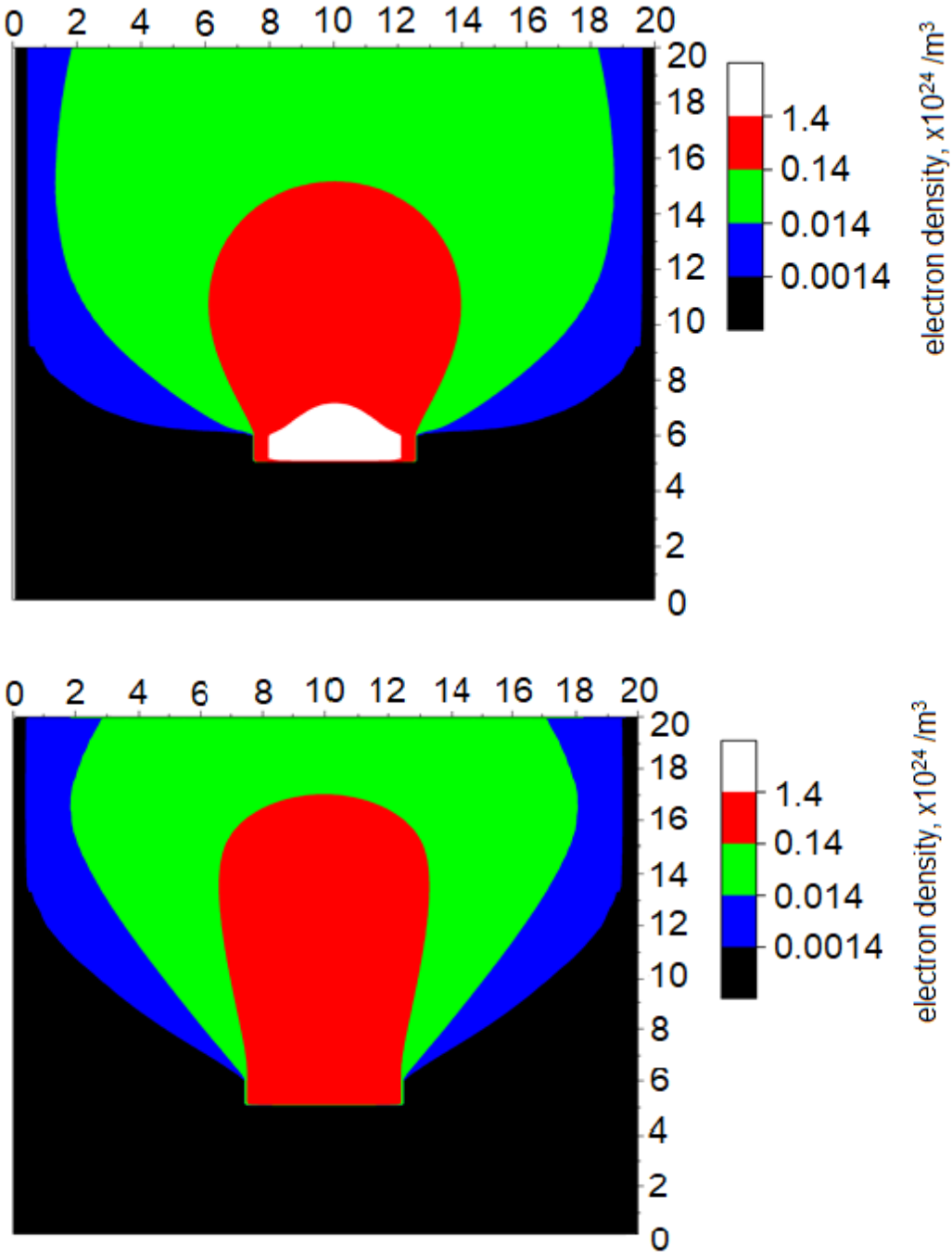

Figure 5.7: Showing plasma densities above the 10^{21} /m^3 contour shows clearly how the divergence angle varies with plasma temperature (Top = 10 eV, bottom = 2 eV). The contour density was chosen for this figure as it clearly illustrates the varying divergence (dimensions are mm)

After many comparisons, the values for the plasma source used to mimic the gun were determined to be gun_T = 4 eV, gun_rho = $2\text{x}10^{-4}$ kg/cc and gun_v = $2\text{x}10^{4}$ m/s for the plasma generated at a typical driver pulse of 21 kV. Figure 5.9 shows a comparison between the simulated and measured density profiles.

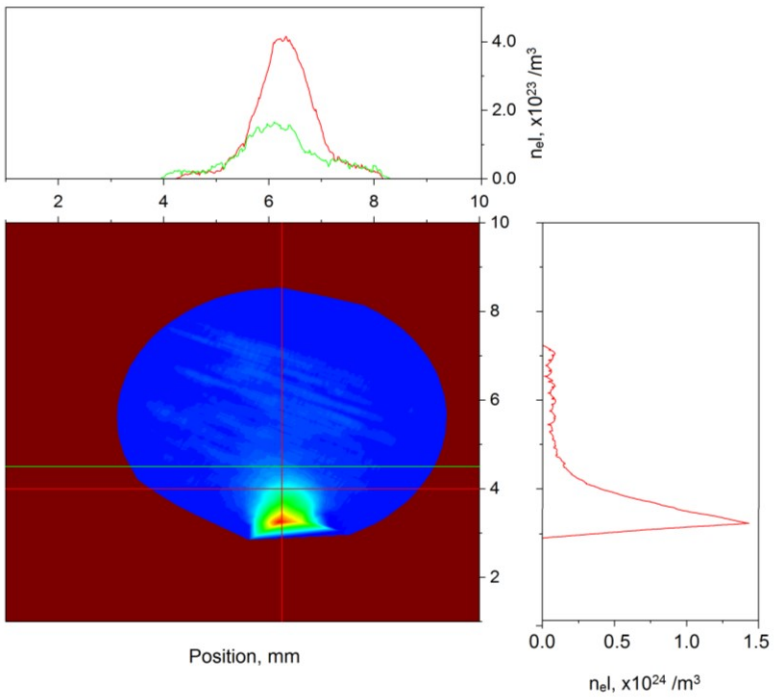

Figure 5.8: Extracting experimental data for comparison with simulation results.

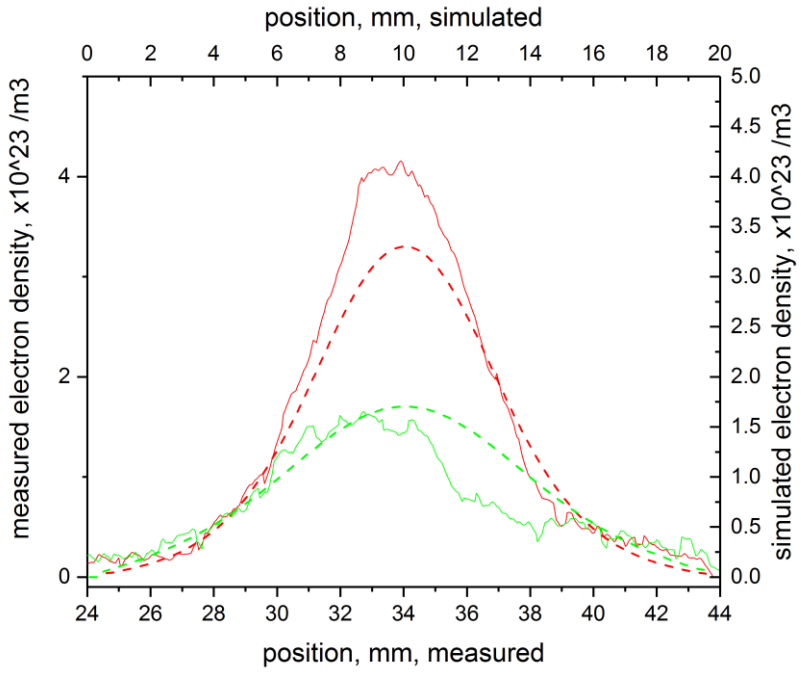

Figure 5.9: comparison of an 18 kV shot data with simulated data, the data shown is for an 18 kV shot (solid lines), compared with data from a Te=4 eV, gun_v=2x10^4m/s, gun_rho=2x10^{-4} kg/cc simulation (dashed lines). Lineouts taken at 5.9 mm (red) and 8.6 mm (green).

With these parameter values, the speed of the plasma expansion in the simulations can be estimated as 7.5x10^3 m/s is a little slower than measured but increasing the injection velocity any

further affects the divergence greatly. The plasma expansion front velocity only matters insofar that the density at the rod is correct at the onset of the current pulse, and so the pulse can be applied a little later in time in order to account for this. At high voltages, 21 kV the difference in density between simulation and experiments becomes more pronounced but is well within a reasonable range (see figure 5.9). The results shown here are not exact matches but are well within a reasonable range. Further work could be undertaken to locate an exact match to the experimental results, but it is felt that this would represent diminishing returns at this point, and so was not undertaken. The proximity of the results is sufficient for the development of the PFRP model. One major difference between the experiment and the simulation is that the plasma creation is continuous in the simulation, whereas it is pulsed in the experiment. In the region of interest, at the times under study this will not affect the behaviour of the snowplough as the density of the pre-fill at the rod at the time the main current pulse starts to flow is what matters.

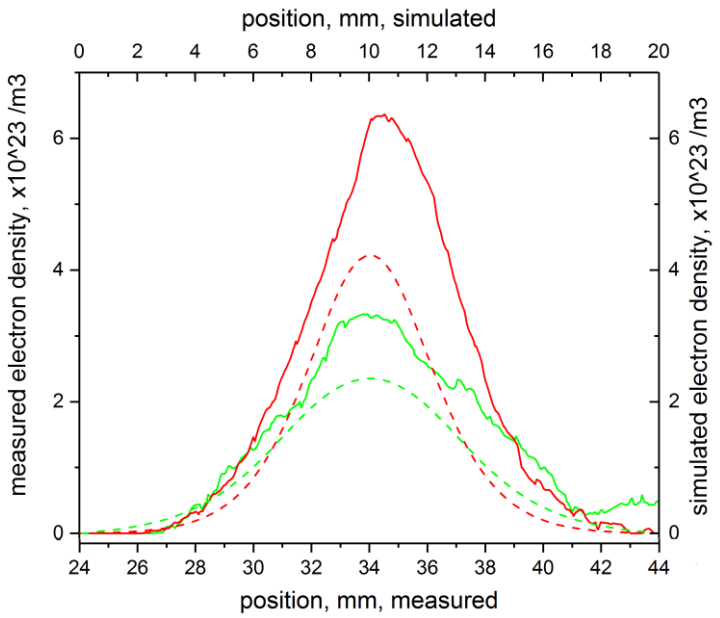

Figure 5.10: Comparing data from a 21 kV shot (solid lines) with a 2 eV plasma simulation (dashed lines). The lower temperature reduces the pressure gradient and increases the forward density profiles as the injection velocity starts to dominate. The profile shapes match well, but the densities in the simulation are a little low. Lineouts taken at 5.9 mm (red) and 8.6 mm (green).

The plasma pre-fill develops over µs timescales, whereas the main current pulse lasts for roughly 100 ns. Modifying the behaviour of the plasma source to a pulsed one could be achieved in future by varying the density output with time.

5.2: Multigun simulation

Once the single gun simulation parameters were found, it was possible to construct an initial model with six guns contributing to a pre-fill around a central anode rod and cathode disk.

The convergence of the multiple plasma guns showed similar behaviour to that seen in the experimental data. There are distinct areas of higher density where the plasma overlap, present in both the experimental results and the simulation data. Simulations show the density ramps up dramatically when the plasma front reaches the centre and the plasma converge, again agreeing with experimental data on this behaviour. Placing the rod off-centre allows the effects of the convergence of the plasma, and the collisionality of the plasma with the rod to be decoupled by taking lineouts in different directions, either including the rod, or not.

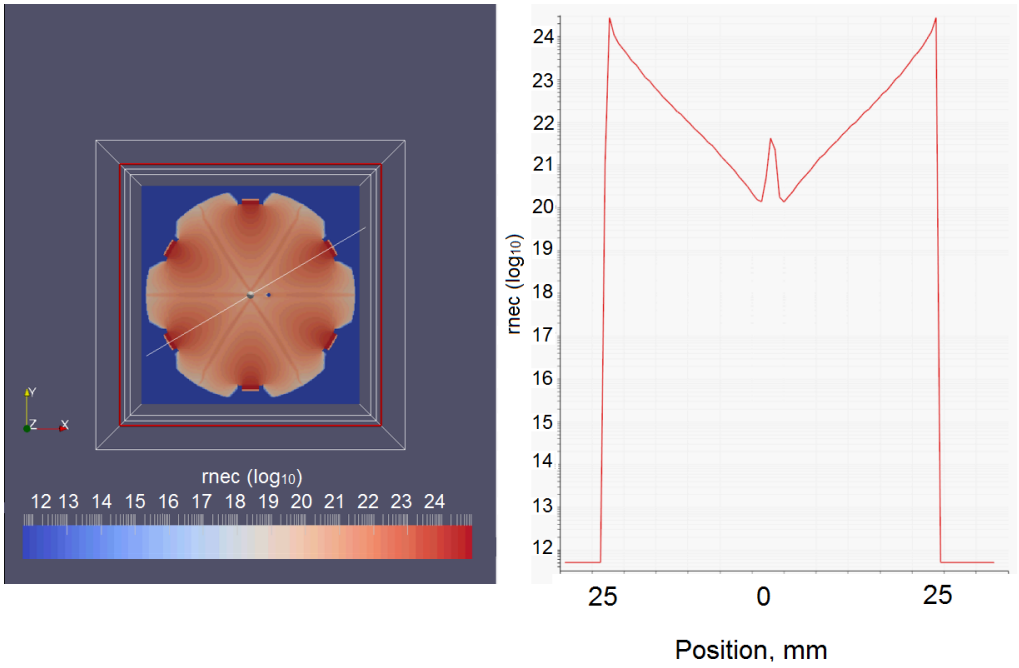

Figure 5.11: Taking a line profile through the centre of the plasma convergence but not through the rod region (rod offset from centre) shows the increase in plasma density at the centre. Rod is 1 mm in diameter, visible as small blue dot).

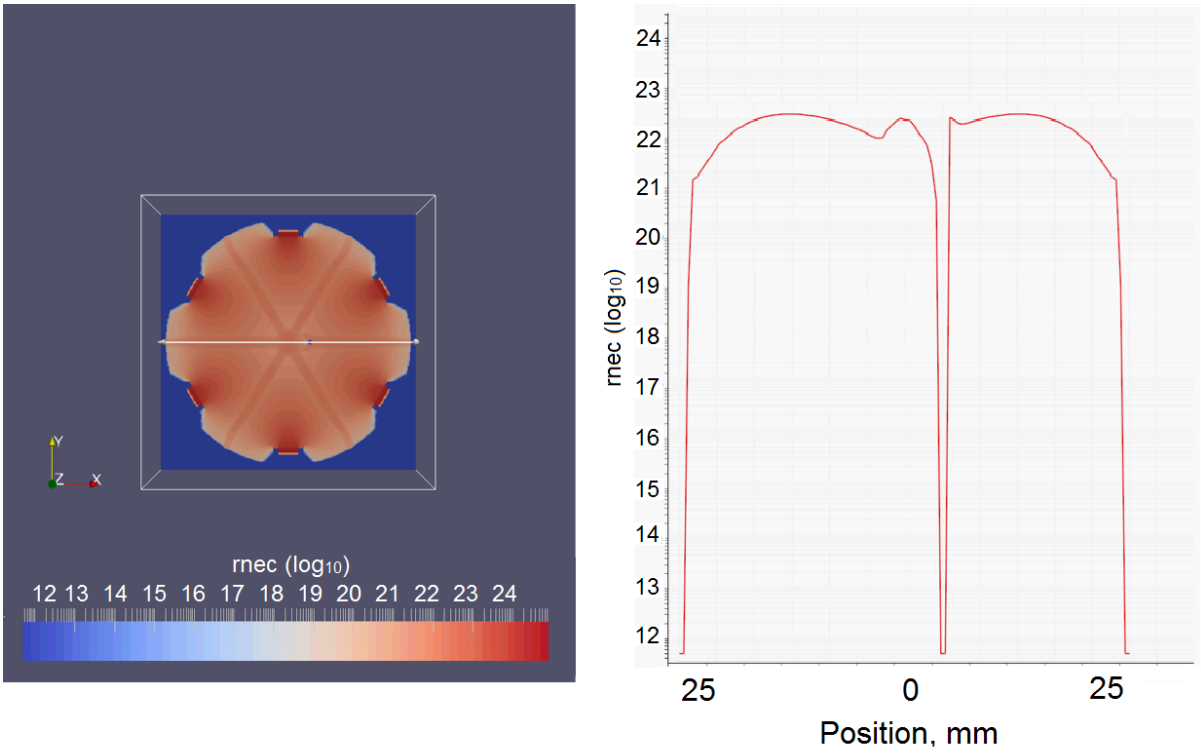

Figure 5.12: A line out along a region of plasma overlap shows how the density is affected by the presence of the offset rod. Upstream of the rod the profile shows a density increase, and downstream the density is lower where the rod blocks the flow from the plasma (the region with zero density is where the rod is).

Experimentally acquiring an interferogram with similar geometry (the rod being off-centre) enables the behaviour of the simulation to be checked. The interferogram shows both the region around the rod having higher density and the region at the nominal centre of the plasma convergence zone. The low density region at the left of the rod is due to the fringes having poor contrast at this point due to the rod support.

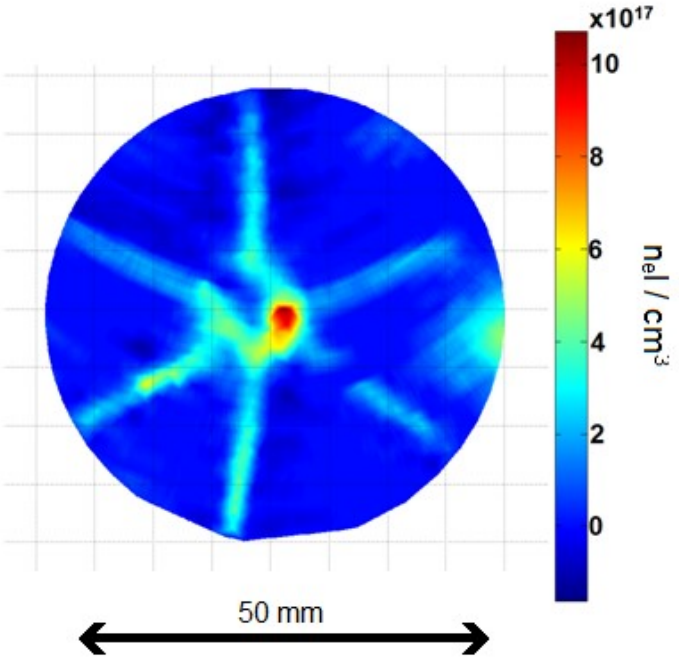

Figure 5.13: The multigun interferogram, figure 3.23, illustrates the correct formation of the plasma convergence zones and the increased density at the offset rod.

5.3: Simulations of the snowplough phase

Once an adequate simulation of the plasma flow from the guns onto the rod was developed, it was used as the basis for a full 3D MHD simulation of the movement of plasma along the rod in response to the main current flowing. In order to enable these simulations to complete more quickly, checks were performed on the initial model to understand the effects of reducing the resolution of the computation grid. Halving the resolution in each axis reduces the computational load by a factor of eight, or sixteen if temporal resolution is reduced too. High resolution simulations were compared with lower resolution, and no major differences were noted. Perturbations in the current sheath are observed in both high and low resolution simulations, and they evolve similarly. This finding led to the use of lower resolution simulations, at 270 cells per side.

The same gun parameter values as before were employed, and the simulation applied a magnetic field to the region at the base of the rod, such that it induced a current of 650 kA in 75 ns. No field is applied in the region above the cathode.

Figures 5.14 to 5.16 show the motion of the pre-fill in the simulation. In the simulations, the plasma is seen to snowplough along the rod, taking 30 ns to travel the length of it. This equates to a velocity of 8×10^5 m/s, comparable to estimates of the Alfvén velocity (6×10^5 m/s), expected for non-Hall regime behaviour according to [5.2].

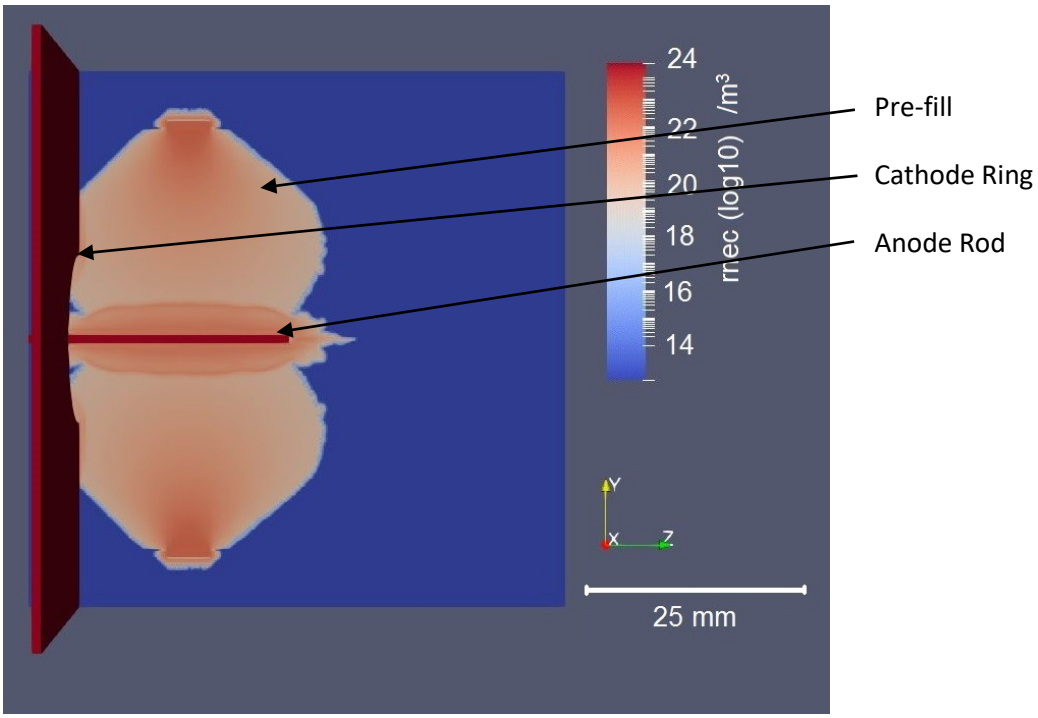

Figure 5.14: 10 ns after the current starts to flow, the snowplough hasn't yet presented itself.

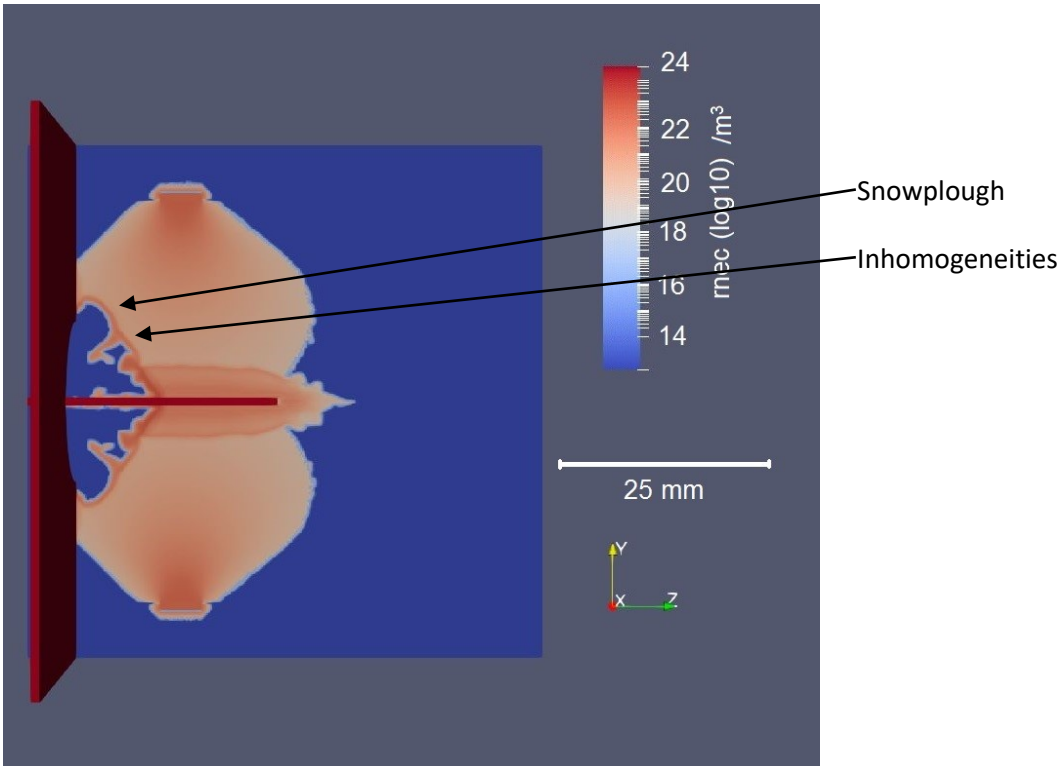

Figure 5.15: 35 ns after current starts to flow, the snowplough has progressed a distance of approximately 10 mm along the rod. Some inhomogenities can be noted inside the snowplough, caused by a slight variation in the density. It is thought that the variations are caused by the edge of the plasma which has propagated through the hole in the cathode ring.

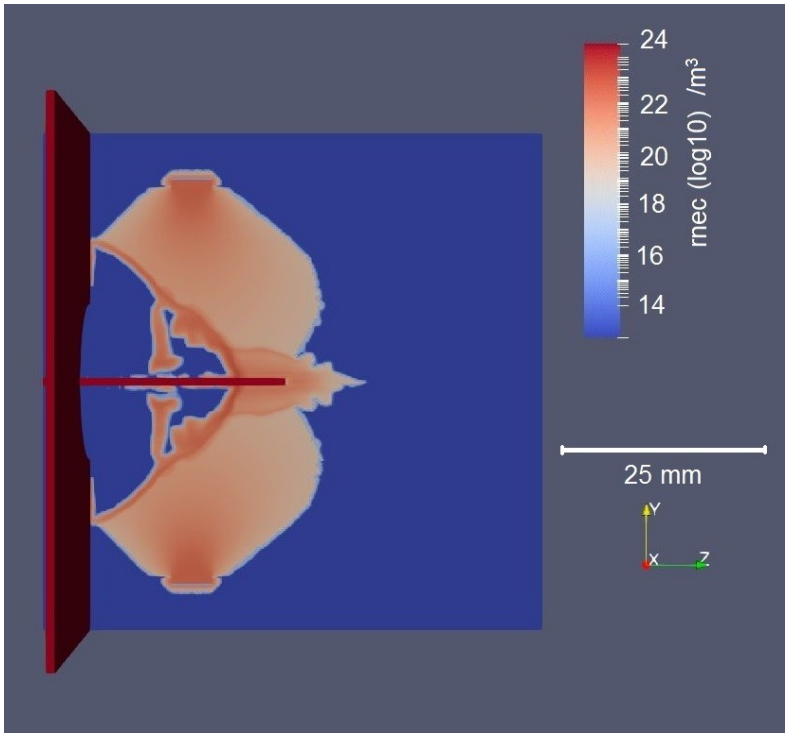

Figure 5.16: At 45 ns, the snowplough shows marked density increase of two orders of magnitude at the current sheath. The inhomogeneities have developed further to form a conductive path, a secondary snowplough front.

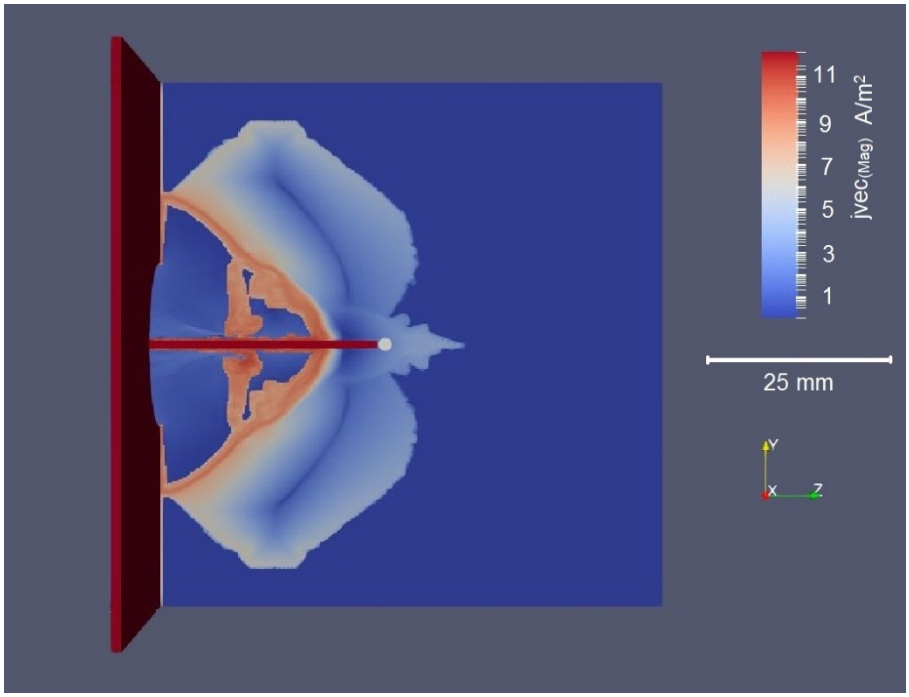

Figure 5.17: The current flow can be seen to be roughly equal in both snowplough fronts.

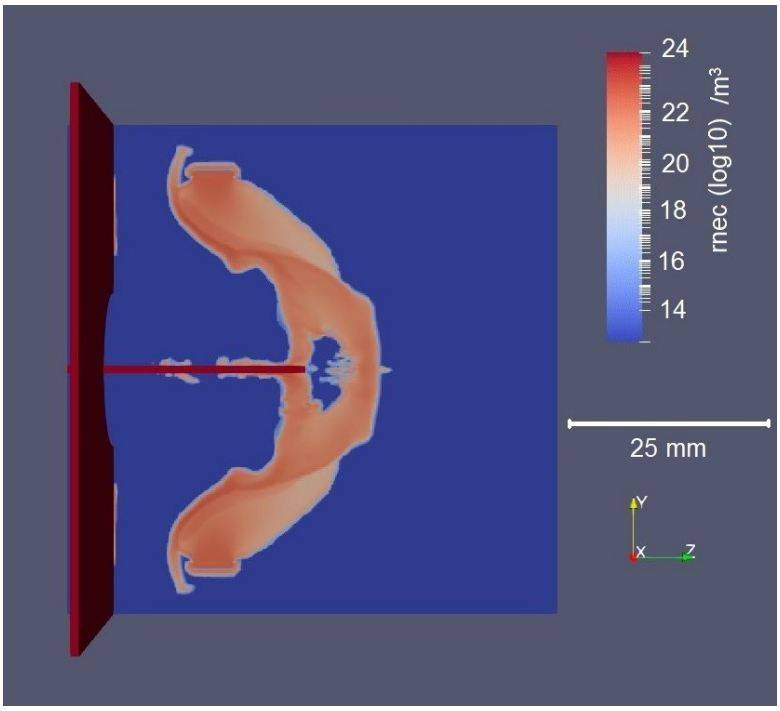

Figure 5.18: At 60 ns, the secondary snowplough has almost merged with the main one.

Figures 5.14 to 5.18 show how the snowplough propagates along the rod. The time at which the snowplough leaves the rod also compares well to experimental measurements in [5.1], in the region of 50 – 70 ns. A precise timing is not possible as the intensity of light emitted by the source will

overwhelm any optical diagnostic. Timing can be inferred however, by studying the change in impedance of the diode as it increases when the acceleration gap opens.

In the simulations, a secondary snowplough can be seen, possibly seeded by the edge of the plasma that has made its way through the hole in the cathode ring, giving rise to magnetic Raleigh-Taylor instabilities, or the cause could be within the simulation only, for example, numerical instabilities. By studying the distribution of current flow, it is possible to understand how this secondary front may affect the current passing through the tip of the rod. As figure 5.18 above shows, the current density is roughly equal in both snowplough fronts. Investigations into possible cures of the second snowplough yielded an interesting result. Increasing the radius of the hole in the cathode to move the edge away from the pre-fill helps considerably, as shown in figure 5.20. It is interesting to note, however, that the instabilities do still occur, just less prominently, and further from the rod. They never reach the rod and short the current path. This could merit further work once the Hall version of Gorgon is completed.

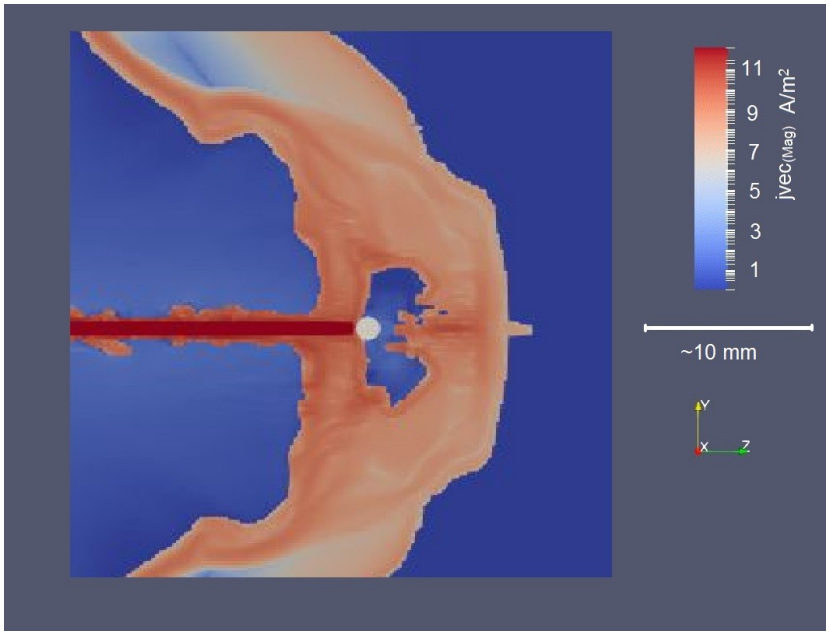

Figure 5.19: The secondary snowplough

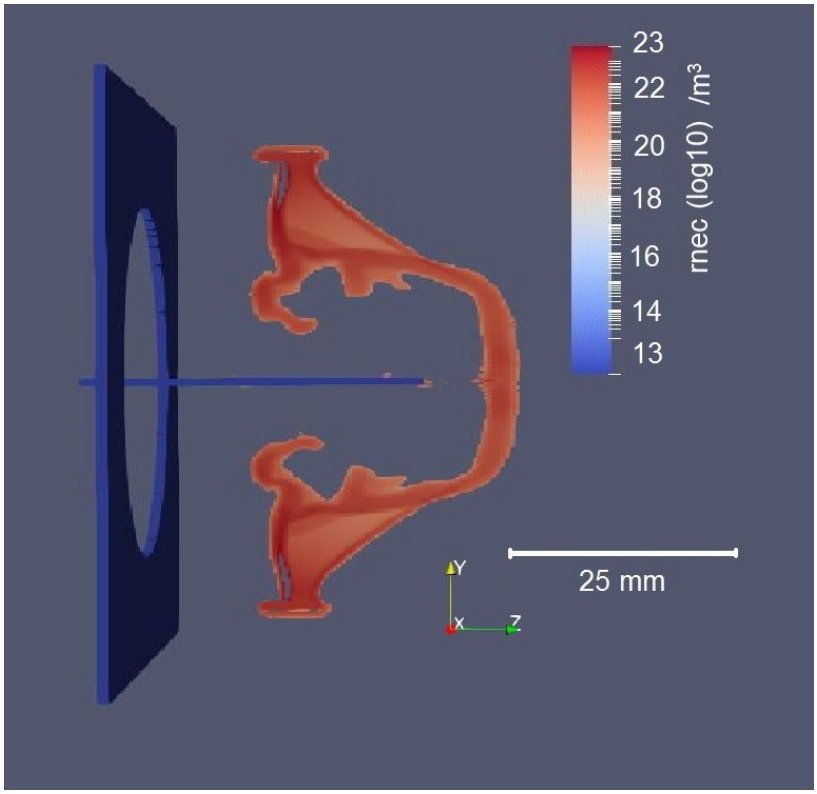

Figure 5.20: A larger cathode hole helps decrease the presence of the second snowplough.

It should be noted at this point that the model is not technically accurate in one respect, due to the method used to induce a current into the rod. The snowplough front actually leaves the cathode, becoming tethered to the plasma guns instead. This would prevent current flow as there's no longer a conductive path between the cathode and anode. This behaviour is understood to arise as a result of the way the magnetic field is applied to the simulation and does not affect the capability of the code to demonstrate the behaviour of the main phase of the snowplough.

5.4: Exploring the operation of the PFRP

5.4.1: Density and the transition to Hall regime

If the pre-fill density is too high, the snowplough may not actually be able to traverse the rod in the duration of the current pulse. If the density is too low, however, the operation could enter the Hall regime, as discussed by [5.2, 5.3, 5.4] who all agree that certain conditions need to be met in order for the Hall regime to dominate;

- A characteristic timescale which is much less than the ion gyrofrequency
- An electron speed which is greater than the Alfvén velocity

One further consideration is that the Hall effect will not dominate if the system is configured in positive polarity [5.5] as the Hall effect advects the magnetic field lines in the direction of the current along contours of radial density [5.6]. [5.3] states that postive polarity configurations will not exhibit Hall regime behaviour, but [5.6] go further to discuss how this is the case only in uniform plasmas. In non-uniform plasmas, the Hall regime can advect the magnetic field into the plasma in both polarities.

In Paraview, it is possible to perform calculations on data and plot the results. (This is achieved using the *Append Attributes* feature). By plotting the results for the different terms in eq. 4.9, the relative magnitudes of the different terms can be ascertained:

$$\frac{\partial \mathbf{B}}{\partial \mathrm{t}} = \nabla \times \left(\frac{\nabla \times \boldsymbol{B}}{\sigma \mu_0}\right) + \nabla \times (\mathbf{v} \times \mathbf{B}) - \nabla \times \left(\frac{\mathbf{j}}{\mathrm{n_e e}} \times \mathbf{B}\right) \quad \text{(Eq. 5.1)}$$

In the above equation, the first term, featuring $\nabla \times \boldsymbol{B}$, concerns resistive diffusion of the magnetic field lines, the second term, featuring **v**x**B**, represents the snowplough, the third term, featuring **j**x**B**, is the Hall term. Note that although Gorgon does not presently simulate the Hall effect, the quantities involved are calculated and so the Hall term can be plotted for any point in the simulation time, it is simply that the Hall term does not affect the evolution of the simulation. The plots of each term are shown in figures 5.21 and 5.22.

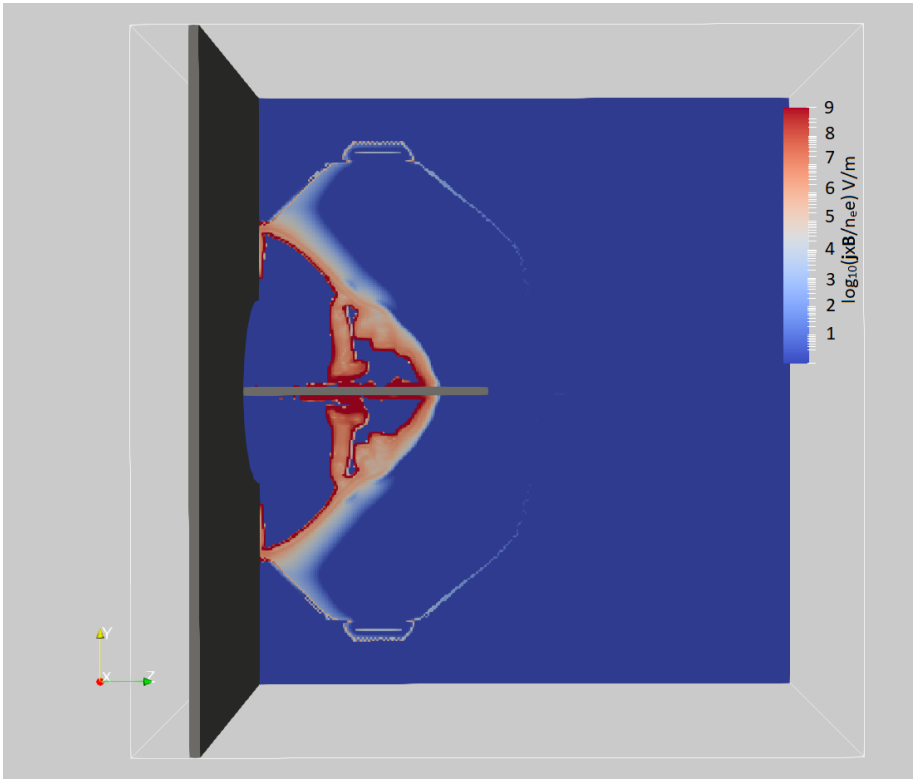

Figure 5.21: Hall term plotted, T=45 ns.

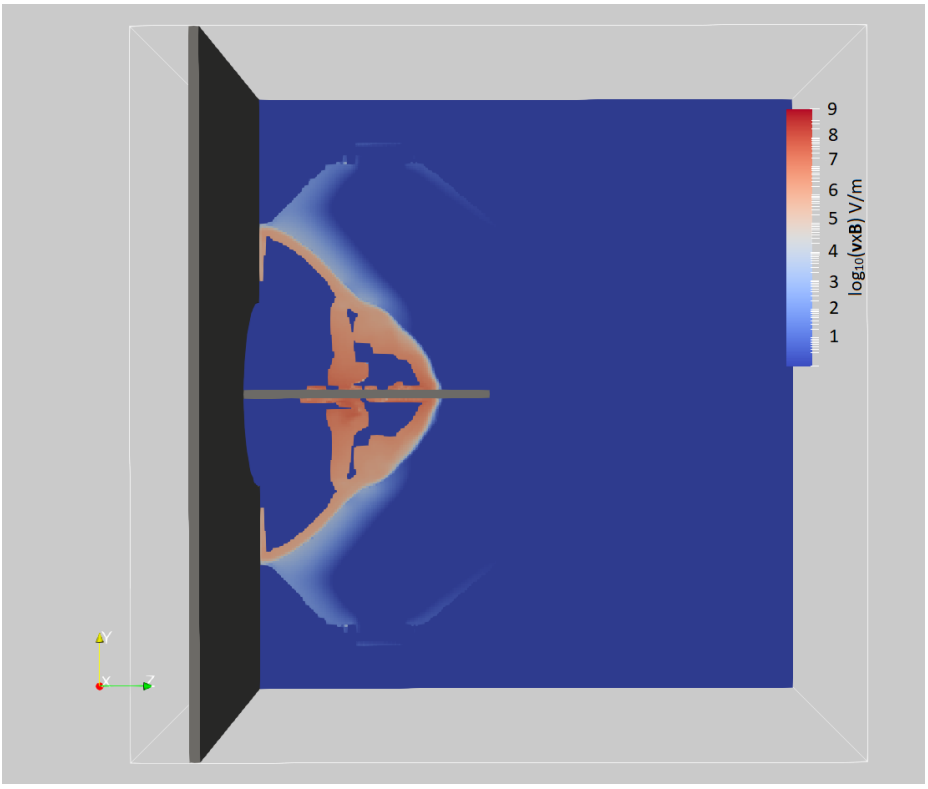

Figure 5.22: Snowplough-related term plotted, T=45 ns.

The **jxB** term plot shows higher, though comparable values at the edges of the plasma than the **v**x**B** term plot, though inside the plasma the values are similar. Although the Hall related **j**x**B** term is similar to, but greater than, the snowplough related **v**x**B** term, it is still the snowplough mode that dominates as the current rise time is greater than the ion cyclotron period, given by $\omega_i=eB/m_i$, which is in the order of ns, a comparison used to discern the dominant regime by [5.3].

5.4.2: The effects of variations in pre-fill density

Variations in the density of the pre-fill lead to dramatic changes in the shape of the snowplough, as shown in figure 5.23 where the plasma density was configured to be 10x denser than the standard. The flattening of the snowplough's profile would lead to increased inductance which could affect the accelerating voltage as well as the current rise time, both of which would affect the x-ray dose obtained. As a denser pre-fill is also heavier, the time taken to traverse the rod would also be expected to increase with density, but this was not evident with a density ten times greater than the nominal values used, though a pre-fill that is too dense could lead to the current pulse ending before the snowplough has reached the end. Possible causes for this discrepancy could be the current is shared between the two snowploughs in the nominal density case, so each particle will be propelled less strongly, and the denser snowplough has a distinctly different shape which may lead to material being propelled radially, leading to decreased density on axis.

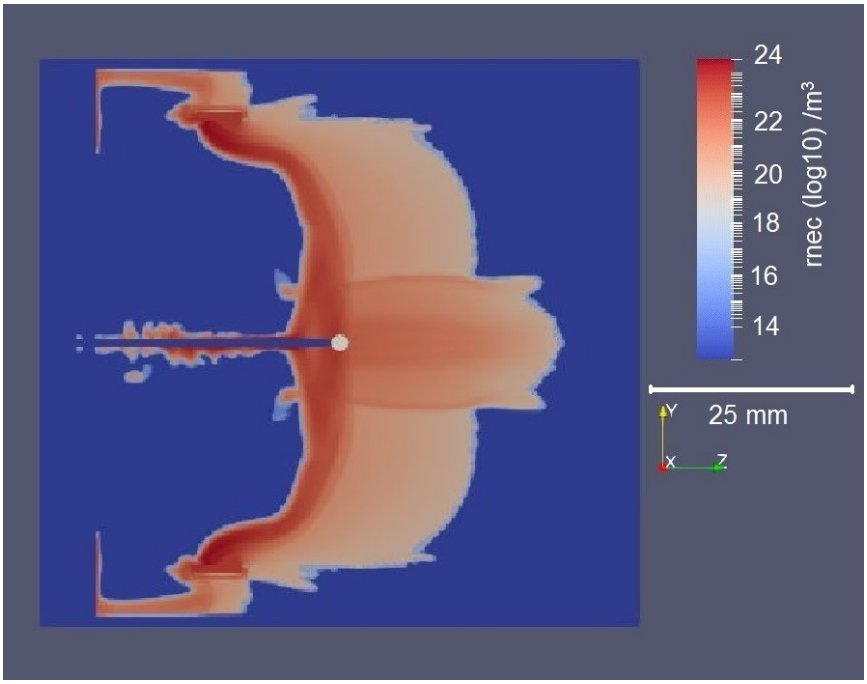

Figure 5.23: Increasing the pre-fill density (gun_rho=2x10-3 kg/cc, x10 increase over nominal value) causes changes to the profile of the snowplough.

5.4.3: Examining the effects of off-centre rods and asymmetric pre-fills

Plasma pre-fill density is not the only important factor to understand. Alignment of the rod with the cathode, and symmetry of the pre-fill may also affect the operation. It was observed in the experimental phase of this study that the pre-fill symmetry can be affected by gun placement or failure.

The simulation was modified to place the rod significantly off-centre, until it was almost at the edge of the hole in the cathode ring. The results show that, although the snowplough is deformed, and features some filamentation, it still forms, and maintains a conductive path between the cathode and anode until about 45 ns. From a plasma perspective, the snowplough operation appears to function, although it is off-axis, following the displacement of the rod. It doesn't break free of the rod as cleanly as a "properly formed" snowplough, which could cause a prolonged low-impedance phase, decreasing the x-rays produced by preventing the a-k gap from opening fully and cleanly at the correct time in the pulse.

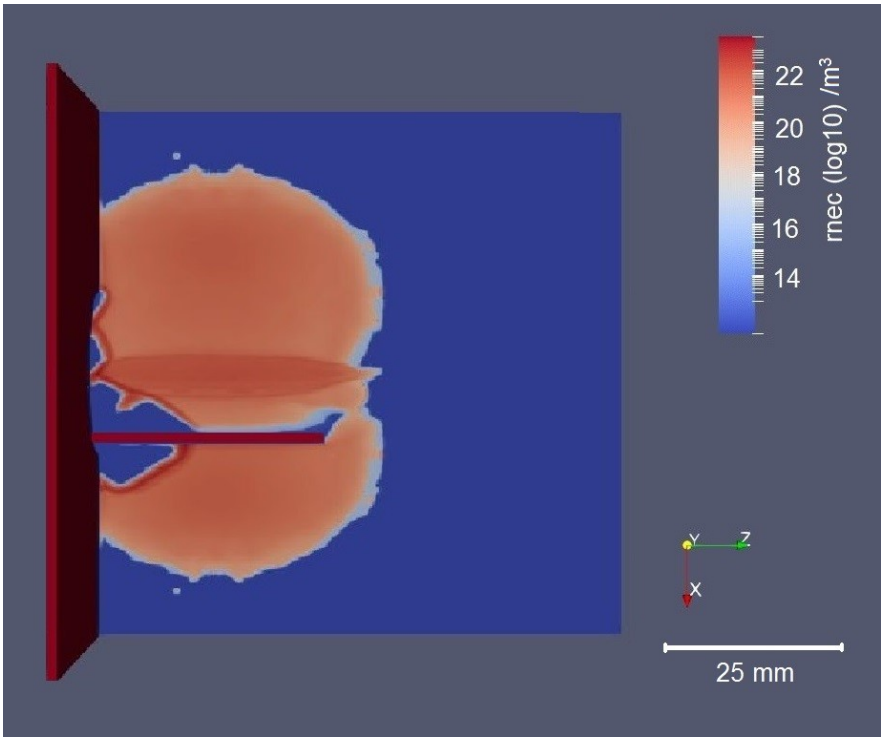

Figure 5.24: The onset of a malformed snowplough in a configuration with an offset rod.

A failed plasma gun was simulated by simply disabling one of the sources, leading to an asymmetric pre-fill. The simulated pre-fill, shown in figure 5.25, bears a strong likeness to the measured density distribution acquired during the experimental phase, when a gun failed to fire. The interferometry showed five regions of overlap, rather than the usual six, with the central convergence region being deformed towards the non-firing gun. Simulations of multiple plasma converging asymmetrically due to five guns firing, show that the effect on the convergence pattern is solely restricted to the regions where the overlap would occur. There is no global impact on the convergence of the other plasma.

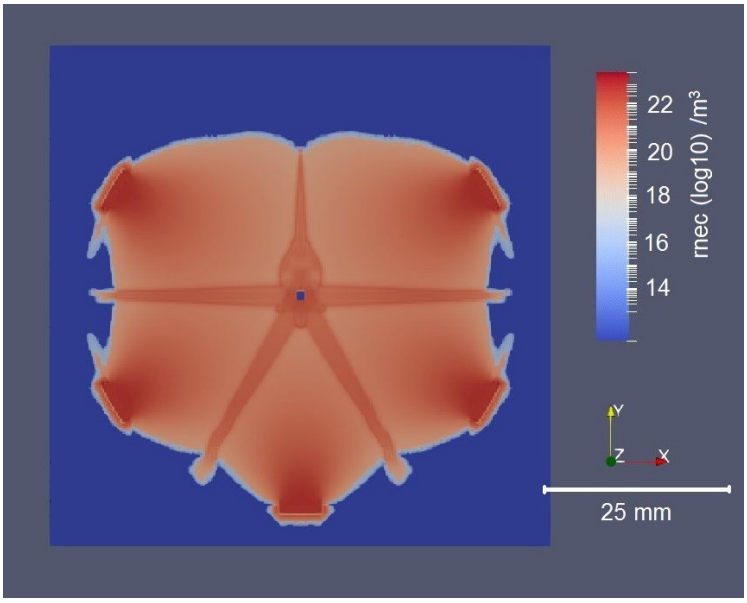

Figure 5.25: Simulated asymmetric pre-fill.

On application of the main driving current pulse, the behaviour of the asymmetric pre-fill is surprisingly similar to that of the symmetric pre-fill, with a snowplough heading towards the end of the rod. The amount of plasma in the current sheath is less than for a complete pre-fill, as it misses a segment once the snowplough starts to transit the rod. The transit time for this snowplough is 10 ns shorter than that of the first snowplough in the baseline configuration.

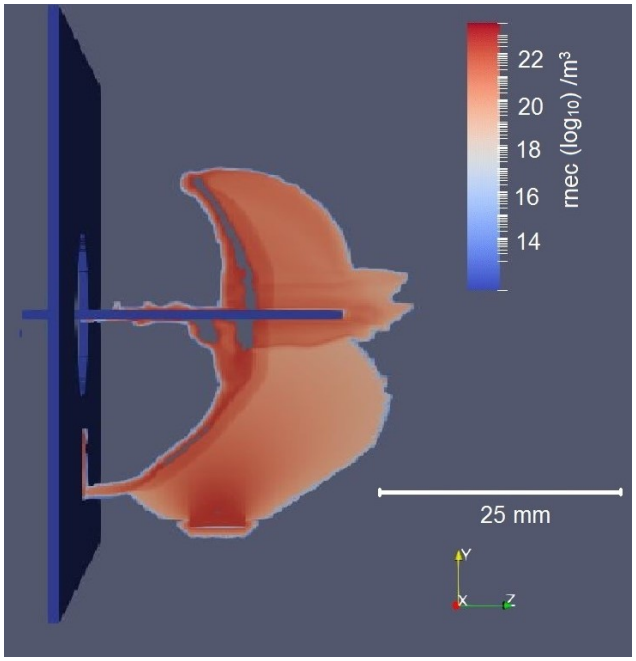

Figure 5.26: a side view of the snowplough shows correct operation, despite being improperly formed.

These results show the resilience of the PFRP to geometrical issues. Increasing the rise time of the current pulse, meanwhile, leads to an increase in the time taken for the snowplough to travel along the rod. In the simulation, the rise time was increased to reach a peak at 200 ns, instead of 75 ns. The first snowplough left the rod at 70 ns, instead of 50 ns, and the second left at 90 ns instead of 60 ns, although the pre-fill is broken up by this time. The higher impedance arising from the pre-fill being cleared out by the snowplough would likely reduce the current and so decrease the x-ray dose from the diode, though the voltage across the diode would remain high for a prolonged period, potentially causing hardware failure.

If the peak current is decreased from 650 kA to 250 kA, similar behaviour is evident, 60 ns and 80 ns for the first and second snowploughs respectively. This is not surprising as both situations decrease the current passing through the snowplough and decrease the force propelling the snowplough.

In summary, these simulations have shown that the PFRP should be resilient to minor variations in configuration, such as only five plasma guns firing, or the timing of the main current pulse changing slightly, leading to variations in plasma pre-fill density. Even if the main current pulse contains less than half of the current of the standard one, the snowplough should still occur, and the acceleration gap should still open. A slight misalignment should not prevent the operation of the PFRP either, although operating at the severe misalignment simulated here would certainly not be recommended. Without analysing the interactions of the electrons with the rod using Monte-Carlo methods, for example, it is not possible to fully gauge the effect these changes would have on the x-rays produced.

Chapter 6: Summary, conclusion and future work

6.1: Summary of key results

In this thesis, the behaviour of the plasma filled rod pinch was studied, first measuring the characteristics of the plasma pre-fill generated by the plasma guns then using these measurements as the basis of 3D MHD simulations of the entire diode.

Measurements from a single gun demonstrated that the plasma expands with a velocity of $8.5x10^3$-$14.5x10^3$ m/s, and has a density of 10^{18} cm^3 at the nozzle, which decreases rapidly away from the gun. 12 frame high speed interferometry was developed to understand the nature of the plasma density distribution and how it evolves over time. This technique proved more powerful than existing methods because a single shot's evolution was studied at multiple instances during the one shot, rather than the more conventional method of taking multiple shots and making the assumption that the evolution is the same each shot. The divergence of the plasma, and the velocity of the expansion front were the main characteristics used to compare the experimental and simulated plasma, along with the density profile.

Spectroscopy was used to obtain estimates of the electron temperature as 2-2.8 eV through coarse comparison with simulated emission spectra using Prismspect. This rough estimate was within an order of magnitude of the Thomson scattering experiments, which gave a result of 9 eV. The discrepancy could be explained by the fact that probed volume was slightly different.

Multiple guns were used to investigate the convergence of the output plasma and understand the collisionality of the plasma, further refining the simulation. The plasma convergence was seen to increase in density in the areas of plasma overlap, and also at the centre of the convergence. Ordinarily, the density distribution had a six-fold rotational symmetry (when viewed perpendicular to the plane of the plasma guns), exhibiting "arms" where the plasma overlap. When a gun failed to fire, or was not correctly aligned, the arrangement of the arms changed to reflect the absence of the plasma.

In the simulations using the Gorgon 3D MHD code, the plasma gun was modelled as a simple expanding plasma source, rather than modelling the processes that lead to the plasma being created in the nozzle of the plasma gun. The plasma was described by several parameters (density, temperature and injection velocity) which were determined by matching the simulated plasma with results from experiments.

Once the pre-fill had been successfully simulated, the action of the main current pulse on the diode was explored in the simulations. As the current increased, the pre-fill was swept along the rod in a snowplough, similar to the run-down phase of a dense plasma focus. When the default current pulse, which rises to 650 kA in 75 ns, flows in a nominal density pre-fill, the snowplough travels the length of the rod at $8x10^5$ m/s, comparable to estimates of the Alfvén velocity, expected for the snowplough regime. The speed of the snowplough decreased when a lower current (250 kA) was used, the time to traverse the rod increased to 60 ns. Increasing the risetime also slows down the snowplough. In both of these cases, the snowplough behaviour remains evident.

The strength of the different terms in the MHD equation were compared to experimental and simulation values. Although the Hall term did exhibit relatively large values, it did so typically at very small scales. The effects of pre-fill density were explored - a denser pre-fill exhibits a different profile, it is much flatter. This would occur if for instance, the plasma guns operated at a higher current prior to the main current pulse. The increased volume enclosed by the current sheath would increase the inductance of the diode and could drive down the accelerating voltage or decrease the current.

Other explorations looked at the scenario when the rod is misaligned and is far from central to the cathode hole. Once more, the snowplough is present, but malformed. The deformation occurs because the balance of force and mass discussed above is severely asymmetric and doesn't leave the rod as cleanly as the nominal case. This could lead to a prolonged low impedance phase.

6.2: Conclusion

This study has yielded tantalising results showing how the snowplough phase of the PFRP operation may be affected by variations from the standard configuration. Different variations were simulated and the simulations showed that the snowplough is very resilient. In all cases, snowplough behaviour was observed.

6.3: Future work

This result alone is not enough to assure the successful operation of the PFRP though, as the evolution of the magnetic field is also governed by a competing term, the Hall term, which describes how the magnetic field penetrates into the plasma, rather than pushing it. This could lead to current channels within the plasma and prevent the snowplough from clearing the plasma and creating an accelerating gap at the end of the rod. Neither is this study capable of simulating the e-beam and subsequent x-ray production following the snowplough travelling off the end of the rod.

Extending this study with future work can be split into three main interrelated areas; improving diagnostics of the plasma pre-fill, better understanding of the pre-fill behaviour under the influence of the current pulse and comparison of simulations with experiments on real pulsed power experiments.

6.3.1: Diagnostics

The 12-frame high-speed camera represents a great way of capturing the evolution of plasma over timescales ranging from a few tens of nanoseconds to a few microseconds but manual analysis of the fringe patterns gained from each image is tedious, an obvious improvement would be the implementation of automated extraction of the fringes. Such software already exists but was not capable of analysing the fringe patterns obtained here, as the fringes exhibited too great a curvature. The extreme nature of the curvature could be due to slight misalignment of the optical paths or could be due to the significant increase in beam diameter as it exists the fibre before it is subsequently collimated giving rise to different path lengths arising across the beam width. Understanding the root cause of the curvature would be beneficial as the fibre techniques used to

transport the beam to the experiment could prove very useful in future experiments. If it is very difficult, or expensive to correct the fringe pattern, developing the software so that it can process the curved fringes might be a more realistic option.

The fibre-based triature interferometry is also extremely useful, being quick and relatively easy to deploy. As a diagnostic for use in studies of plasmas, the data it provides is, however incomplete. A single wavelength only provides information on the combined effects of the electrons and the neutrals. Adding a second wavelength removes this ambiguity. Significant efforts were made in this study to develop the two-wavelength version of the triature interferometer. The results showing negative densities, obtained using the Drude model / Gladstone-Dale constant approach discussed in chapter 2, are clearly unphysical, it would be very useful to complete the development of the two-wavelength version in order to understand what is occurring in this region. The problem does not seem to be a deficiency in the fibre optic technologies used, but rather in the analysis used, as the artefacts are evident in data obtained with a conventional open beam, single exposure spatial system. Possible causes for this include transition lines or ion polarisability. Smoothing the data does not solve the issue, so it is not simply caused by the ratio of two low value but noisy signals. Further work is required to obtain understanding of this method, and the range of plasma parameters it can be applied to. The alternate analysis method, based on species polarisabilities (also discussed in chapter 2) shows good promise in this application, though further work is required to improve the confidence in the results, and to understand the small n_0, compared to the Saha prediction. The term $\alpha 0$, the polarisability of the neutral gas, needs particular focus. The term used is specific to Carbon, yet the plasma under study also features Fluorine and Copper. These are not yet accounted for in the calculations presented in this study.

The data from the emission spectroscopy is not conducive to more detailed analysis, it would be desirable to obtain better data with finer resolution. The Thomson scattering technique was very useful at narrowing the range of values characterising the plasma. It would be an excellent extension

of this work to study the plasma at multiple distances from the nozzle, to understand better how the temperature varies. This would support the discrepancy between the spectroscopy and Thomson experiments. Probing the characteristics of the snowplough itself would also be a very interesting experiment, though that would present some significant practical challenges, access to an expensive pulsed power machine and the high x-ray dose being two examples.

Faraday cups could also be used to gain further information of the ion species present in the plasma, as each species would have different times-of-flight, and so the different species could be discerned.

6.3.2: Understanding the effects of the current on the pre-fill

The version of the MHD simulation code used in this study did not have a fully functioning Hall capability. Re-testing the various scenarios simulated here with the new version that features the Hall term calculations could be very instructive and would represent a logical next step. Further testing assertions presented in [6.1] regarding applicability of the different regimes, in the context of the PFRP would be very interesting work. [6.2] states that the Hall behaviour would penetrate into the plasma along lines of radial density variation (nr^2) in a POS operating in positive polarity. Demonstrating this using Gorgon would also be a logical next step. Once the behaviour was understood, another activity could be to push the operating parameters in the simulations and see if, when, and how the PFRP ceases to function.

The plasma was modelled as a continuous source, rather than one that is modulated by the plasma gun driver's current. This is an acceptable approximation in the timescales of the operation of the diode, but a more rigorous improvement would be to modulate the plasma density with a decaying sinusoid.

6.3.3: Experiments on pulsed power machines

It would be a great conclusion to this work if the simulations were improved, and then tested experimentally as thus far only the plasma expansion phase modelling has been tested. Modelling the behaviour of the diode on a real machine would be the perfect way to test the predictions made

by the simulations. A relatively easy experiment would be to take density measurements during the snowplough phase. Other possible experiments could be to integrate the predicted behaviour with other modelling software to obtain a prediction of the x-ray output. This would represent significant efforts though.

Appendix 1 – Lumped LCR circuit simulation

To aid a better understanding of the plasma gun driver circuit behaviour, a simplified model was created to simulate it in software. The circuit was broken down into just three components, a capacitance, a resistance and an inductance.

The capacitance, C, represents just one real-world component, the capacitor.

The resistance, R, needs to encompass the effects of the spark-gap switch, the cables, the plasma discharge and the internal resistance of the capacitor in the doghouse (only one gun was simulated, so only one capacitor was included).

The inductance, L, represents the inductances in the doghouse structure, the cables, the plasma gun, the internal inductance of the capacitor, and any other system inductance, such as that caused by the geometry of the connection of the cables to the gun itself.

Some simplifications are made:

1) That the switch is a simple on-off switch, rather than including the complicated behaviours of a spark gap switch. No time-varying resistances or inductances are included.
2) That the nature of the plasma discharge does not vary and can be modelled as a simple resistance.

These two simplifications are incorrect as reality is more complex, but in the timescale of the pulse, and for the purposes of the simulation (for example: to understand the effect of longer cables, or a cable in the bundle failing open or shorted) they are acceptable in that their absence will not skew the overall result.

The capacitance of the doghouse was known to be 0.7µF. The inductance of the system can be roughly estimated by calculating the inductance of the cable bundle, using the manufacturer's

specifications, likewise resistance. The initial condition is that the capacitor is charged, current starts to flow at the start of the simulation.

Figure App1.1: An LCR circuit.

The simulation of the LCR can then yield current and voltage traces, allowing for comparison with measured data, and a good approximation can be found by further iterations. It is constructive to performs this as it shows how varying the inductance in the circuit can affect both the peak voltage and the frequency of the circuit. Modifying the resistance affects the duration of the damping. Values for L, C and R are roughly 450 nH, 0.7 µF and 0.13 Ω, respectively.

Appendix 2 - Example sequence of images from 12 frame interferometry

Shown here are twelve images captured from the shot shown in Chapter 3, section 3.2.1 in the order they were captured during a shot of a single plasma gun. The frames are 400 ns apart, 10 ns exposure, with the trigger occurring 1.065 µs before the first frame. Multiple flashes can be noted, as the sequence covers the timescale in which the circuit rings, as can be seen by reviewing a typical current trace plotting against an electron density plot.

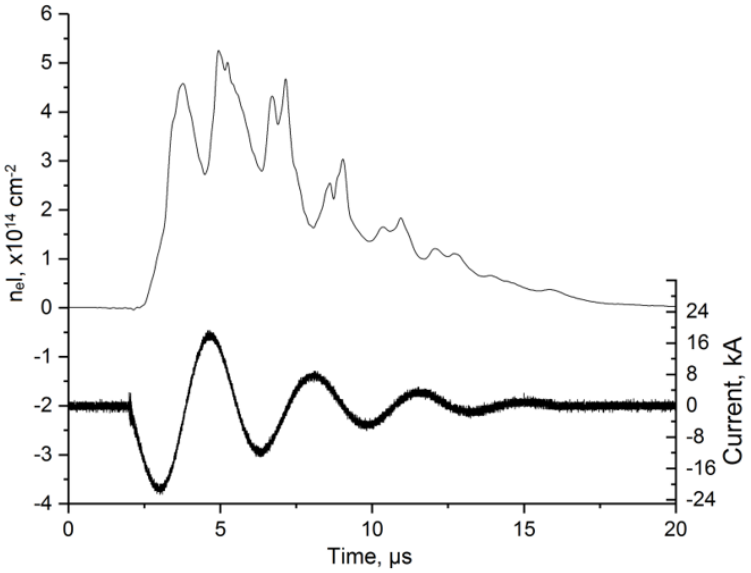

Figure App2.1: Current and electron density.

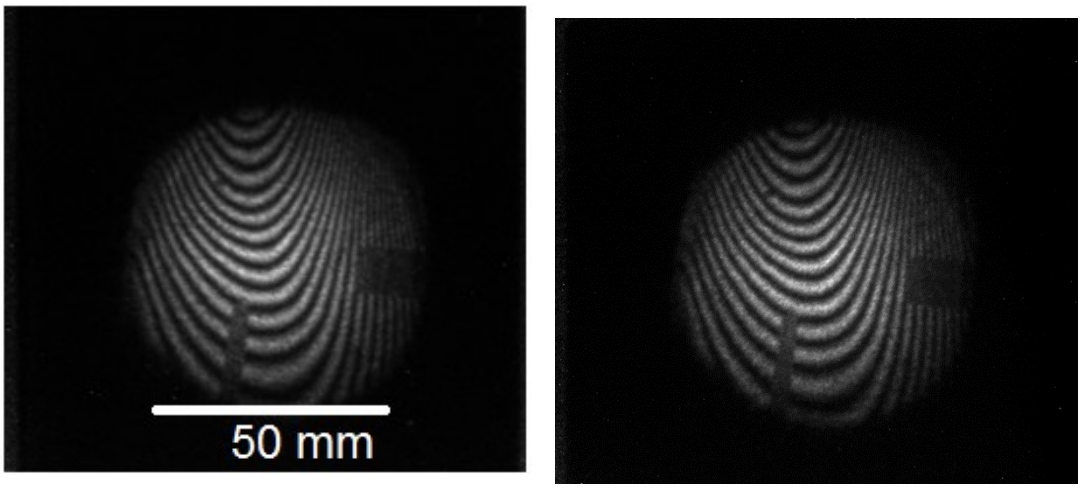

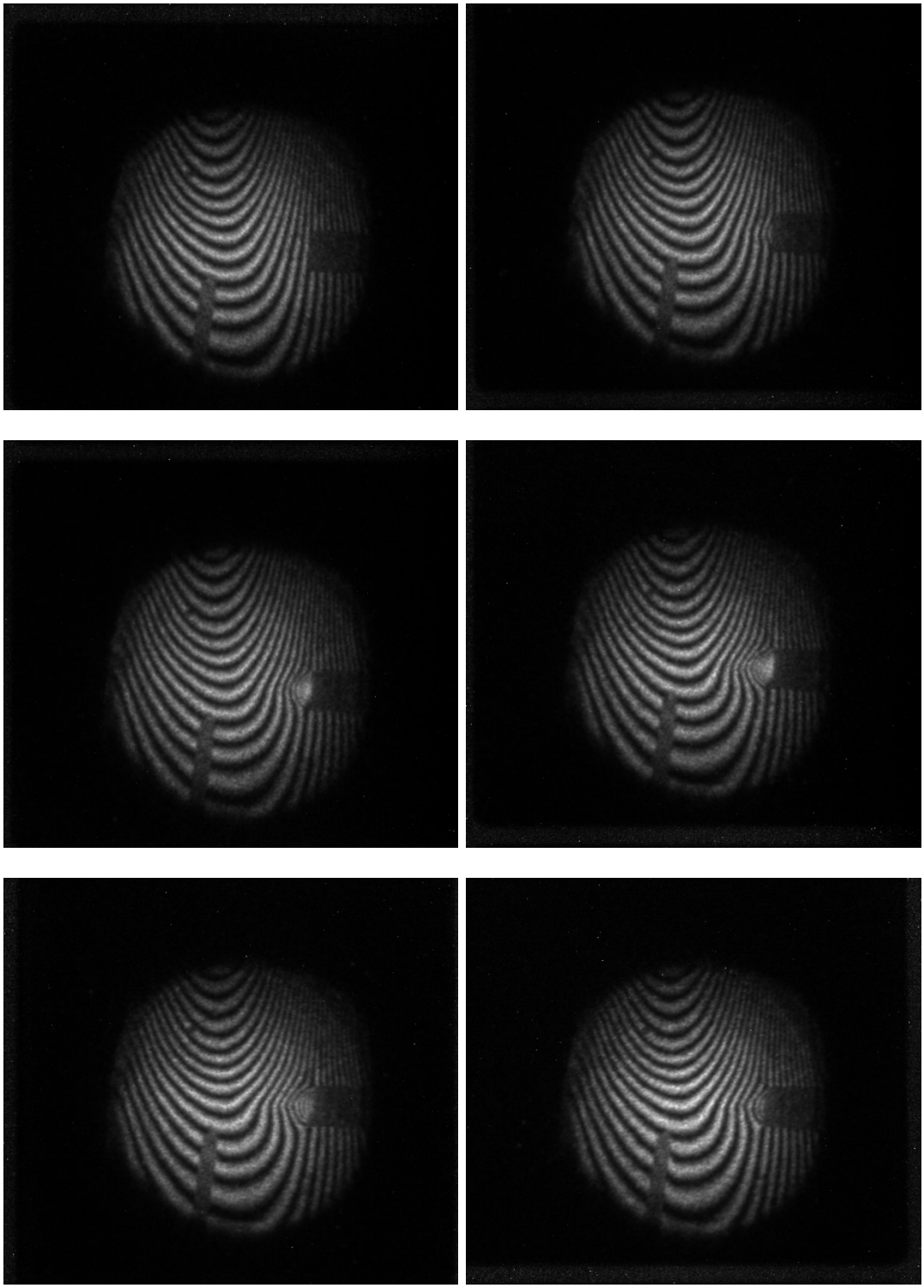

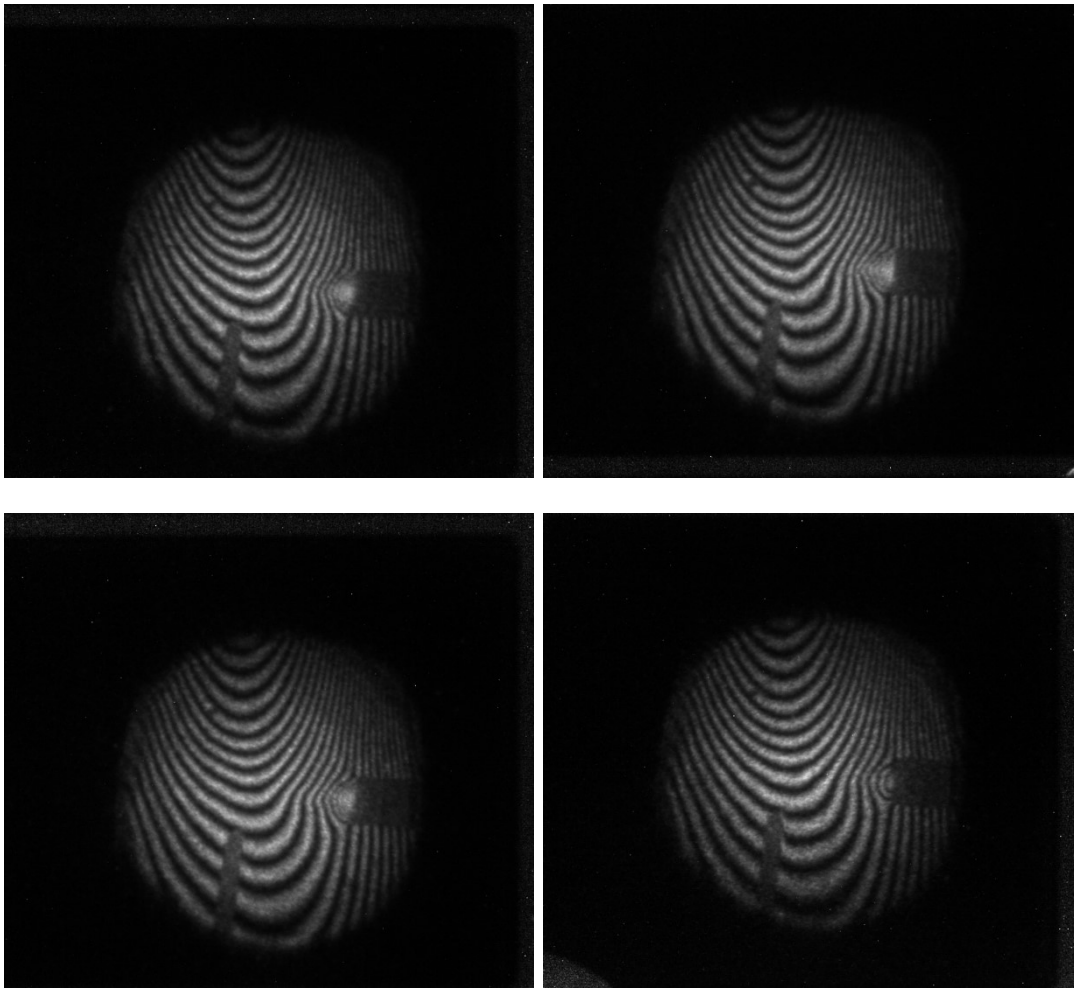

References

G.1: F.F. Chen, Introduction to plasma physics and controlled fusion, volume 1: plasma physics, Springer, 2006

1.1: B.V. Weber et al, Ultra-high electron beam power and energy densities using a plasma-filled rod-pinch diode, Physics of Plasmas, 11, 2916, 2004

1.2 Private conversation with M Sinclair of AWE, 2017

1.3: G. Bekefi and A.H. Barrett, Electromagnetic vibrations, waves and radiation, MIT Press, 1977

1.4: T.J.M. Boyd and J.J. Sanderson, The physics of plasmas, Cambridge University Press, 2005

1.5 M. Alonso and E.J. Finn, Physics, Addison Wesley, 1996

1.6: J. A. Gaunt, Continuous Absorption, Philosophical Transactions of the Royal Society of London, 1930

1.7: Private conversation with A Jones of AWE, 2014

1.8: F.L. Cochran and J. Davis, Evolution of an X-pinch plasma, Physics of Fluids B, 2, 1238, 1990

1.9: C. Ekdahl, Modern electron accelerators for radiography, 28th IEEE International Conference on Plasma Science and 13th IEEE International Pulsed Power Conference, 17-22 June 2001

1.10: N.J. Carron, An introduction to the passage of energetic particles through matter, Taylor and Francis, 2007

1.11: R. J. Adler, Pulsed Power Formulary 3rd Ed., North Star Power Engineering, 2001

1.12: C. Leroy, P.-G. Rancoita, Principles of radiation interaction in matter and detection, 2nd Ed, World Scientific, 2009

1.13: W.H. Wells, Production of high energy particles, Journal of Applied Physics 9, 677, 1938

1.14: G.A. Mesyats, Pulsed Power, Kluwer Academic / Plenum Publishers, New York, 2005

1.15: H. Bluhm, Pulsed power systems, Springer, Berlin, 2006

1.16: I. D. Smith, Induction voltage adders and the induction accelerator family, Phys. Rev. Special Topics – Accelerators and Beams, Vol 7, 064801, 2004

1.17: R. D. Mcbride *et. al.*, A Primer on Pulsed Power and Linear Transformer Drivers for High Energy Density Physics Applications, IEEE Transactions on Plasma Science, 46, 11, 2018

1.18: P.N. Martin, J.R. Threadgold, S. Vickers, Critical current operation of the self-magnetic pinch radiographic diode, IEEE Transactions on Plasma Science, 41, 9, 2013

1.19: G. Cooperstein *et al.*, Theoretical modelling and experimental characterization of a rod-pinch diode, Physics of Plasmas, 8, 4618, 2001

1.20: C. D. Child, Discharge from hot CaO, Phys. Rev. (Series I) 32, 492, May 1911

1.21: B. Cassany and P. Grua, Analysis of the operating regimes of microsecond conduction time POS, Journal of Applied Physics 78 (1), July 1995

1.22: Weber et al, Plasma Opening Switch conduction scaling, Physics of Plasmas, 2, 10, Oct 1995

1.23: A. Fruchtman, K. Gomberoff, Magnetic field penetration due to the hall field in (almost) collisionless plasmas, Physics of fluids B, 5 2371, 1993

1.24: R.D. Hazeltine and F.L. Waelbroeck, The framework of plasma physics, Westfield, 2004

1.25: K. Gomberoff and A. Fruchtman, Fast magnetic field penetration into a cylindrical plasma of nonuniform density, Physics of Fluids B, 5, 2841, 1991

1.26: J. P. Chittenden, S. V. Lebedev, C. A. Jennings, S. N. Bland, and A. Ciardi, X-ray generation mechanisms in three-dimensional simulations of wire array z-pinches, Plasma Physics and Controlled Fusion 46 (12B), B457, 2004.

1.27: A. Ciardi *et. al.*, The evolution of magnetic tower jets in the laboratory, Physics of Plasmas 14(5), 056501, 2007.

2.1: J.R. Goyer, D. Kortbawi, F.K. Childers and P.S. Sincerny, Low jitter operation of a plasma opening switch, Journal of Applied Physics 74(6), Sept 1993

2.2: L. Montgomery Smith, D.R. Keefer and N.W. Wright, Novel designs for the DECADE coaxial plasma gun, Transactions on Plasma Science, 30, 5, Oct 2002

2.3: https://www.pasternack.com/semirigid-0.250-rg401-50-ohm-coax-cable-copper-rg401-u-p.aspx (accessed Sept 2015)

2.4: Private communication with B Weber of NRL, 2014

2.5: B. Cassany, P. Grua, Analysis of the operating regimes of microsecond conduction time POS, Journal of Applied Physics, 78 (1), July 1995

2.6: C.W. Mendel Jr., D.M. Zagar, G.S. Mills, S. Humphries Jr. and S.A. Goldstein, Carbon Plasma Gun, Review Scientific Instruments, 51 (12), Dec 1980

2.7: https://www2.l3t.com/ati/pdfs/Tg-75.pdf (modern equivalent, accessed Dec 2019)

2.8: https://en.wikipedia.org/wiki/Thyratron (accessed Dec 2019)

2.9: George Swadling, PhD thesis: *An experimental investigation of the azimuthal structures formed during the ablation phase of wire array z-pinches*, Imperial College, 2011

2.10: B. Dromey, S. Kar, M. Zepf and P. Foster, The plasma mirror – A subsecond optical switch for ultrahigh power lasers, Review of Scientific Instruments, 75, 3 March 2004

2.11: G.S. Sarkisov, I.L. Beigman, V.P. Shevelko and K.W. Struve, Interferometric measurements of dynamic polarizabilities for metal atoms using electrically exploding wires in vacuum, Physics Review A, 73, 042501 (2006)

2.12: E Hecht, Optics, fourth edition, Addison Wesley, 2002

2.13: I.H. Mitchell *et. al.*, A high impedance mega-ampere generator for fiber z-pinch experiments, Review of Scientific Instruments, 67, 4, April 1996

2.14: http://www.invisiblevision.com/products/ultra-high-speed-framing (accessed Dec 2019)

2.15: G.S. Settles, Schlieren and shadowgraph techniques, Springer, 2001

2.16: I.H. Hutchinson, Principles of plasma diagnostics, 2nd Ed., Cambridge, 2002

2.17: D.H. Dolan and S.C. Jones, THRIVE: a data reduction program for three-phase PDV/PDI and VISAR measurements, Sandia National Laboratories, 2008, DOI:10.2172/942210

2.18: J. Macdonald, S.N. Bland and J. Threadgold, A fibre based triature interferometer for measuring rapidly evolving, ablatively driven plasma densities, Review of Scientific Instruments 86, 083506, 2015

2.19: R. Priest, Analysis of fiber interferometer utilizing 3 × 3 fiber coupler, IEEE Transactions on Microwave Theory and Techniques, 30 (10), 1589, 1982

2.20: G. Point *et al.*, Two-color interferometer for the study of laser filamentation triggered electric discharges in air, Review of Scientific Instruments, 85, 2014

2.21: B.V. Weber, S.F. Fulghum, A high-sensitivity two-color interferometer for pulsed power plasmas, Review of Scientific Instruments, 68, 2, Feb 1997

2.22: M. Alonso and E.J. Finn, Physics, Addison Wesley, 1996

2.23: R. Sangines de Castro, H. Sobral, C. Sanchez-Ake and M. Villagrain-Muniz, Two-color interferometry and fast photography measurements of dual-pulsed laser ablation on graphite targets, Physics Letters A, 357, 2006

2.24: S.M. McMurry, Quantum mechanics, Addison-Wesley, 1996

2.25: J. Stark, Observation of the separation of spectral lines by an electric field, Nature, 2301, 92, December 1913

2.26: P. Zeeman, The effect of magnetisation on the nature of light emitted by a substance, Nature, 1424, 55, February 1897

2.27: J.D. Hare, PhD Thesis: *High energy density magnetic reconnection experiments in colliding carbon plasma flows*, Imperial College London, 2017

2.28: http://www.andor.com/scientific-software/solis-software (accessed Aug 2019)

2.29: A Colaïtis, MSc Report: *Thomson Scattering diagnostics for Z-pinches in MAGPIE*, Imperial College, September 2010

2.30: D.H. Froula, S.H. Glenzer, N.C. Luhmann, Jr., J. Sheffield, Plasma scattering of electromagnetic radiation, 2nd Ed., Academic Press, 2011

2.31: Private communications with J.D. Hare, Imperial College London, 2018

2.32: Electron density fluctuations in a plasma, E.E. Salpeter, Physics Review, 120, 5, 1960

2.33: Suttle L.G. *et al.*, Ion heating and magnetic flux pile-up in a magnetic reconnection experiment with super-Alfvénic plasma inflows, Physics of Plasmas, 25, 042108, 2018

3.1: L. Montgomery Smith, D.R. Keefer and N.W. Wright, Novel designs for the DECADE coaxial plasma gun, Transactions on Plasma Science, 30, 5, Oct 2002

3.2: https://www.prism-cs.com/software/prismspect/overview.html (accessed Aug 2019)

3.3: C.W. Mendel Jr., D.M. Zagar, G.S. Mills, S. Humphries Jr. and S.A. Goldstein, Carbon plasma gun, Review Scientific Instruments, 51 (12), Dec 1980

3.4: B. Cassany and P. Grua, Analysis of the operating regimes of microsecond conduction time POS, Journal of Applied Physics 78 (1), July 1995

3.5: R.D. Hazeltine and F.L. Waelbroeck, The framework of plasma physics, Westfield, 2004

3.6: J. Macdonald, S. N. Bland, and J. Threadgold, A fibre based triature interferometer for measuring rapidly evolving, ablatively driven plasma densities, Review of Scientific Instruments, 86, 083506 2015

3.7: B.V. Weber, S.F. Fulghum, A high-sensitivity two-color interferometer for pulsed power plasmas, Review of Scientific Instruments, 68, 2, Feb 1997

3.8: Extracted from "Two-colour interferometry and Thomson scattering measurements of a plasma gun", Hare, J; et al.© IOP Publishing, Reproduced with permission. All rights reserved.

3.9: G. Point *et al.*, Two-color interferometer for the study of laser filamentation triggered electric discharges in air, Review of Scientific Instruments, 85, 2014

3.10: R. Sangines de Castro, H. Sobral, C. Sanchez-Ake and M. Villagrain-Muniz, Two-color interferometry and fast photography measurements of dual-pulsed laser ablation on graphite targets, Physics Letters A, 357 (2006) 351-354

3.11: https://www.nist.gov/pml/atomic-spectra-database (accessed Dec 2019)

3.12: F.F. Chen, Introduction to plasma physics and controlled fusion, volume 1: plasma physics, Springer, 2006

3.13: Private communications with J.D. Hare, Imperial College London, 2018

3.14: D.H. Froula, S.H. Glenzer, N.C. Luhmann, Jr., J. Sheffield, Plasma scattering of electromagnetic radiation, 2nd Ed., Academic Press, 2011

3.15: A. Savitzky and M. Golay, Smoothing and differentiation of data by simplified least squares procedures, Analytical Chemistry, 36, 8, July 1964

4.1: B.V. Weber *et al.*, Ultra-high electron beam power and energy densities using a plasma-filled rod-pinch diode, Physics of Plasmas, 11, 2916, 2004

4.2: R.D. Hazeltine and F.L. Waelbroeck, The framework of plasma physics, Westfield, 2004

4.3: T.J.M. Boyd and J.J. Sanderson, The physics of plasmas, Cambridge University Press, 2005

4.4: B. Cassany and P. Grua, Analysis of the operating regimes of microsecond conduction time POS, Journal of Applied Physics 78 (1), July 1995

4.5: F.F. Chen, Introduction to plasma physics and controlled fusion, volume 1: plasma physics, Springer, 2006

4.6: R. Rhodes and D. Keefer, Numerical simulation of cableguns using MACH2, Transactions on Plasma Science, 31, 2, 2003

4.7: J. P. Chittenden, S. V. Lebedev, C. A. Jennings, S. N. Bland, and A. Ciardi, X-ray generation mechanisms in three-dimensional simulations of wire array z-pinches, Plasma Physics and Controlled Fusion 46 (12B), B457, 2004

4.8: A. Ciardi *et al.*, The evolution of magnetic tower jets in the laboratory, Physics of Plasmas 14 (5), 056501, 2007

4.9: Paraview, https://www.paraview.org (accessed August 2019)

4.10: Origin 2017, https://www.originlab.com (accessed August 2019)

5.1: B.V. Weber *et al.*, Ultra-high electron beam power and energy densities using a plasma-filled rod-pinch diode, Physics of Plasmas, 11, 2916, 2004

5.2: S.V. Loginov, Plasma dynamics in microsecond megaampere plasma opening switches, Physics of Plasmas, 18, 102104, 2011

5.3: B. Cassany and P. Grua, Analysis of the operating regimes of microsecond conduction time POS, Journal of Applied Physics 78 (1), July 1995

5.4: Weber *et al.*, Plasma Opening Switch conduction scaling, Physics of Plasmas, 2, 10, Oct 1995

5.5: A. Fruchtman, Penetration and expulsion of magnetic fields in plasmas due to the hall field, Physics of Fluids B, 1908, 1991

5.6: K. Gomberoff and A. Fruchtman, Fast magnetic field penetration into a cylindrical plasma of nonuniform density, Physics of Fluids B, 5, 2841, 1991

6.1: B. Cassany and P. Grua, Analysis of the operating regimes of microsecond conduction time POS, Journal of Applied Physics 78 (1), July 1995

6.2: K. Gomberoff and A. Fruchtman, Fast magnetic field penetration into a cylindrical plasma of nonuniform density, Physics of Fluids B, 5, 2841, 1991